THE PENNSYLVANIA STATE UNIVERSITY
SCHREYER HONORS COLLEGE

DEPARTMENT OF ENGINEERING SCIENCE AND MECHANICS

DEVELOPMENT OF EBPVD MAGNESIUM ANODE MATERIAL FOR USE IN A 'GREEN' BATTERY

ROBERT GRESH
Spring 2012

A thesis
submitted in partial fulfillment
of the requirements
for a baccalaureate degree
in Engineering Science
with honors in Engineering Science

Reviewed and approved* by the following:

Mark Horn
Professor of Engineering Science and Mechanics
Thesis Co-Adviser

Barbara Shaw
Professor of Engineering Science and Mechanics
Honors Adviser
Thesis Co-Adviser

Judith A. Todd
P. B. Breneman Department Head Chair
Professor of Engineering Science and Mechanics

* Signatures are on file in the Schreyer Honors College.

ABSTRACT

The development of a “green” battery with a magnesium anode and polymer cathode could help to meet current energy needs while decreasing the negative environmental impact that is caused by disposable batteries. There are many advantages to developing magnesium for use as an anode material. Magnesium is a fairly inexpensive and environmentally friendly material when compared to competing anode materials such as aluminum, zinc and lithium. The specific compositions of magnesium alloys can be varied and the structure of magnesium films can be controlled through the method of Electron Beam Physical Vapor Deposition (EBPVD). This thesis discusses the electrochemical and structural characteristics of MgAlZn alloy thin films deposited via EBPVD.

Magnesium alloy thin films targeted to have 6% Al and 1% Zn were deposited with varying thicknesses of 3.01 µm, 5.89 µm, 7.17 µm and 7.79 µm were analyzed and compared. Scanning electron microscopy was used to image the surface and cross-sectional views of the films. The SEM analysis provided a measurement of thickness from the cross-sectional view. SEM analysis on the surface of each film indicated that thicker films have a more defined surface structure and, therefore, more surface area. AZ61 thin films were tested using polarization resistance and electrochemical impedance spectroscopy in order to evaluate their electrochemical characteristics. The corrosion rates determined by these tests were compared and it was found that corrosion rate increases as a function of film thickness, which is likely caused by the increase in surface area. ICP analysis showed that the thin films contained very little Al and Zn in their compositions.

Further investigation is required to confirm the conclusions of this thesis. Advanced imaging methods such as FESEM and XRD can be used to gain more information on the surface structure of the

films. Several methods of fabricating thin films can be used to increase percentage of Al and Zn in the composition of the films.

Table of Contents

List of Figures

List of Tables

Acknowledgements

Advisors: Dr. Barbara Shaw, Dr. Mark Horn, Dr. Elizabeth Sikora

Undergraduate and Graduate Students: Dan Cook, Anna Hartsock, Hitesh Basantani, Beth Bimber, Rob Vadella, Tony Naccerelli, Derek Wolfe, Nick Chu

Introduction:

Problem Statement

The development of a "green" battery with a magnesium anode and polymer cathode could help to meet current energy needs while decreasing the negative environmental impact that is caused by standard batteries. This battery can be considered "green" because the materials used in the battery are environmentally friendly and biodegradable.

Design Needs

There are many advantages to developing magnesium for use as an anode material. Magnesium is a fairly inexpensive and environmentally friendly material and when compared to competing anode materials such as aluminum, zinc and lithium, has the highest galvanic potential. The specific compositions of magnesium alloys can be varied and the structure of magnesium films can be controlled through the method of Physical Vapor Deposition (PVD). Using PVD, the structure of Mg alloy films can be altered by varying the deposition rate, distance, temperature, or by the motion of the substrate. By using PVD, magnesium can be alloyed with elements that are either not soluble or have only limited solubility in magnesium [1, 2]. Furthermore, magnesium alloys that were created by PVD display different corrosion properties than cast magnesium alloys [3], which is important for battery applications because corrosion properties are closely related to the power output and life of a battery. PVD provides many design opportunities in the development of a magnesium anode for a battery.

After films are created they need to be tested for electrochemical properties to determine whether or not they could be useful as a battery anode. The properties of interest include energy density, galvanic corrosion properties, open circuit potential, and discharge characteristics. These properties were tested with various electrochemical experiments. The structure of the film is also of interest and this property can be determined by using X-ray diffraction and scanning electron microscopy (SEM). Once these characteristics are determined and analyzed, new thin-films can be designed and produced and the testing process repeated, until an effective anode is developed.

Objective

This thesis is primarily concerned with the PVD processes that were used to create candidate magnesium alloys for use in the design of "green" or environmentally friendly batteries. Several thin films were made by EBPVD from AZ61 bulk material. This is a commercially available magnesium alloy designed to have improved corrosion resistance over pure magnesium and targeted to have 6% aluminum and 1% Zn. The thin films made from the AZ61 alloy were deposited at different deposition rates and to different thicknesses and then characterized using electrochemical tests, profilometry, SEM, and ion coupled plasma spectroscopy. The specific goal of this research was to better understand how deposition thickness influences the electrochemical properties of the thin film alloys so that a better battery material can be developed.

Literature Review:

Electron Beam Physical Vapor Deposition

Coatings are used in a wide variety of engineering applications today. Thermal barrier coatings protect jet engines from large changes in temperature. Corrosion coatings help to prevent structural materials from degrading. Coatings can be used to alter optical, electrical, adhesive, and magnetic properties of a surface. One important type of coating is thin films. Thin films are created through various deposition techniques and are an important part of semiconductors and other small electronic devices. One common technique for thin film deposition is Electron Beam Physical Vapor Deposition (EBPVD).

Electron Beam Physical Vapor Deposition is a deposition process in which a source material is evaporated by an electron beam under high vacuum in order to deposit a thin film on a substrate. EBPVD occurs at high vacuum so that a solid source can evaporate. The source material is evaporated using an electron beam to rapidly heat the material into its vapor phase. After the material is turned into vapor, it is deposited onto a substrate and a solid thin film is formed. The parameters of EBPVD can be closely controlled in order to design useful thin films [4]. A typical setup of the components of an EBPVD system is shown in Figure 1.

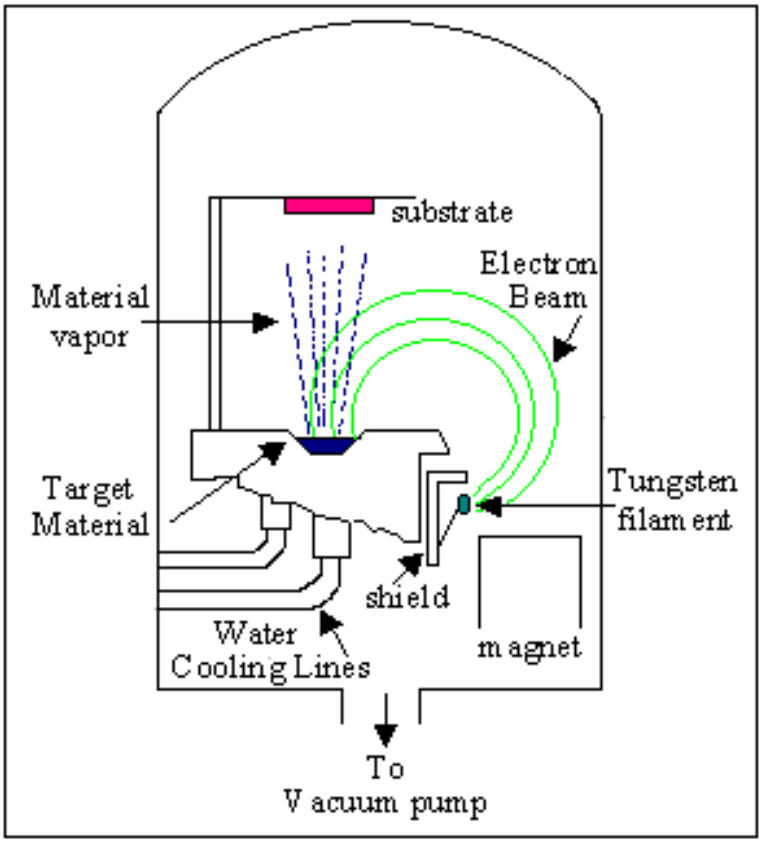

Figure 1. High vacuum chamber with labeled important EBPVD components [5]

Deposition Conditions

The conditions at which the Electron Beam Physical Vapor Deposition process occurs has a significant effect on the resulting thin film. In order for the source material to evaporate, the deposition chamber must be at high vacuum. High vacuum refers to a pressure of less than 1×10−3 Torr, which is significantly lower than standard atmospheric pressure (760 Torr) [4]. The temperature is not as crucial as the pressure and can be varied to change the properties of the resulting thin film. The motion and distance of the substrate from the electron beam can also be manipulated to change the uniformity of the film and its microstructure.

Electron Beam Evaporation

An electron beam is used to provide the energy that vaporizes the source material. An electron beam is produced using an electron gun like the one shown in Figure 2. The electron gun requires a high voltage source of 10kV and a large current in order to form an electron beam. Electromagnets can be used to direct the beam across the surface of the source material in order to provide uniform evaporation. When the electron beam hits the surface of the source material, the kinetic energy of the electrons is converted into thermal energy and the temperature of the source material rises quickly. As the temperature of the source material rises, the material transforms rapidly from a solid to a vapor because of the low pressure (high vacuum) within the chamber.

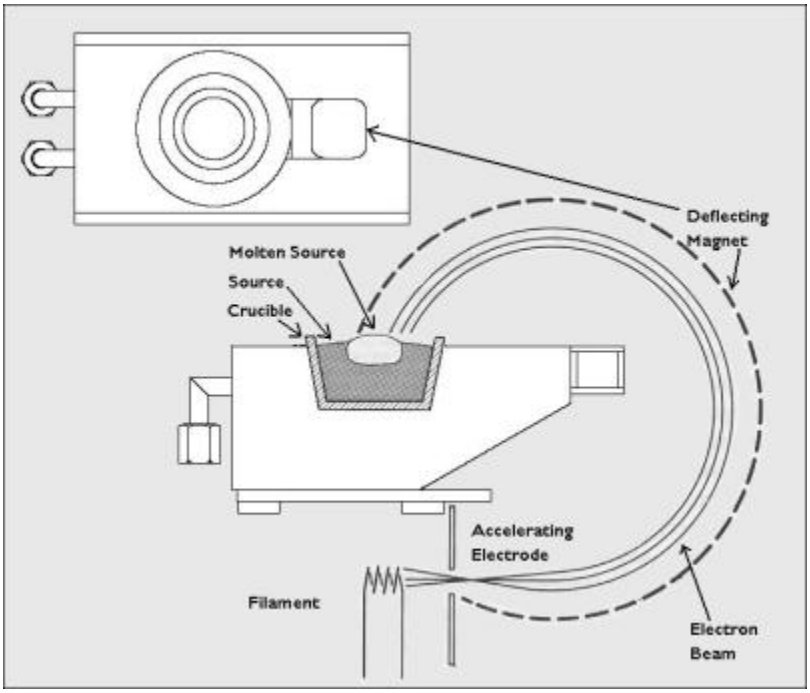

Figure 2. Electron Gun and Magnetic Beam former [6]

There are three different forms of evaporation that can occur, each resulting in a different material at deposition [7], these are:

- *Direct Evaporation*: the source material evaporates directly into its vapor phase and is deposited with the same chemical composition of the source material.
- *Reactive Evaporation:* occurs when evaporation occurs in the presence of a gas that reacts with the source material to form a material of a new composition. For example, a pure Titanium ingot could be evaporated in the presence of oxygen gas to form TiO_2, which would then be deposited onto the substrate.
- *Co-evaporation*: occurs when multiple source materials are evaporated and deposited on the substrate simultaneously, the resulting film composition will be determined by the deposition rates of each materials and how the different materials interact.

After the source material is evaporated it moves through the chamber, because the vapor is seeking an equilibrium pressure. As the vapor moves throughout the chamber, everything within line of sight of the source material will be coated via deposition. A thin film is formed as the vapor deposits on the surface of the substrate. The properties of the film can be varied by varying the substrate temperature, the distance of the substrate from the source, the motion of the substrate, and how the substrate material interacts with the vapor of the source material [4]. Substrates are often single crystal silicon wafers that are kept as clean as possible in order to minimize defects in the thin film. Substrates are often rotated so that the film deposits uniformly across the surface of the substrate.

Advantages of Electron Beam Physical Vapor Deposition

There are many advantages to using Electron Beam Physical Vapor Deposition over other deposition methods. Many characteristics of the thin film being produced can be altered by changing the parameters of the deposition such as the substrate temperature, deposition rate and motion of the substrate. As a result, EBPVD is useful in research because thin films with slightly differing properties can be produced and tested until a desirable film is developed. Higher deposition rates can be achieved with EBPVD than with other physical vapor deposition techniques, such as cathodic arc deposition, evaporative deposition, pulsed laser deposition and sputter deposition. Many other deposition techniques require high temperatures, but EBPVD allows evaporation and deposition to occur at low temperatures and the temperature can also be varied to change properties [8].

Disadvantages of Electron Beam Physical Vapor Deposition

The main disadvantage of EBPVD is the high cost to set up and maintain the equipment required to perform the process. The vacuum chamber, pumping system, electron guns, high voltage systems, and electromagnets require uncommon and expensive pieces of equipment that need to be carefully maintained and calibrated[7]. The EBPVD process is more complex than other deposition process and each parameter must be carefully considered, which can make it difficult to produce multiple films with consistent properties. Many other deposition processes are much simpler and/or more uniform and reproducible films can be made easily, however each deposition technique has drawbacks and advantages.

Electron Beam Physical Vapor Deposition in Research

Electron Beam Physical Vapor Deposition is an important process in the fabrication of modern devices. Through the use of Physical Vapor Deposition a variety of specialized thin films can be created with very specific properties and functions, such as metastable metal alloys. Through the precise control of deposition parameters many properties of the thin film can be controlled, which makes EBPVD a desirable deposition method for research. EBPVD can also have a higher deposition rate than other deposition techniques and this makes it useful in the manufacturing of thin films that are several micrometers thick. The versatility of the EBPVD process is one of its primary strengths, making it a powerful and practical tool for research.

Magnesium and Magnesium Alloys

Magnesium is a very unique and useful engineering material. Magnesium is an alkaline metal and has desirable properties as a structural material because of its combination of light weight and relatively high strength. In addition, magnesium is the 8th most common element on earth making it a relatively inexpensive metal [9]. Despite these desirable qualities, magnesium is not commonly used as a structural material because it is highly susceptible to corrosion. As a result, magnesium is primarily used as an alloying component to create strong, lightweight aluminum alloys [10]. Magnesium is both environmentally friendly and biologically compatible when compared to other metals. In fact, magnesium is essential for many functions in the human body and the average adult should consume 300-400 mg of magnesium each day [11]. Because magnesium is so compatible with the human body, it is currently being tested and used in various bioengineering applications. One of the primary uses for magnesium in the body is as a material for structural implants, because its strength and density is very close to that of human bone [12].

As seen in Table 1, magnesium is the most electrochemically active of all engineering metals and, as a result, it is highly susceptible to galvanic corrosion. In fact, it acts as an anode when placed in a galvanic couple with other metals. This makes magnesium useful as an anode in a galvanic battery. By alloying magnesium with other metals such as aluminum, zinc, titanium, and yttrium the galvanic corrosion rate of the magnesium can be altered [1]. One useful tool for alloying magnesium is the physical vapor deposition process that was mentioned earlier in this review. PVD allows alloys to be produced that are not possible with other methods, because PVD does not require the alloying elements to be soluble with one another. With the use of PVD, magnesium alloys can be produced with desirable corrosion properties for battery applications. Vapor deposited magnesium alloys are often significantly more corrosion resistant than cast magnesium alloys [3].

Table 1. Comparison of Ecorr values of several engineering metals in water solution at 5% NaCl [13]

Metal	E_{corr}, V_{SCE}
Mg	-1.65
Zn	-1.02
Al-7075	-0.88
Al-1xxx	-0.73
Fe	-0.50
Cu	-0.12
Ni	+0.01

Magnesium-Carbon Battery

The battery industry is a relatively young and thriving one. Batteries are used in a wide variety of applications from small wristwatch batteries to much larger car batteries. More electronic devices that require batteries are produced each year and the demand continues to grow along with the popularity of portable electronic devices such as laptops and cell phones. A battery is an electrochemical cell that converts chemical energy into electricity. Primary and Secondary batteries are the two major types of batteries. Primary batteries, or disposable batteries, are designed not to be rechargeable, whereas Secondary batteries, or rechargeable batteries, are designed to be recharged and reused. This research is focused on a primary, wet-cell, reserve battery. A wet-cell battery (basic setup shown in Figure 3) is one that uses a liquid electrolyte and a reserve battery can be stored for a long time before becoming active. In the magnesium-carbon battery, seawater is the liquid electrolyte and it is a reserve battery because it can be stored dry and the electrolyte can be added to activate the cell when it is ready to be used.

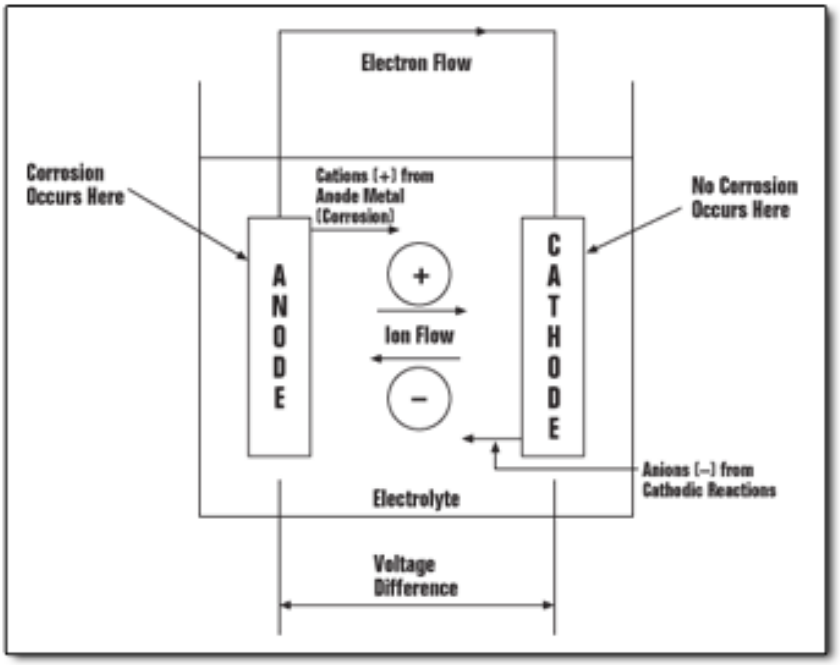

Figure 3. Diagram of a basic electrochemical wet cell. [14]

Primary batteries often consist of an anode and cathode (usually metals) that are placed in an electrolyte to form a galvanic couple. Some of the most common primary batteries are made up of a zinc anode and a carbon or manganese cathode. According to a review carried out by the Materials Systems Lab at the Massachusetts Institute of Technology in 2010, “Approximately 80% of portable batteries manufactured in the US are so-called alkaline dry cells with a global annual production exceeding 10 billion units. Today, the majority of these batteries go to landfills at end-of-life”[15]. Because so many

batteries end up in landfills, there is a large interest in decreasing the environmental impact of the battery industry through use of more environmentally friendly materials and processes.

Figure 4 shows the discharge of a magnesium- PEDOT battery and shows that the battery can perform at a voltage of just under 1.5 volts for several days. Figure 5 shows that magnesium operates at a potential of around 1.5 volts in $MgCl_2$ solutions. This data demonstrates that a magnesium- PEDOT battery can operate at a potential of around 1.5V, which is the same voltage as current alkaline batteries, such as the AA battery. Therefore, there is a strong interest in developing magnesium-PEDOT batteries as an environmentally friendly alternative to these common batteries.

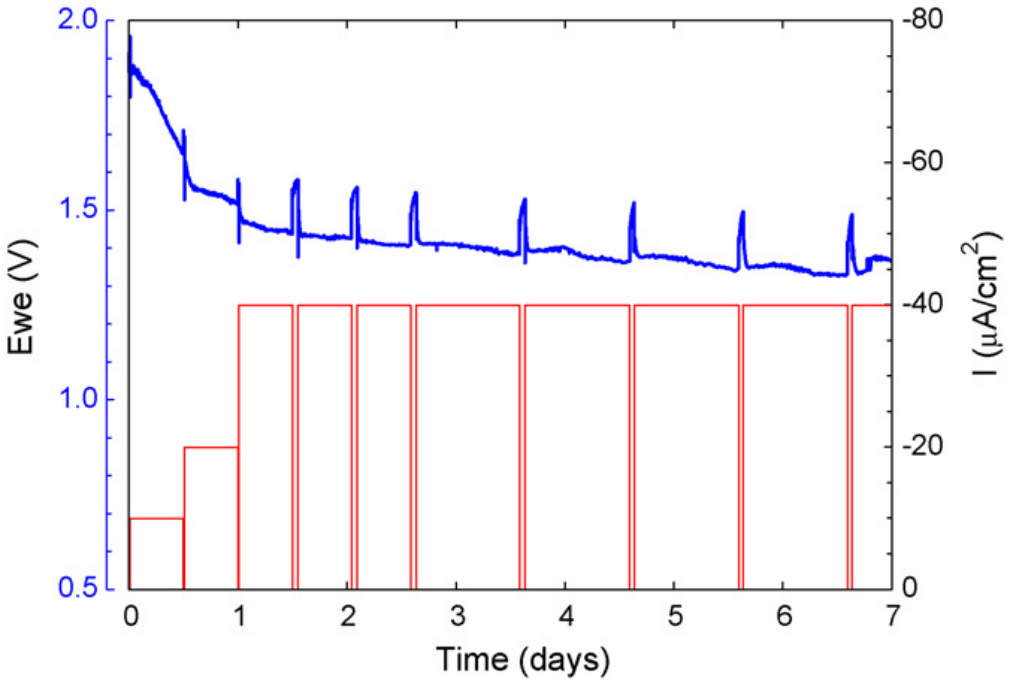

Figure 4. “Typical discharge curves for the Mg/MgCl2/PEDOT/O2 cell. The discharge current (thin line) was initially stepped up to 40_A/cm2 in three steps as shown, and then held for more than a week at this level. Discharging was interrupted daily in order to perform EIS measurements.” Graph from reference 16.

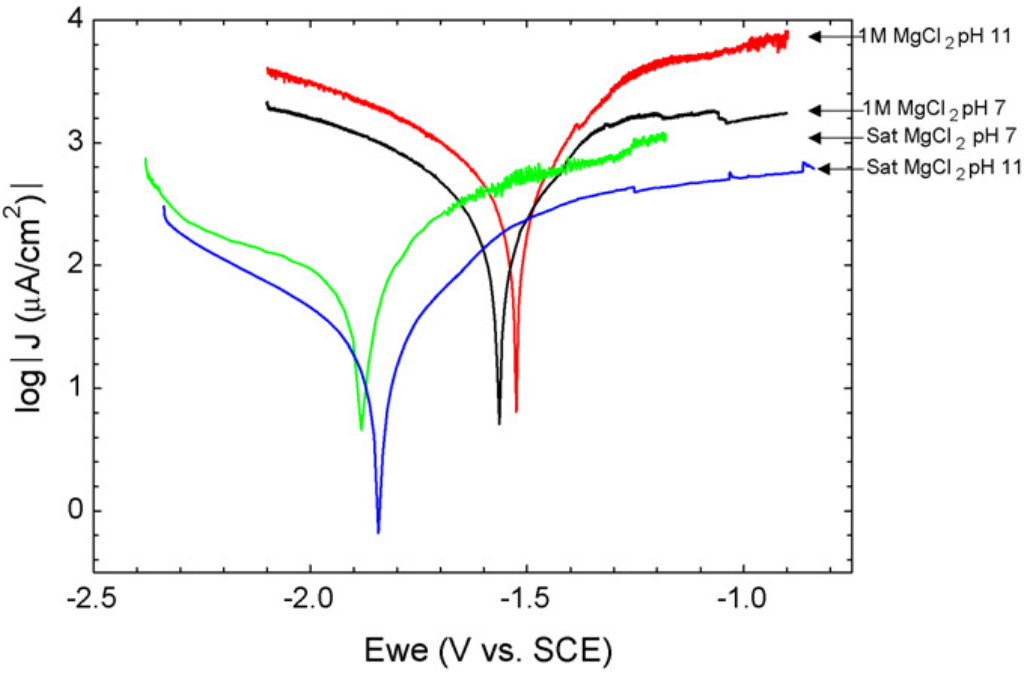

Figure 5. Polarization curves of magnesium in aqueous solutions various $MgCl_2$ concentrations. Graph from reference 16.

Experimental

Electron Beam Physical Vapor Deposition

For this research, EBPVD was used to fabricate magnesium alloy thin-films for use as an anode for a primary reserve battery. The EBPVD system was designed at Penn State and features two Telemark electron guns that operate at 10kV, quartz crystal microbalances to measure deposition rate, and a high vacuum that can pump to a pressure of under 3.6E-6 Torr. The system also contains a programmable motor system to rotate the substrate. The system is made up of the following key components.

Source Material and Substrate

The source material (Figure 6) is deposited onto an oxidized single crystal silicon wafer (Figure 7 and Figure 8). These wafers make for a clean, uniform and inert surface. These wafers are an important part of the deposition process because in order for a film to grow properly it is important that the substrate surface does not contain defects and that the substrate material does not react with the film. The substrate is attached to a motor system within the chamber that spins the substrate during deposition, helping to create a more uniform film. After deposition, the coated wafer is cleaved into smaller pieces so that various tests could be performed on the same thin film sample.

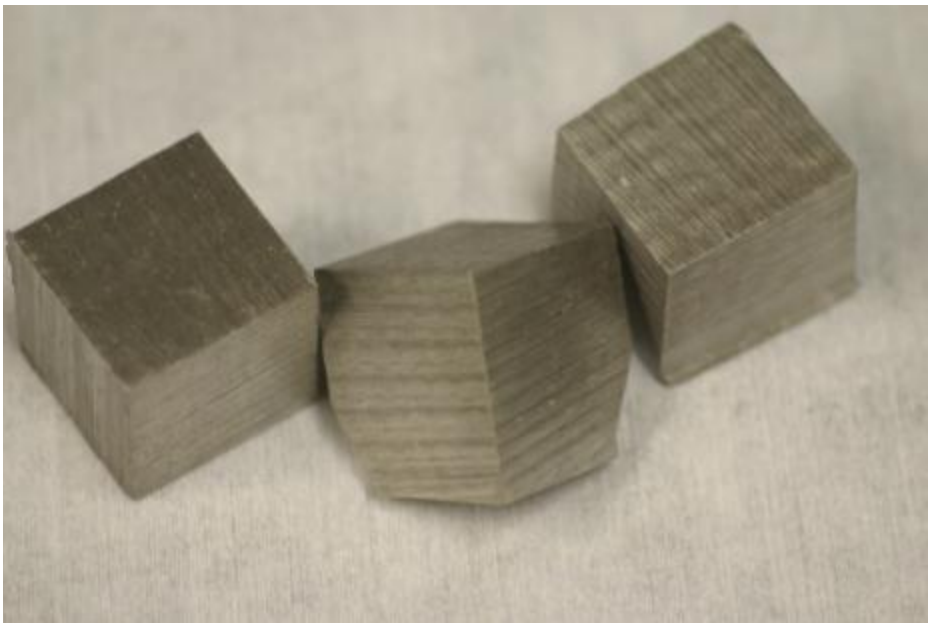

Figure 6. Pure magnesium source material for deposition, similar blocks of AZ61 were used as source material for the thin film alloys made in this research.

Figure 7. Oxidized silicon wafer to be used as substrate. A small piece of glass is taped on the polished surface with Kapton tape to mask the surface for profilometry measurements.

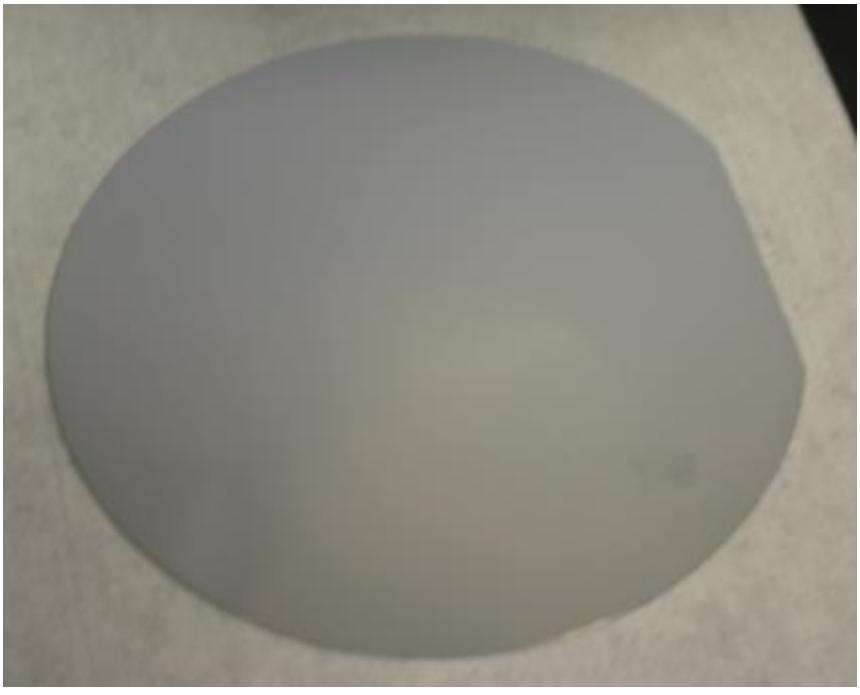

Figure 8. Silicon wafer with a thin film deposited from AZ61 on the polished surface of the wafer.

Vacuum System

The vacuum system includes a roughing pump and a cryopump (Figure 9). The roughing pump allows the chamber to be pumped down from atmospheric pressure, which is about 760 Torr, to under 100 mTorr. Once the system has reach 100 mTorr, a valve system allows the roughing pump to be sealed off and then the system is opened up to the cryopump, which will take it down to $3x10^{-8}$ Torr, which is high vacuum and will allow the deposition process to take place. During deposition, the pressured rises to the mid 10^{-5} Torr range.

Figure 9. High vacuum system with cryopump (right), Deposition Controllers and Power Supply Controllers (Left)

High Voltage System

A high voltage system provides the power that is necessary to operate the electron beam emitters. A 10 kW high voltage power supply is connected to the electron beam emitters within the high vacuum chamber. The maximum current of this power supply is 1 Amp and the maximum voltage of the power supply is 10kV.

Electron Beam Emitters and Electromagnets

The system contains two electron beam emitters within the chamber, each with their own electromagnet that allows the beam to be directed onto the surface of the source material (material to be deposited). The electromagnets can be controlled using a device outside of the chamber in order to center the beam on the source material.

Deposition Controller

A deposition controller is used for each electron beam controls the power that is supplied to each electron beam emitter (Figure 10). By controlling and adjusting this power, the electron beam can be used to vaporize a wide range of metals and the deposition rate can be controlled to 0.1 Angstroms/sec (1 Angstrom is $1x10^{-10}$ meters). The instantaneous deposition rate is measured by quartz crystal monitors. By keeping track of the deposition rate and the time, the thickness is also estimated and films can be grown to a target thickness.

Figure 10. Telemark 880 and 860 deposition controllers that are used in the EBPVD system.

All of these components play an important role in allowing the EBPVD system to function properly and determine how the thin-film is grown.

Profilometry

After a film has been deposited on the surface of the substrate and removed from the vacuum chamber, profilometry is performed to measure the thickness of the film. The wafer is placed into a contact profilometer, which measures the thickness of the film by dragging a stylus across the surface and measuring the difference in the depth of the stylus (Figure 11). Prior to depositing on the substrate, a small piece of glass is attached with Kapton tape. After deposition, the glass piece is removed and the profilometer is able to measure the difference between the surface of the substrate and the surface of the film. This thickness measurement is necessary because the thickness of the film is never exactly what is predicted by the deposition controller.

Figure 11. Tencor P-10 Surface Profiler. This instrument was used to measure the thickness of thin films after deposition.

Inductively Coupled Plasma Atomic Emission Spectrometry

Inductively coupled plasma atomic emission spectrometry (ICP-AES) allows the concentration of an element in a sample to be determined. This technique uses inductively coupled plasma to excite atoms and ions to emit electromagnetic radiation. The wavelength of the radiation is unique for each element and the intensity of the emission can be used to determine the concentration of the element in the sample. Using this method, the concentrations of various elements in the samples can be determined. This is important because when alloying materials using vapor deposition, the resulting composition is not always what is expected.

Scanning Electron Microscope

A scanning electron microscope is used to image materials by scanning the material with a beam of electrons (Figure 12). In this project, secondary electron imaging was used to study the topography of the film surfaces. Cross-sections of the thin films that were deposited were also prepared and images of the edge of each film evaluated so that growth could be seen and the thickness of the film could be measured and cross-referenced with profilometry measurements.

Figure 12. Philips XL30 Environmental Scanning electron microscope used to image the surface of films [17]

Electrochemical Testing

Electrochemical testing was performed on the samples in order to determine their corrosion characteristics. The tests were performed on a Gamry Reference 3000 Potentiostat, which is connected to a computer that uses the Gamry Framework software to run electrochemical experiments.

Sample Preparation

Before cleaved samples of the thin film can be electrochemically tested they must be prepared in a way such that only the corrosion of the thin-film will be measured and not that of the silicon substrate. In order to create an electrical connection with the film, a wire is bonded to the sample at the surface of the thin film as shown in Figure 13. Then the sample and the exposed copper wire are coated with 5 layers of PMMA (polymethylmethacrylate) in order to protect the silver bond, copper wire, and silicon substrate, and mask them off for the so that they are not included in electrochemical measurements (Figure 13).

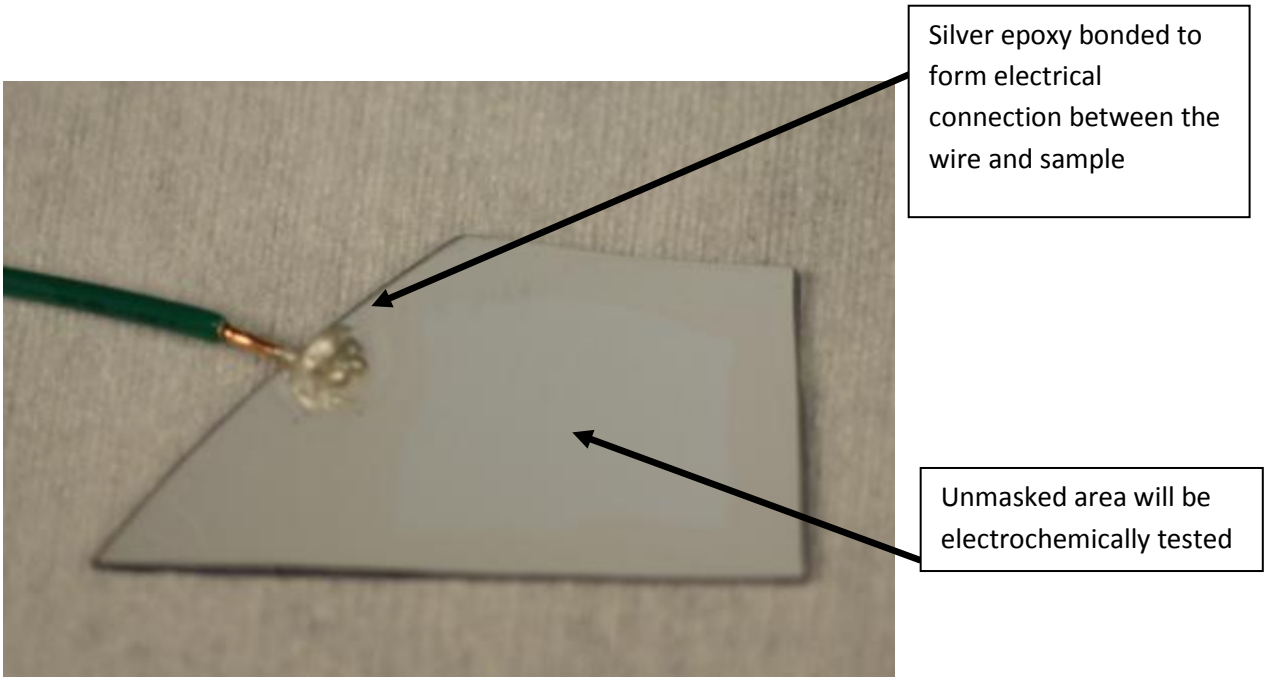

Figure 13. A cleaved wafer sample that has had a copper wire bonded to it with silver epoxy and has been maxed with 5 coats of PMMA. Note that the corrosion area is also determined by the PMMA.

Electrochemical Cell Setup

For each electrochemical experiment, an electrochemical cell was setup that used artificial seawater as an electrolyte. Three electrodes are required for the experiments, a reference electrode, counter electrode, and working electrode. A saturated calomel electrode (SCE) was used as the reference electrode. The working electrode is the thin film deposited from AZ61 and a graphite rod was used as the counter electrode. The experiments were conducted at ambient lab temperature, which is about 25°C, in the setup shown in Figure 14.

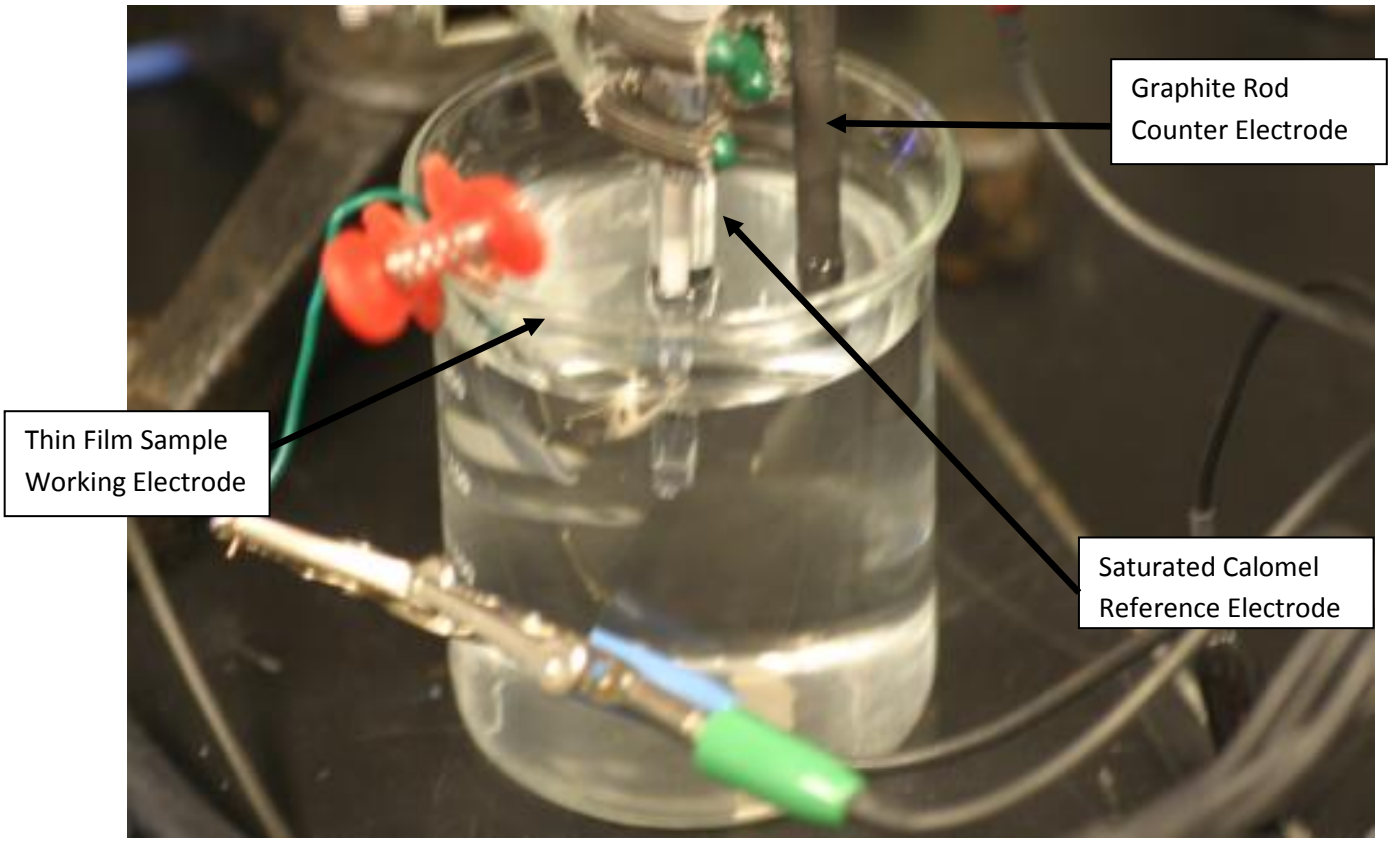

Figure 14. Electrochemical cell setup for corrosion testing. The cell uses a saturated calomel reference electrode, graphite rod counter electrode, and is filled with artificial seawater. The wafer sample acts as the working electrode during the electrochemical experiments.

Open Circuit Potential

The open circuit potential is the potential of the working electrode relative to the reference electrode when no potential or current is applied to the cell. The first experiment that is run in the sequence of corrosion experiments is a measurement of the open circuit potential. This potential value will provide a reference point for the following experiments. Open circuit potential experiments were performed for 20 minutes before and after each set of polarization resistance and EIS experiments. Figure 15 shows a graph of open circuit potential vs. time that is generated by the Gamry Echem Analyst software.

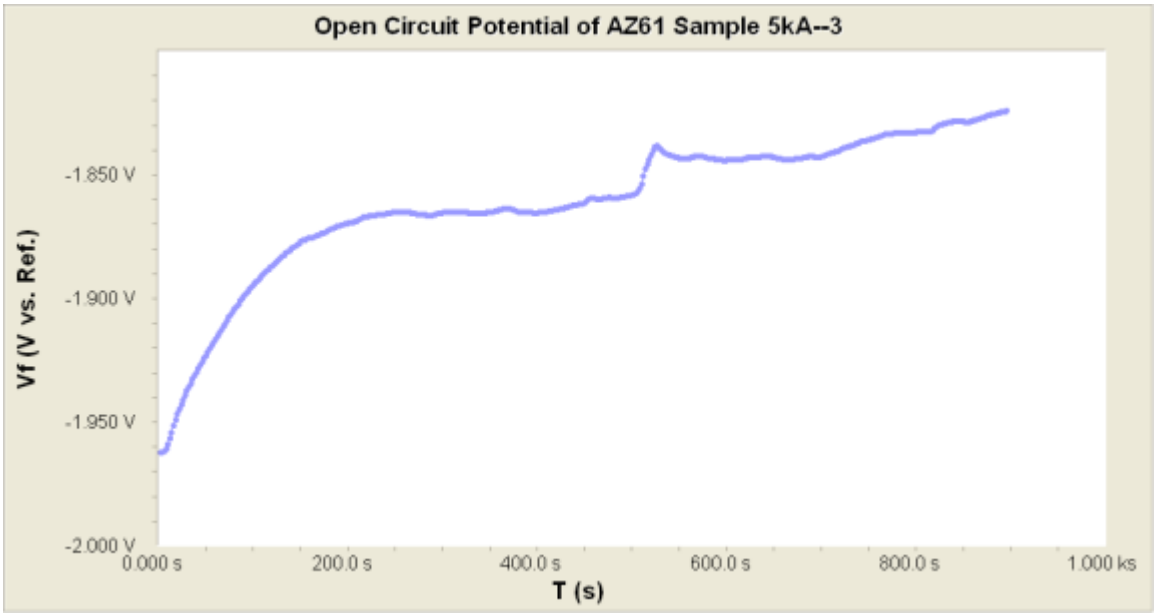

Figure 15. Open Circuit Potential vs Time plot where the reference elctrode was a saturated calomel electrode for an AZ61 alloy exposed to artificial seawater at ambient lab temperature (approximately 25°C).

Polarization Resistance

In a polarization resistance test, the voltage is varied around the open circuit potential and then a graph of potential (V vs SCE) vs current density is generated by the Gamry Echem Analyst software as shown in Figure 16. The R_p can be found from the slope of this graph and used to determine corrosion current density i_{corr} by using the Stearn Geary equation (Equation 1).

$$i_{corr} = \frac{\beta_a \beta_c}{2.3(\beta_a + \beta_c)R_p}$$

Equation 1. Calculation of corrosion current density from polarization resistance [18]

Where i_{corr} is the corrosion current density (A/cm^2), R_p is the polarization resistance (Ω*cm^2), β_a is the anodic tafel slope (V/decade) and β_c is the cathodic tafel slope (V/decade). It is common practice to estimate both tafel slope values to be 0.1 V/decade. Once the corrosion resistance is determined by plugging R_p into Equation 1, the corrosion rate can be determined using Equation 2.

$$r = \frac{K * i_{corr} * EW}{\rho}$$

Equation 2 Calculation of corrosion rate from corrosion current density [18]

In Equation 2, r is the corrosion rate in units determined by the constant, K, $i_{corr}$is the corrosion current density (μA/cm^2), EW is the equivalent weight, and ρ is the alloy density (g/cm^3). Equivalent weight and alloy density can be determined from the properties of the alloying materials and the ICP data. The corrosion current density is taken from the experimental data and the calculations of Equation 1. K is a constant that can be varied to allow the equation to output corrosion rates in different units. In this research, a K value of 0.129 was used to yield a corrosion rate in mils per year (mpy).

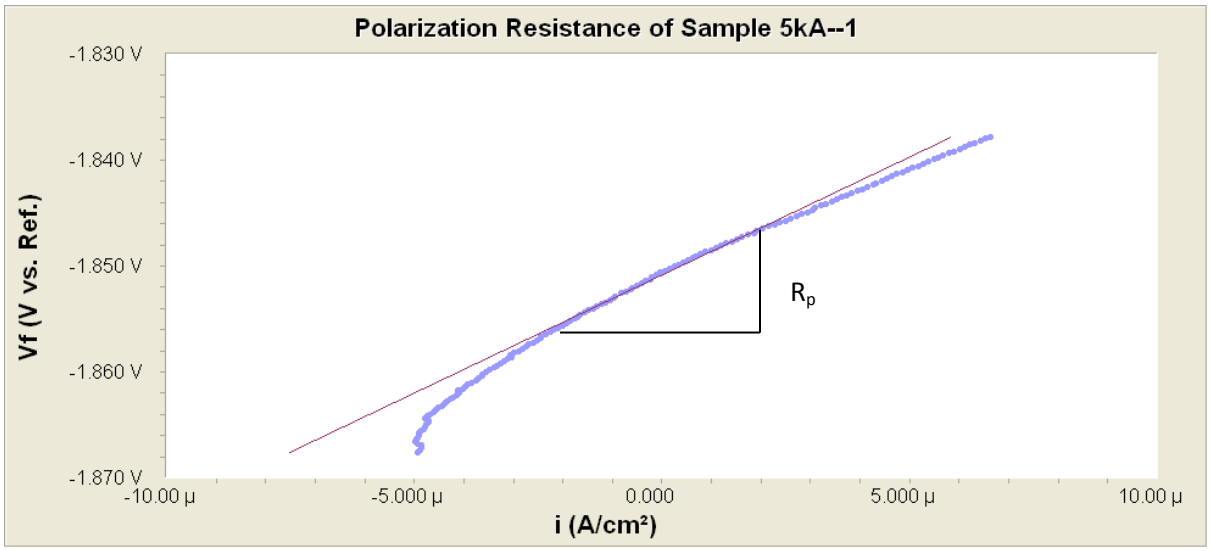

Figure 16. Potential vs Current Density used to determine R_p. The straight red line is fitted around 0 current density and the slope of this line is R_p.

From Figure 16, the slope of the red line, R_p, was measured by the Gamry software to be 2234 ohms*cm^2. This R_p value can now be plugged into the Stearn Geary Equation to find i_{corr}:

$$\frac{0.1 \times 0.1}{2.3\,(0.1 + 0.1)\,2234}$$

The calculated i_{corr} is 9.72μA. This can then be converted to a corrosion rate in mpy by using Equation 2. The equivalent weight for the AZ61 samples is 12.4 and the density is 1.76. Plugging these values into Equation 2 gives:

$$\frac{0.129 \times 9.72 \times 12.4}{1.76}$$

which yields a corrosion rate of 8.82 mpy. All of these calculations are performed by the Gamry software during polarization resistance analysis.

Electrochemical Impedance Spectroscopy

Electrochemical impedance spectroscopy (EIS) can be used to determine the corrosion rate of a metal sample in an electrolyte. During EIS a sinusoidal current is applied to the sample as a function of frequency and used to find the polarization resistance, R_p. The R_p can be determined from the Nyquist or Bode plots that are generated by the Gamry Analyst software using the EIS data. Figure 17 shows a Nyquist and Bode plot and shows how the R_p can be measured on each plot.

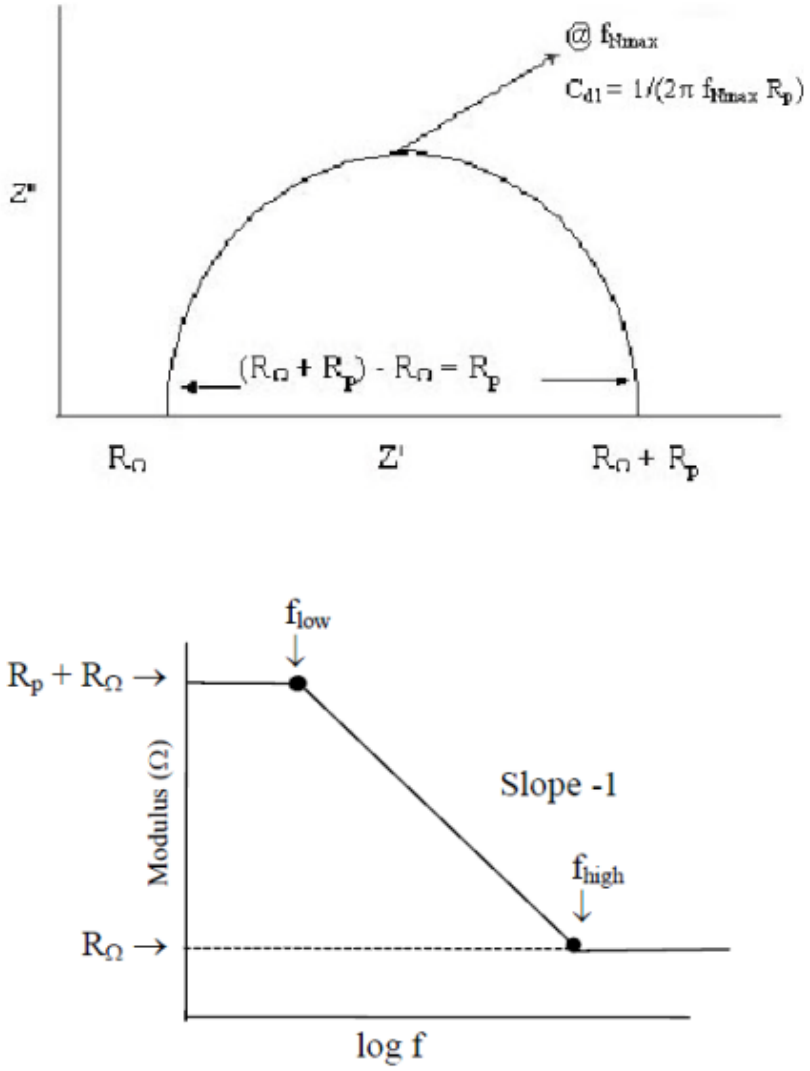

Figure 17. Nyquist (top) and Bode (bottom) Plots for finding the Polarization Resistance from a material that exhibits simple Randles circuit behavior. Figure taken from reference 19.

Once the R_p is measured it can be plugged into Equation 1 to find the corrosion current density, which can then be used in Equation 2 to determine the corrosion rate, in the same way that was

described for polarization resistance. Figure 18 shows the Bode plots for Sample 5-1 and how the R_p is measured from the plot.

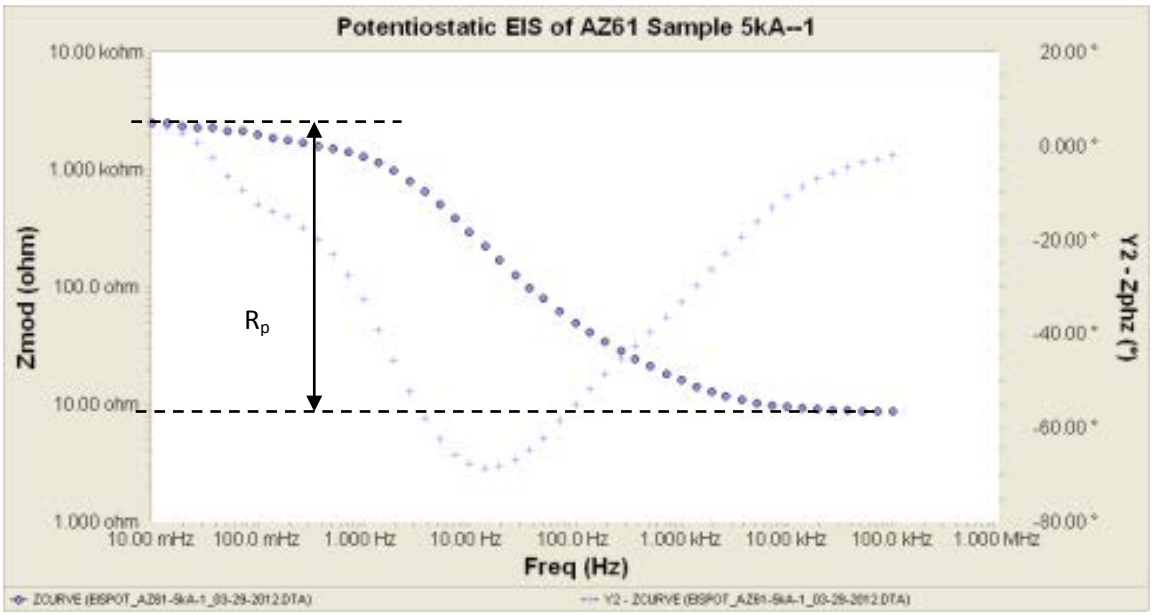

Figure 18. Bode Plot from EIS data for Sample 5-1. The double arrow line indicates how R_p is measure from the plot. The R_p is the difference between the upper and lower part of the impedance (Z) curve.

From this plot, the R_p value was measured to be 2448 ohms. R_p should have units of ohms*cm^2, so this value is normalized for area by multiplying it by the unmasked area of the sample, which was measured before beginning the experiment. 2448 ohms * 1.304 cm^2 = 3192.192 ohms*cm^2. This value is then plugged into Equation 1 to find the i_{corr}:

$$\frac{0.1 \times 0.1}{2.3\,(0.1 + 0.1)\,3192.192}$$

The i_{corr} is calculated to be 6.81µA. Equation 2 can now be used to determine the EIS corrosion rate:

$$\frac{0.129 \times 6.81 \times 12.4}{1.76}$$

The resulting corrosion rate is 6.19 mpy. This analysis was not performed by the Gamry software. Instead the R_p was measured as shown in Figure 18 and then that value was plugged into an excel spreadsheet that performed the remaining calculations. This process was repeated to find the EIS corrosion rate for each sample.

Results

During this research many thin films were fabricated by EBPVD and then tested. This section will give an overview of the films created and a more in depth analysis of selected films. Selected films were analyzed using SEM, open circuit potential, polarization resistance, EIS, and ICP. The analysis leads to a possible relationship between film thickness and corrosion rate that requires further investigation and testing.

Fabrication of Thin Films via EBPVD

Several thin films were fabricated for the testing of corrosion properties and analysis of the film structure using SEM. The chosen source material for deposition was bulk AZ61, which has a composition of 93% Mg, 6% Al, 1% Zn. Films were deposited at room temperature and at high vacuum ($3.8x10^{-6}$). The films were deposited at a rate of 20-25 Angstroms per second until the desired thickness was reached. During deposition the substrate was spinning in order for more uniform film grown to occur across the surface of the substrate. Table 2 shows all of the films that were created during this research. The Mg-Ti films were created for research on bioabsorbable implants. AZ61 films were chosen because AZ61 is commonly used in magnesium battery applications. Of the AZ61 films, the ones chosen for testing varied significantly in thickness and were fabricated specifically for this thesis research.

Table 2. Table of thin films fabricated. The Mg-Ti depositions were fabricated using a two electron gun deposition. Films from this chart were made for battery research as well as for bioabsorbable implant materials. The deposition rate is in Angstroms/second and the thickness of the films is given.

Metals Deposited	Deposition Rates (A/s)	Film Thickness (μm)
Mg-Ti	Mg: 24 Ti: 1	3.75
Mg-Ti	Mg: 24 Ti: 1.2	4.5
Mg-Ti	Mg: 15 Ti: 1.2	4.22
Mg-Ti	Mg: 11 Ti: 1.1	3.1
AZ61	AZ61: 24	7
AZ61	AZ61: 25	7
AZ61	AZ61: 25	7
Mg	Mg: 25	4.4
Mg	Mg: 23	7
Mg-Ti	Mg: 24 Ti: 1.1	6.3
Mg-Ti	Mg: 24 Ti: 1	6.5
Mg-Ti	Mg: 23 Ti: 1	4
Mg-Ti	Mg: 22 Ti: 1	5
AZ61	AZ61: 23	6.6
AZ61	AZ61: 24	1
AZ91	AZ91: 20	5
AZ91	AZ91: 20	5
Mg-Ti	Mg: 20 Ti: 1.1	4
AZ61	AZ61: 23	0.5
AZ61	AZ61: 24	2.1

This thesis will focus on 4 films that were deposited under the conditions mentioned above:

Sample 5 (5kA): The desired thickness of this film was 5kA; however, the thickness measured by the SEM was 3.01 microns (30.1 kA).

Sample 20: The desired thickness of this film was 20kA; however, the thickness measured by the SEM was 5.89 microns (58.9 kA).

Sample 148: The thickness measured by the SEM was 7.17 microns (71.7 kA).

Sample 149: The thickness measured by the SEM was 7.79 microns (77.9 kA).

Figure 19 shows the cross-section of a cleaved sample for each film analyzed. From these images the thickness of each film was determined. By measuring and comparing the thicknesses and structure of the films a relationship can be determined between corrosion rate and film thickness. The analysis of these films will also provide an idea about the consistency of the corrosion behavior across different depositions and whether the corrosion behavior is reproducible from film-to-film.

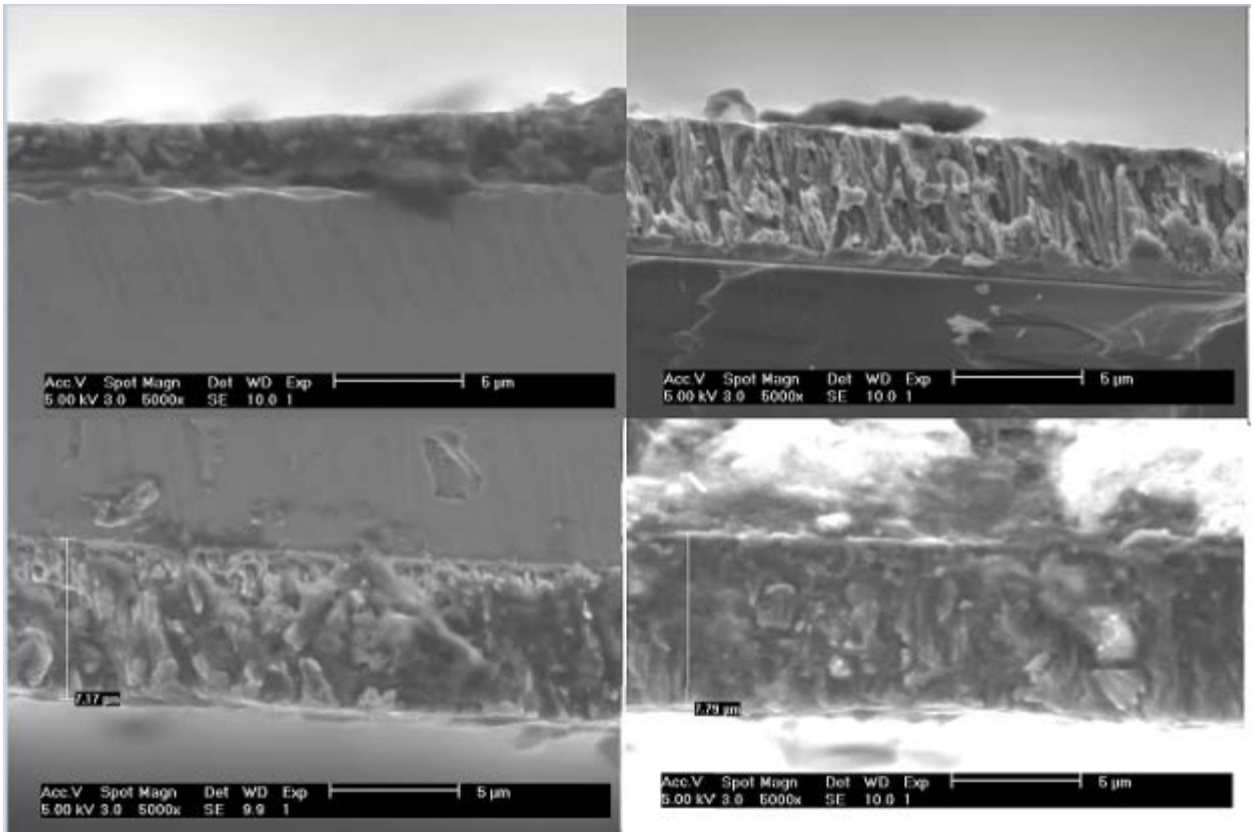

Figure 19. Cross-sectional SEM of Sample 5 (Top Left), Sample 20 (Top Right), Sample 148 (Bottom Left) and Sample 149 (Bottom Right). These images were used to measure the thickness of the films. The structure can also be seen from the side view. Note that the images on the bottom row are flipped so that the substrate is on top of the film.

SEM Analysis

SEM was used to image the surface and edges of thin film samples to study the morphology of the film and to accurately measure the thickness of the film. Previous research has shown that pure magnesium thin films show 3D nucleation or island growth mode [20]. The growth of a pure magnesium film (deposited via EBPVD), immediately at the beginning of a deposition, can be seen in Figure 20A. Evolution in growth of the film is seen as one moves from A to D in the Figure. In Figure 20-D the hexagonal surface structure that is characteristic of pure magnesium thin films can be seen.

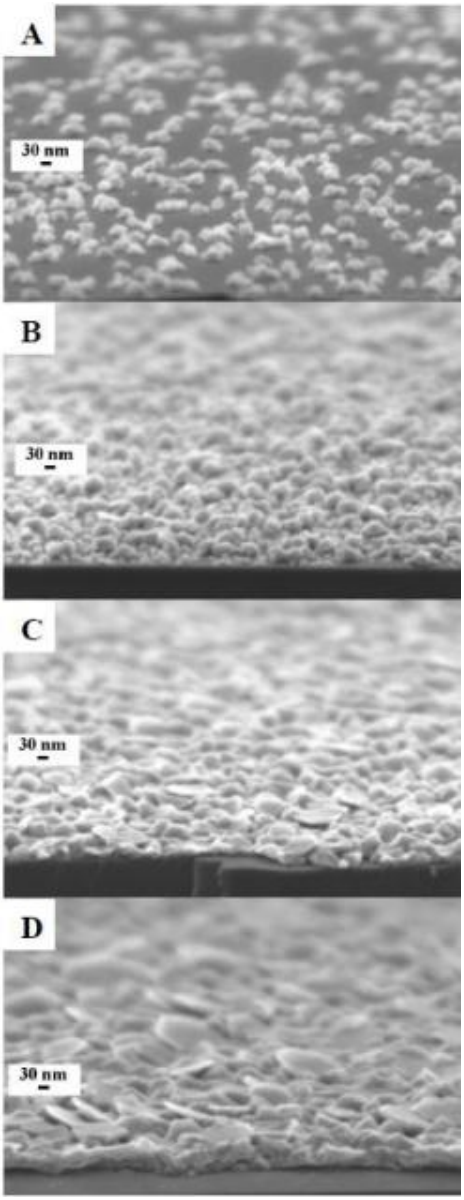

Figure 20. Growth of pure magnesium thin film at low thickness. The film was grown at 10 Angstroms/second and imaged at 2 minute intervals with FESEM starting with image A. Pictures taken from reference 20.

When the AZ61 films were imaged in the SEM, a growth pattern was observed that was almost identical to that of the pure magnesium films shown in previous research. The films formed the hexagonal structures that are characteristic of pure magnesium films, resulting in a high surface area. This structure can be seen in Figure 21, Figure 22, and Figure 23. Figure 21 shows a comparison of the surface of 3 films of different thicknesses at different magnifications. It appears that the hexagonal structures become more defined with increasing film thickness and the film surface has more depth, resulting in more surface area. Figure 22 and Figure 23 show 3.01 µm and 7.79 µm-thick films respectively, at 10000X magnification and the difference in surface structure can be clearly seen. This increase in surface area could explain the higher corrosion rate of the thicker films. The corrosion rate calculations are dependent on area and the area used in the corrosion rate calculations in this thesis were based on the apparent area and not the actual surface area.

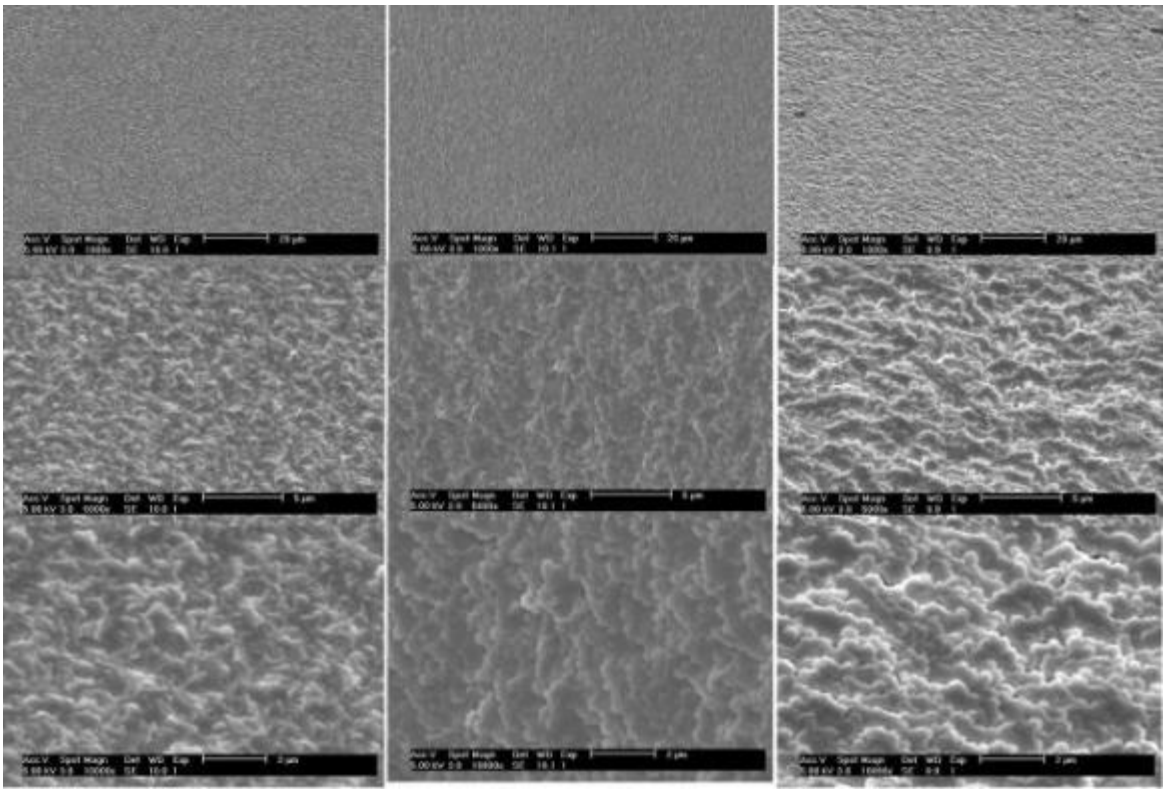

Figure 21. Comparison of AZ61 EBPVD thin films. 3.01 µm film(left), 5.89 µm (middle), and 7.79 µm (right). The magnification is 1000X, 5000X and 10000X from top to bottom and the markers are 20 µm, 5 µm and 2 µm respectively.

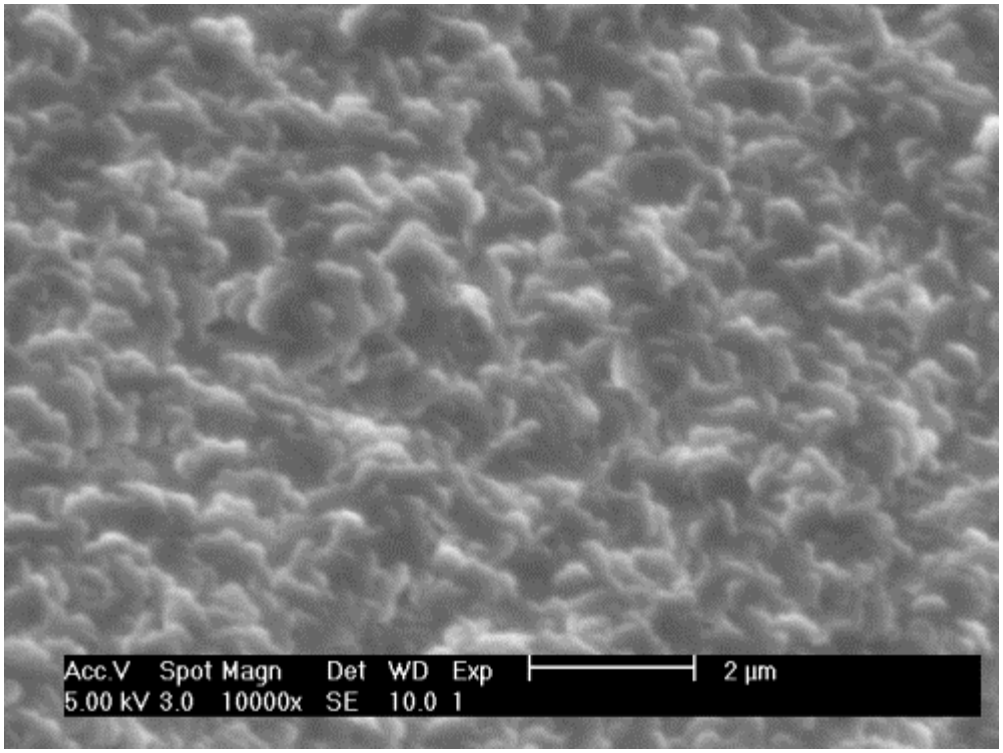

Figure 22. SEM Image of 3.01 µm thick film (Sample 5) at 10000X magnification

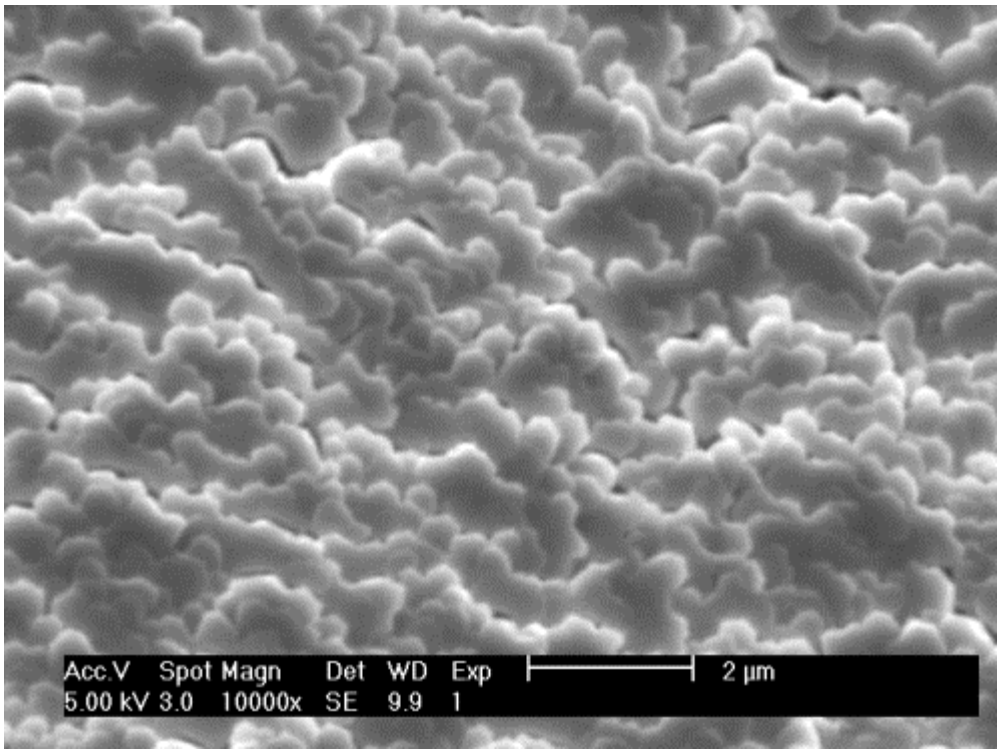

Figure 23. SEM Image of 7.79 µm thick film (Sample 149) at 10000X magnification

Electrochemical Analysis

Electrochemical analysis allowed the corrosion rates of the thin films to be calculated and compared. Corrosion rates were determined using polarization resistance and EIS with an experimental setup as described in the Experimental Section. Open circuit potential experiments were run before each set of polarization resistance and EIS experiments. The open circuit potential for all films range from -1.88 V vs. SCE to -1.77 V vs. SCE. All tests were conducted 3 or more times for each film. The results for Sample 5 are displayed in Table 3. The results for this film fell within an acceptable range for corrosion data, which is one order of magnitude. The corrosion rates from polarization resistance were within a factor of 2 and the corrosion rates from EIS were also within a factor of 2.This film had the lowest corrosion rates of all the films tested. Figure 24 compares the corrosion rates of each sample tested and the average corrosion rates of the film which provides a visual representation of the range of corrosion values measured.

Table 3. Data from electrochemical measurements conducted on AZ61 EBPVD thin film sample 5.

Table of Measured Data for Sample 5			
AZ61 Sample	**Sample 5--1**	**Sample 5--2**	**Sample 5--3**
Area (cm^2)	1.304	1.350	0.702
Open Circuit Potential (V vs SCE)	-1.85	-1.88	-1.82
R_p from Polarization Resistance ($ohm*cm^2$)	2234.00	3048.00	1684.00
i_{corr} from PR (Amps)	9.72E-06	7.12E-06	1.29E-05
Corrosion Rate from Polarization Resistance (mpy)	8.82	6.46	11.70
R_p from Bode Plot ($ohm*cm^2$)	3192.19	3688.20	2010.66
i_{corr} from EIS (Amps)	6.81E-06	5.89E-06	1.08E-05
Corrosion Rate from EIS (mpy)	6.19	5.36	9.83

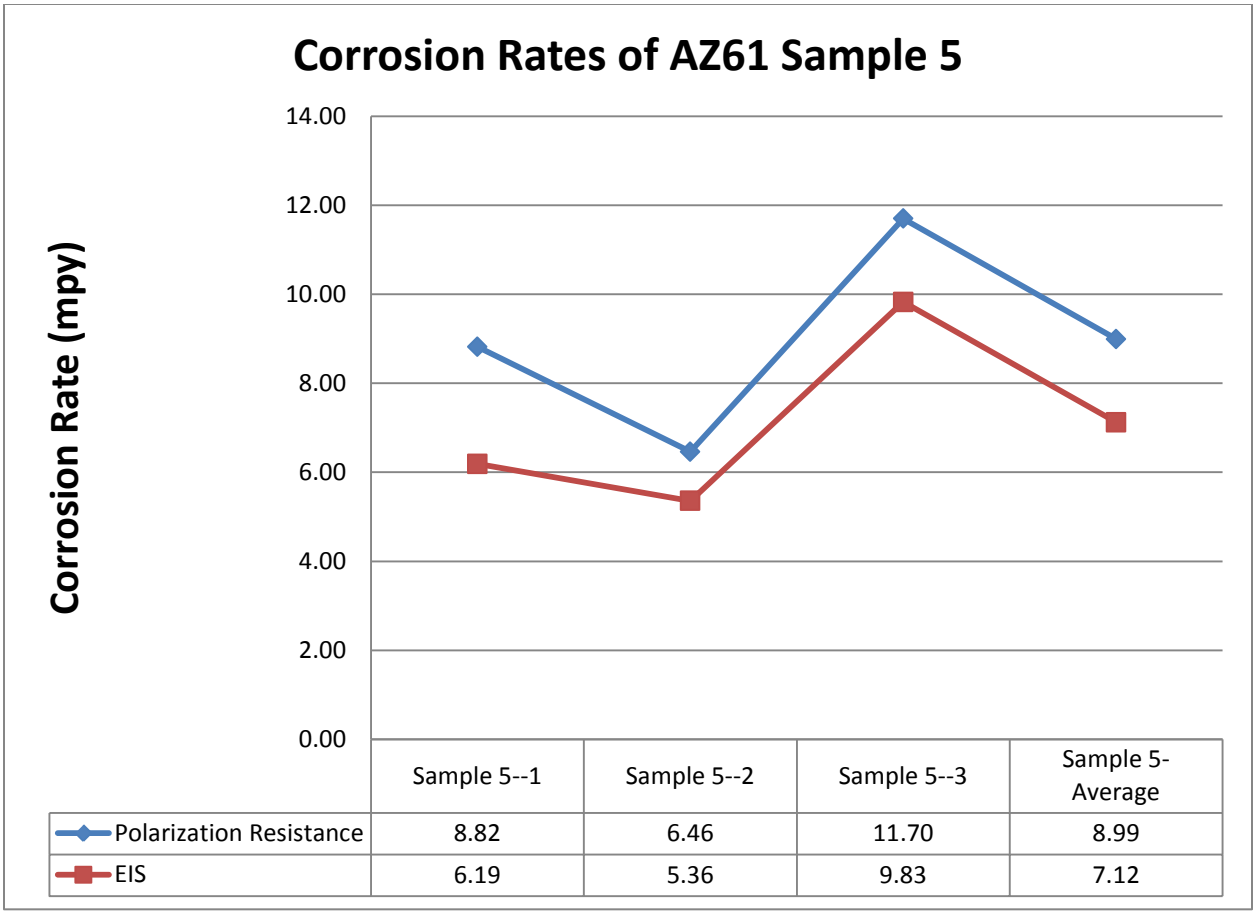

Figure 24. Corrosion data for sample 5. Electrochemical measurements were taken with a Gamry Reference 3000 Potentiostat in artificial seawater at ambient lab temperature (25°C).

The electrochemical results for Sample 20 are shown in Table 4. The corrosion rates for Sample 20 were very consistent. Corrosion rates from polarization resistance were within 18% of one another and the corrosion rates from EIS were within 23% of one another. The corrosion rates are graphed in Figure 25, and it was observed that the corrosion rates for each test are nearly at the same value in mpy.

Table 4. Data from electrochemical measurements conducted on AZ61 EBPVD thin film sample 20.

Table of Measured Data for Sample 20			
AZ61 Sample	Sample 20--1	Sample 20--2	Sample 20--3
Area (cm^2)	0.862	0.880	0.490
Open Circuit Potential (V vs SCE)	-1.87	-1.88	-1.85
R_p from Polarization Resistance (ohm*cm^2)	1474.00	1497.00	1434.00
i_{corr} from PR (Amps)	1.47E-05	1.45E-05	1.51E-05
Corrosion Rate from Polarization Resistance (mpy)	13.36	13.04	11.34
R_p from Bode Plot (ohm*cm^2)	1976.62	2107.60	1719.48
i_{corr} from EIS (Amps)	1.10E-05	1.03E-05	1.26E-05
Corrosion Rate from EIS (mpy)	10.00	9.37	11.49

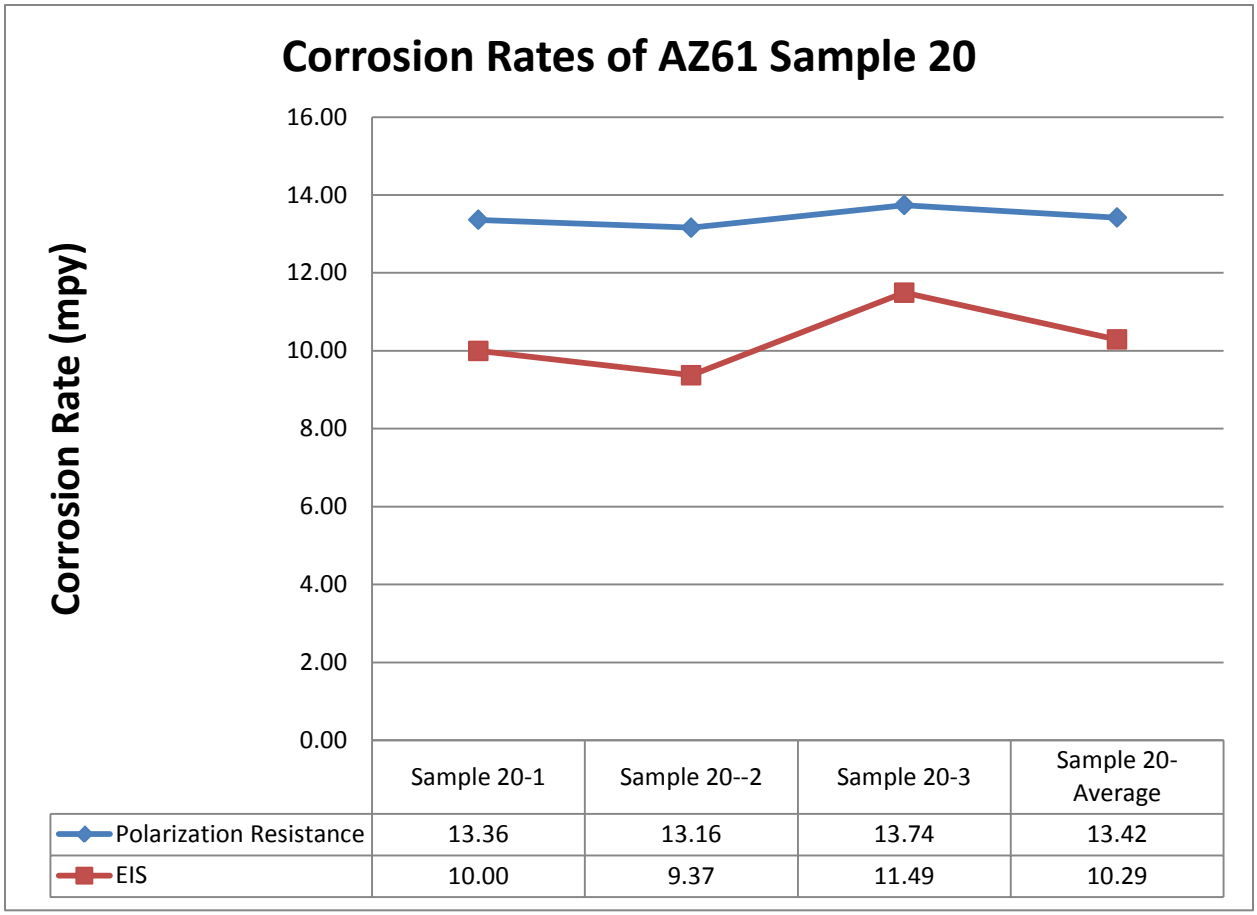

Figure 25. Corrosion data for sample 20. Electrochemical measurements were taken with a Gamry Reference 3000 Potentiostat in artificial seawater at ambient lab temperature (25°C).

Thin films 5 and 20 provided very consistent corrosion rates from sample to sample, with the EIS results being particularly stable. Sample 20 has slightly higher corrosion rates given by polarization resistance, but the corrosion rates determined using EIS are nearly identical. The slightly higher

corrosion rate of the thicker film could be due to the higher surface area that was seen in the SEM imaging.

Electrochemical tests were also performed on the thicker films 148 and 149 [21]. By adding these films into the analysis the trend of increasing corrosion rate with increasing thickness can be more easily observed. The electrochemical results for Sample 148 are shown in Table 5. The results for the thicker samples varied more than those for the thinner samples discussed previously. The corrosion rates for Sample 148 varied significantly, but were still within an order of magnitude of one another.

Table 5. Data from electrochemical measurements conducted on AZ61 EBPVD thin film sample 148. Data taken from reference 21.

Table of Measured Data for Sample 148					
AZ61 Sample	**148 -1**	**148-4**	**148-5**	**148-6**	**148-7**
Area (cm^2)	0.37	0.13	0.49	0.66	0.87
Open Circuit Potential (V vs SCE)	-1.83	-1.77	-1.82	-1.86	-1.83
Corrosion Rate from Polarization Resistance (mpy)	20.80	49.68	13.91	8.70	11.47
R_p from Bode Plot (ohm*cm^2)	1860.00	665.00	2430.00	3290.00	4370.00
i_{corr} from EIS (micro-Amps)	11.67	32.69	8.97	6.62	4.98
Corrosion Rate from EIS (mpy)	10.62	29.75	8.16	6.02	4.53

The results for Sample 149 are shown in Table 6. This film showed the highest corrrosion rates. The corrosion rates found using polarization resistance were within 10%. The corrosion rates measured with EIS were lower and within a factor of 5.

Table 6. Data from electrochemical measurements conducted on AZ61 EBPVD thin film sample 149. Data taken from reference 21.

Table of Measured Data for Sample 149			
AZ61 Sample	**149-1**	**149-4**	**149-5**
Area (cm^2)	0.34	0.76	0.18
Open Circuit Potential (V vs SCE)	-1.82	-1.84	-1.77
Corrosion Rate from Polarization Resistance (mpy)	23.24	22.80	24.97
R_p from Bode Plot (ohm*cm^2)	1690.00	3820.00	900.00
i_{corr} from EIS (micro-Amps)	12.86	5.69	24.16
Corrosion Rate from EIS (mpy)	11.64	5.16	21.90

The corrosion rates for each film sample were averaged so that the corrosion rates for each film could be compared. Figure 26 shows a comparision of the average corrosion rates for all of the AZ61 samples tested. The chart shows a trend of increasing corrosion rate with increasing film thickness. The EIS corrosion rates did not vary as significantly as the polarization resistance corrosion rates from film to

film. Figure 27 is a graph of average corrosion rate vs. thickness for each sample and clearly shows that the corrosion rate increases with the thickness of the film.

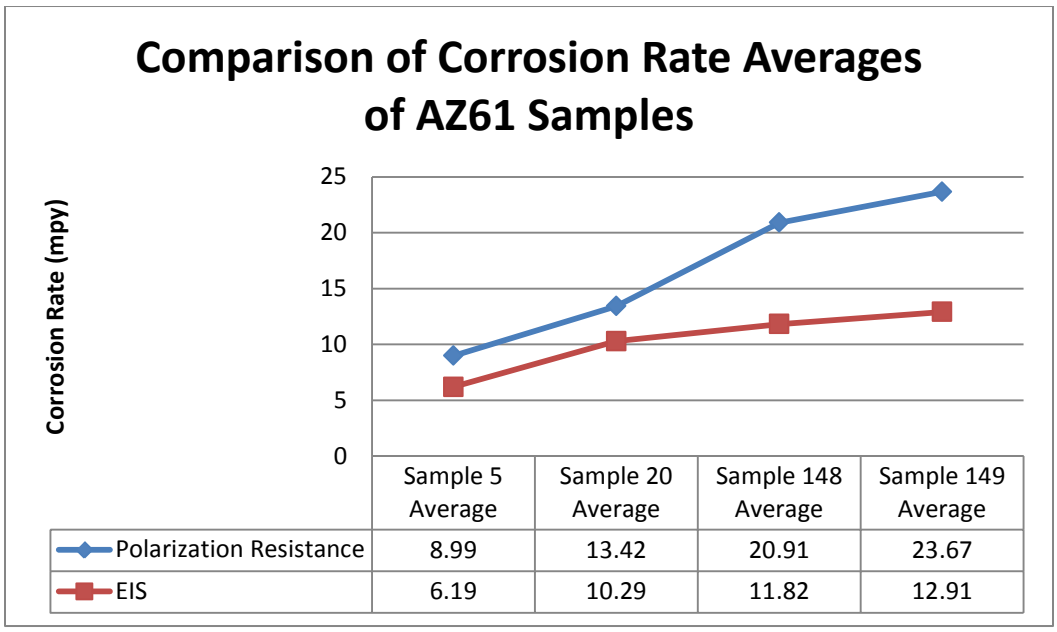

Figure 26. Comparison of Average Corrosion rates of AZ61 samples. Electrochemical measurements were taken with a Gamry Reference 3000 Potentiostat in artificial seawater at ambient lab temperature (25°C).

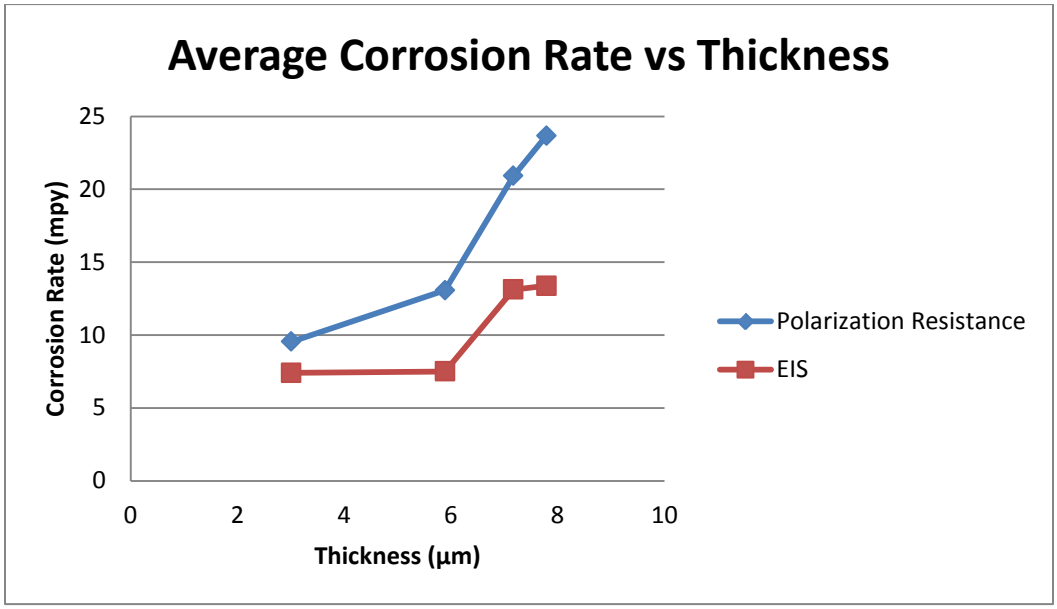

Figure 27. Average Corrosion Rate vs Thickness of AZ61 thin films. This diagram shows the average corrosion rates for each sample on a plot vs thickness. Electrochemical measurements were taken with a Gamry Reference 3000 Potentiostat in artificial seawater at ambient lab temperature (25°C).

The corrosion rates of the thin films that were studied were only slightly higher than that of the bulk AZ61 material, which was found to have corrosion rate of 5.79 mpy by polarization resistance and 5.35 mpy by EIS. This is surprising because we would expect the corrosion rate of the thin films to be higher because of the lower amount of Al and Zn in their composition. The reason that the thin films have a lower corrosion rate than expected may be due to the fact that the Al and Zn are in solid solution and do no form a precipitate, which degrades corrosion performance, like they do in a bulk material.

Inductively Coupled Plasma Atomic Emission Spectroscopy

ICP was performed on bulk AZ31, AZ61, and AZ31 as well was 3 AZ61 thin films (samples 148, 149 and 150). Table 7 presents the data obtained from ICP conducted on the alloys studied in this thesis.

Table 7. ICP data for AZ61 bulk materials and thin films.

Sample	Wt% Mg	Wt% Al	Wt% Zn	Equivalent Weight (g)	Alloy Density(g/cm^3)
AZ31	0.9794	0.0150	0.0055	12.22	1.75
AZ61	0.9993	0.0007	0.0001	12.15	1.74
AZ91	0.9564	0.0397	0.0040	12.11	1.77
148	0.9851	0.0032	0.0116	12.38	1.76
149	0.9815	0.0076	0.0108	12.35	1.76
150	0.9819	0.0089	0.0092	12.31	1.76

It was observed that the concentrations of Al and Zn in all of the alloys tested were lower than indicated by the name of the material. For the AZ61 thin films the Al was less than 1% wt. and the Zn was close to 1% wt. although the expected composition was 6% Al and 1% Zn. This is likely due to the difference in vapor pressures and melting temperatures for Mg, Al, and Zn. This explains why the AZ61 films have behaved so much like pure Mg films. The equivalent weight and alloy density were determined using ICP and the values of 12.4 grams for the equivalent weight and 1.76 grams/cm^3 were used for all of the AZ61 thin films tested.

Conclusions and Future Work

The analysis of thin films deposited from bulk AZ61 revealed that the films show fairly consistent and reproducible corrosion results and structure from film-to-film. This is important because production of a magnesium anode for use in a battery would require the ability to consistently reproduce the desired product. Corrosion rates were shown to be very similar for samples from the same thin-film, which is evidence of a consistent and uniform structure across the surface of the film, which could also be observed in SEM images.

It was observed that corrosion rate increases with increasing film thickness. This is likely due to an increase in surface area as the film grows. This relationship could be studied further by testing films in a wider range of thickness to see if the trend continues. More precise imaging can be done at the surface to get a clearer picture of how the surface structure changes with increasing thickness. To confirm that the thicker films actually do have a larger surface area further testing needs to be done. FESEM and XRD could provide more information about the surface and structure of the film. More films of varying thickness should be made and tested to provide a wider range of data for the corrosion rate vs. thickness relationship. Furthermore, considering that very little alloy is present in the films, it would be interesting to evaluate whether alloy composition affects this trend of increased corrosion rate with increased film thickness.

ICP showed that the AZ61 composition did not carry over from the bulk source material and the Al concentration was particularly low. In future work, an effort can be made to produce magnesium alloys with a higher composition of Al and Zn. One method of doing this would be to use the second gun in the chamber to vaporize Mg and Al or Mg and Zn separately. This would allow for the creation of binary films with some control over the concentration of the alloying element. Another approach would be to melt Al and Zn together in a crucible and then vaporize them together to perform a ternary deposition so that Mg, Al and Zn can be incorporated into the film in desired proper proportions.

Appendix A: Collection of Electrochemical Graphs

This Appendix contains graphs from each stage of the electrochemical testing for each of film samples 5 and 20. For each film the graphs are in order that the experiments were conducted which is OCP, polarization resistance, EIS, and then OCP again.

Sample 5-1

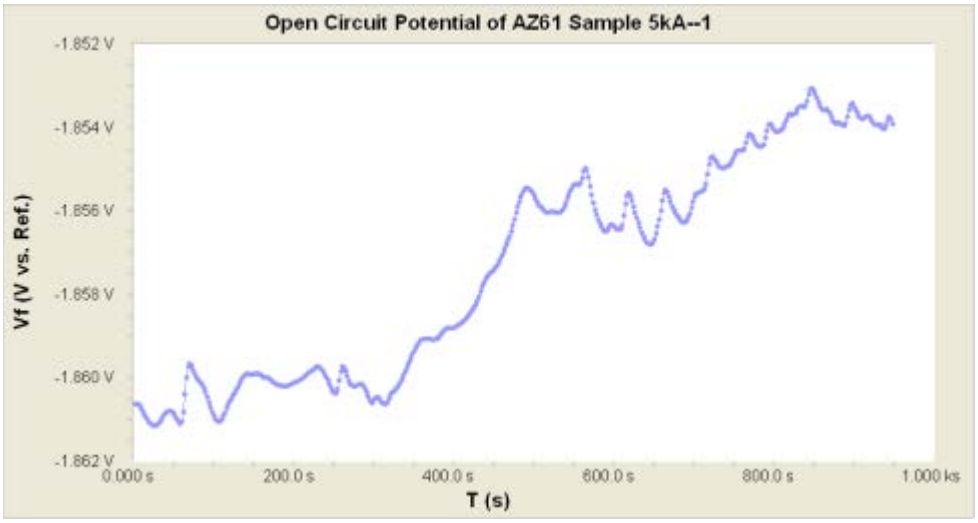

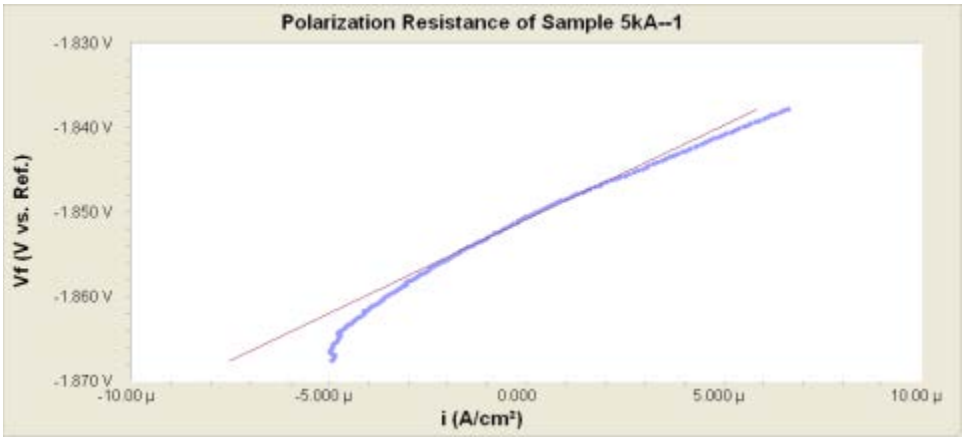

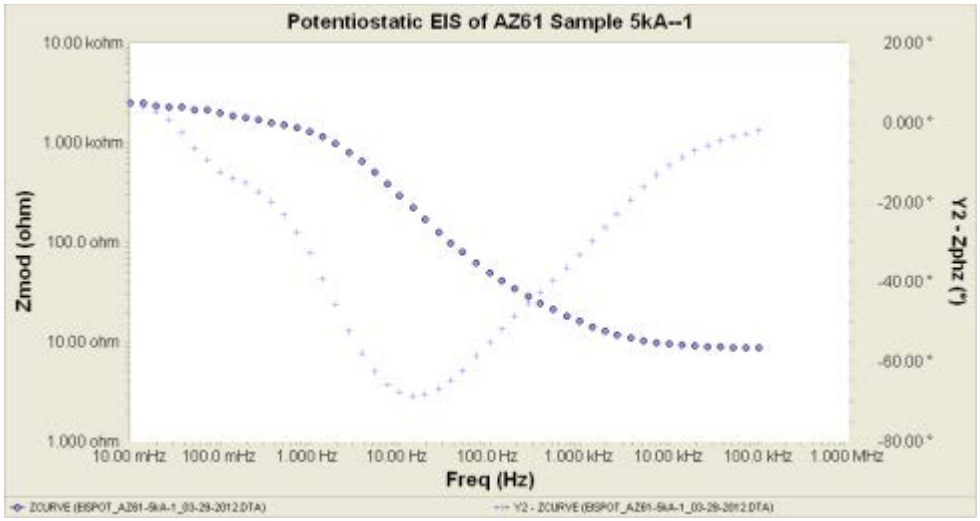
Potentiostatic EIS of AZ61 Sample 5kA--1
10.00 kohm
1.000 kohm
100.0 ohm
10.00 ohm
1.000 ohm
Zmod (ohm)
20.00 °
0.000 °
-20.00 °
-40.00 °
-60.00 °
-80.00 °
Y2 - Zphz (°)
10.00 mHz
100.0 mHz
1.000 Hz
10.00 Hz
100.0 Hz
1.000 kHz
10.00 kHz
100.0 kHz
1.000 MHz
Freq (Hz)
ZCURVE (BSPOT_AZ61-5kA-1_03-29-2012.DTA)
Y2 - ZCURVE (BSPOT_AZ61-5kA-1_03-29-2012.DTA)

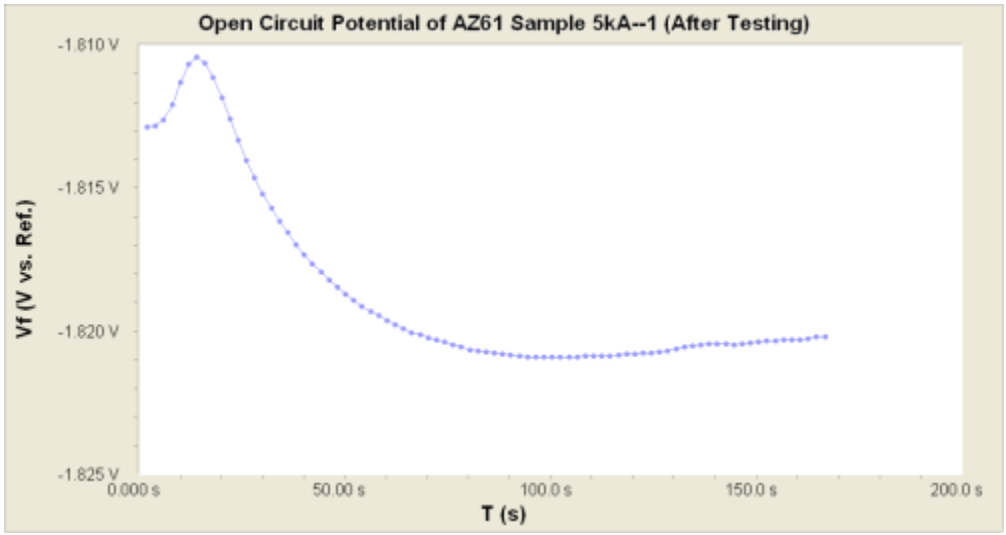
Open Circuit Potential of AZ61 Sample 5kA--1 (After Testing)
-1.810 V
-1.815 V
-1.820 V
-1.825 V
Vf (V vs. Ref.)
0.000 s
50.00 s
100.0 s
150.0 s
200.0 s
T (s)

Sample 5-2

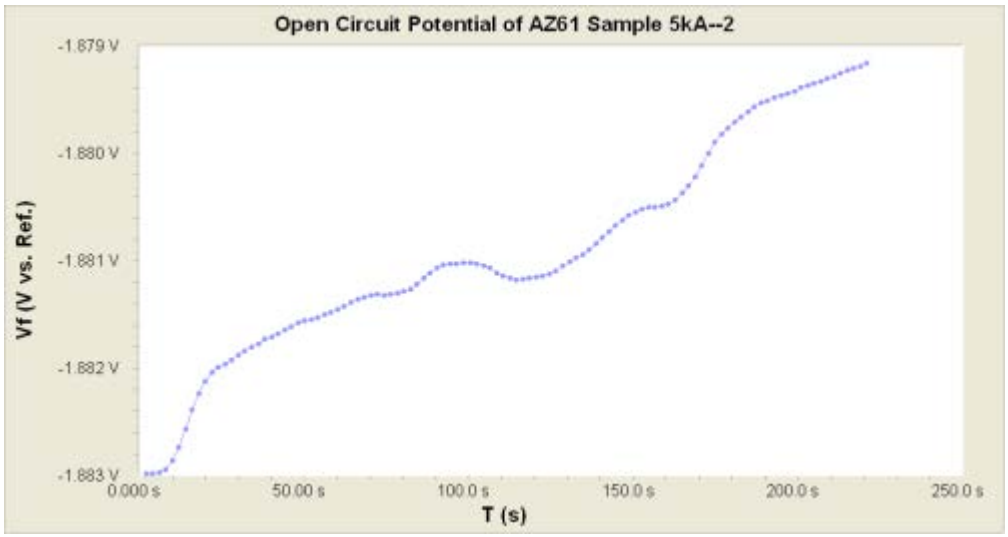
Open Circuit Potential of AZ61 Sample 5kA--2
-1.879 V
-1.880 V
-1.881 V
-1.882 V
-1.883 V
Vf (V vs. Ref.)
0.000 s
50.00 s
100.0 s
150.0 s
200.0 s
250.0 s
T (s)

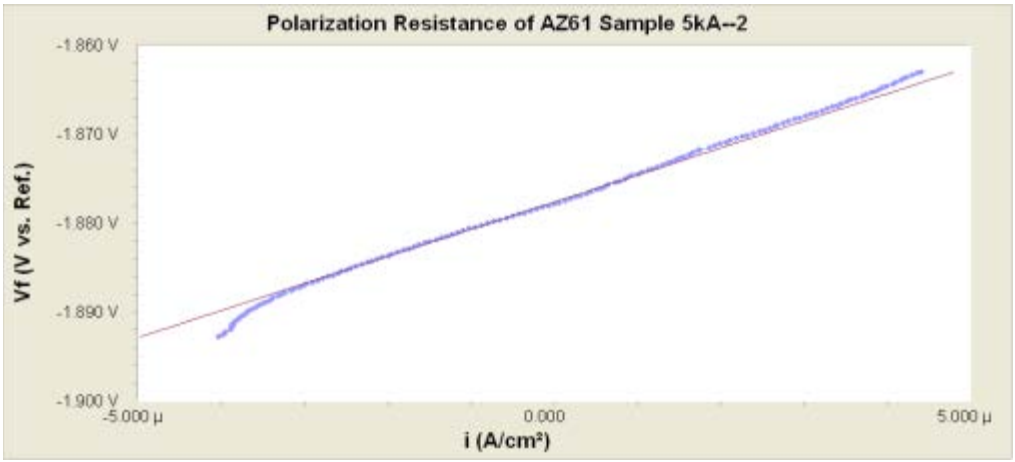
Polarization Resistance of AZ61 Sample 5kA--2
-1.860 V
-1.870 V
-1.880 V
-1.890 V
-1.900 V
Vf (V vs. Ref.)
-5.000 µ
0.000
5.000 µ
i (A/cm²)

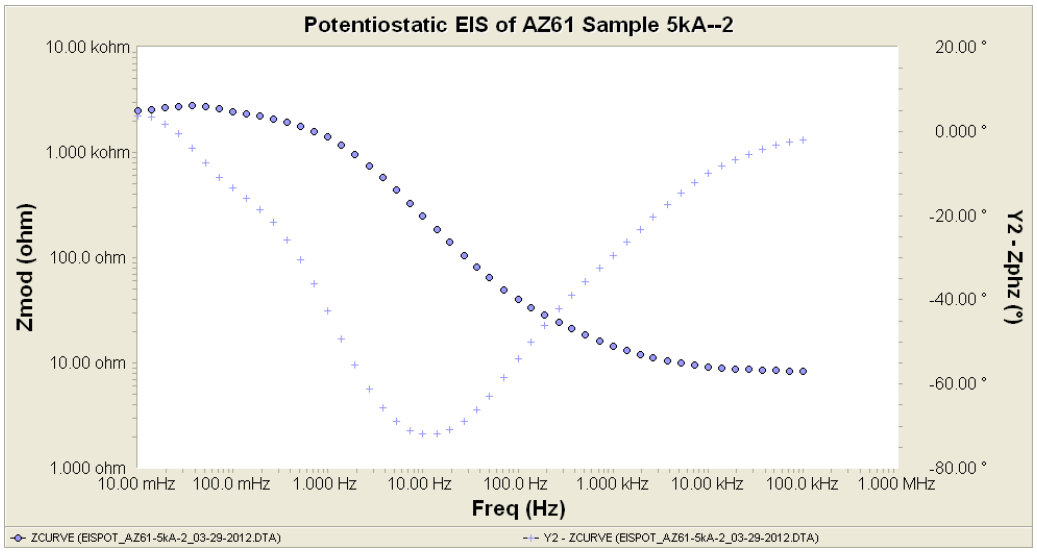
Potentiostatic EIS of AZ61 Sample 5kA--2
10.00 kohm
1.000 kohm
100.0 ohm
10.00 ohm
1.000 ohm
Zmod (ohm)
20.00 °
0.000 °
-20.00 °
-40.00 °
-60.00 °
-80.00 °
Y2 - Zphz (°)
10.00 mHz
100.0 mHz
1.000 Hz
10.00 Hz
100.0 Hz
1.000 kHz
10.00 kHz
100.0 kHz
1.000 MHz
Freq (Hz)
ZCURVE (EISPOT_AZ61-5kA-2_03-29-2012.DTA)
Y2 - ZCURVE (EISPOT_AZ61-5kA-2_03-29-2012.DTA)

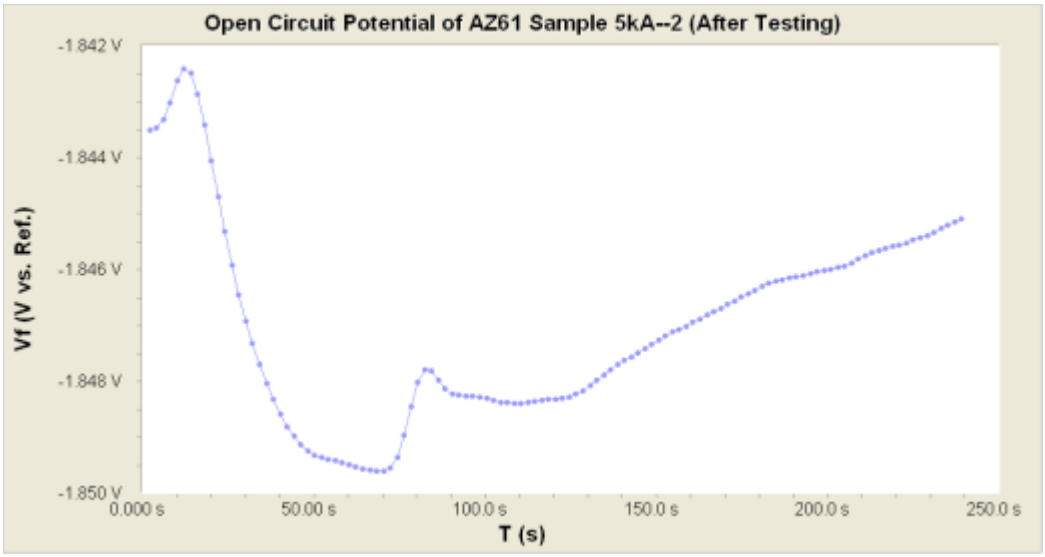
Open Circuit Potential of AZ61 Sample 5kA--2 (After Testing)
-1.842 V
-1.844 V
-1.846 V
-1.848 V
-1.850 V
Vf (V vs. Ref.)
0.000 s
50.00 s
100.0 s
150.0 s
200.0 s
250.0 s
T (s)

Sample 5-3

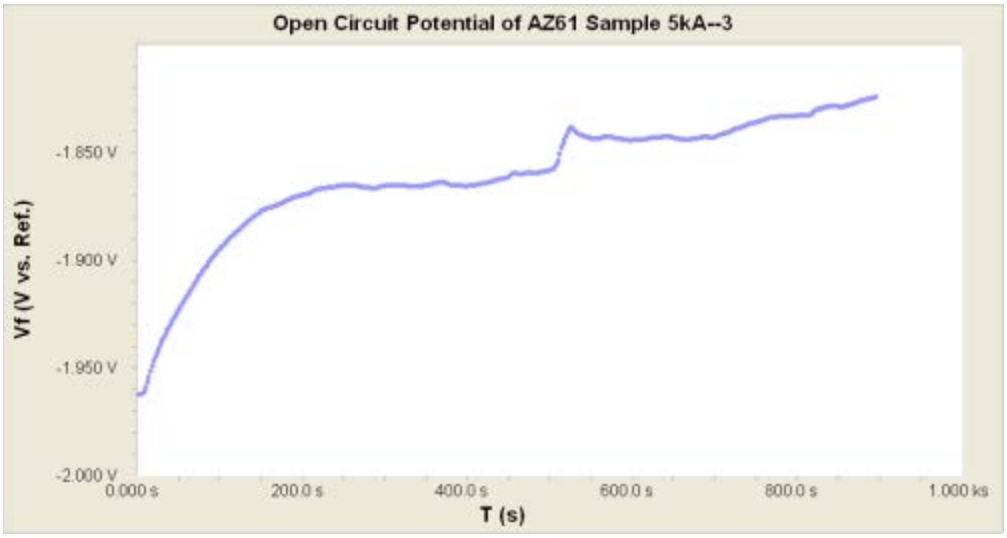
Open Circuit Potential of AZ61 Sample 5kA--3
Vf (V vs. Ref.)
-1.850 V
-1.900 V
-1.950 V
-2.000 V
0.000 s
200.0 s
400.0 s
600.0 s
800.0 s
1.000 ks
T (s)

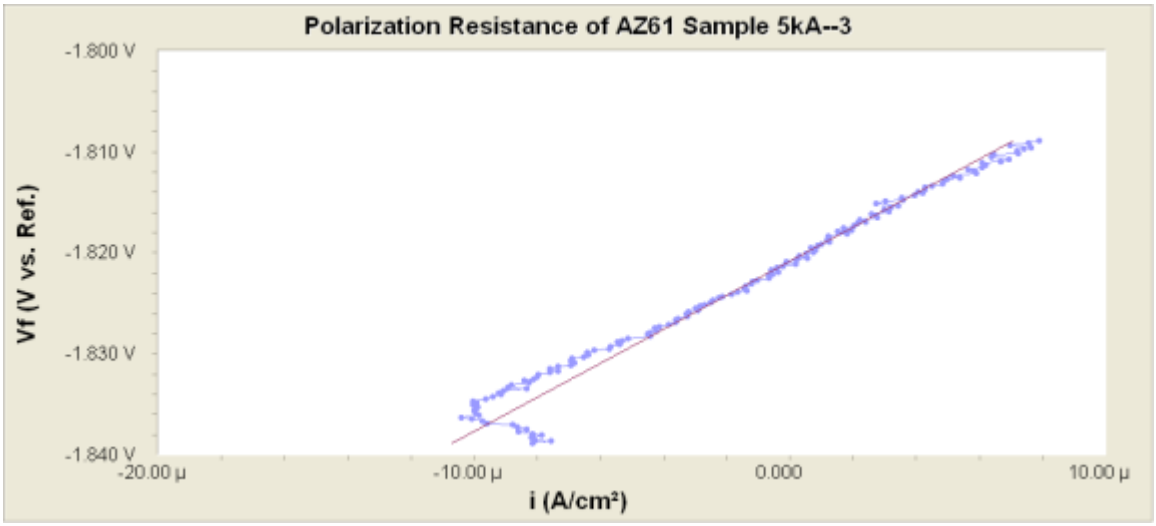
Polarization Resistance of AZ61 Sample 5kA--3
Vf (V vs. Ref.)
-1.800 V
-1.810 V
-1.820 V
-1.830 V
-1.840 V
-20.00 µ
-10.00 µ
0.000
10.00 µ
i (A/cm²)

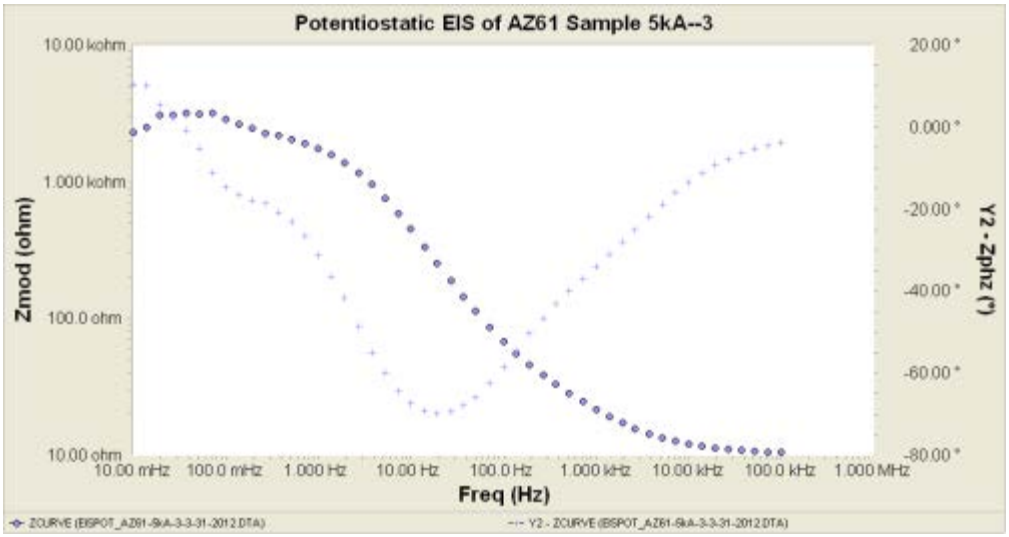
Potentiostatic EIS of AZ61 Sample 5kA--3
Zmod (ohm)
10.00 kohm
1.000 kohm
100.0 ohm
10.00 ohm
Y2 - Zphz (°)
20.00 °
0.000 °
-20.00 °
-40.00 °
-60.00 °
-80.00 °
10.00 mHz
100.0 mHz
1.000 Hz
10.00 Hz
100.0 Hz
1.000 kHz
10.00 kHz
100.0 kHz
1.000 MHz
Freq (Hz)
ZCURVE (BSPOT_AZ61-5kA-3-3-31-2012.DTA)
Y2 - ZCURVE (BSPOT_AZ61-5kA-3-3-31-2012.DTA)

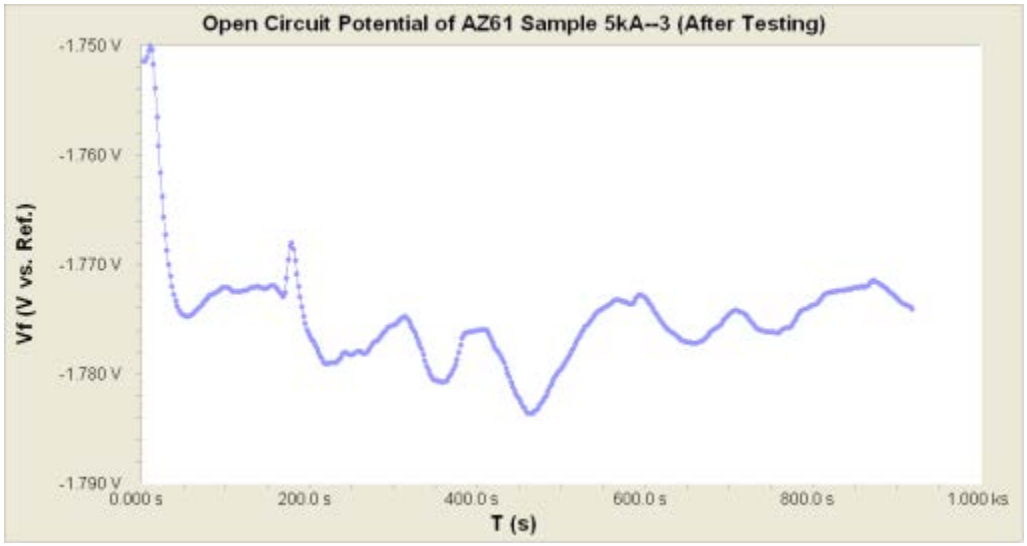
Open Circuit Potential of AZ61 Sample 5kA--3 (After Testing)
-1.750 V
-1.760 V
-1.770 V
-1.780 V
-1.790 V
Vf (V vs. Ref.)
0.000 s
200.0 s
400.0 s
600.0 s
800.0 s
1.000 ks
T (s)

Sample 20-1

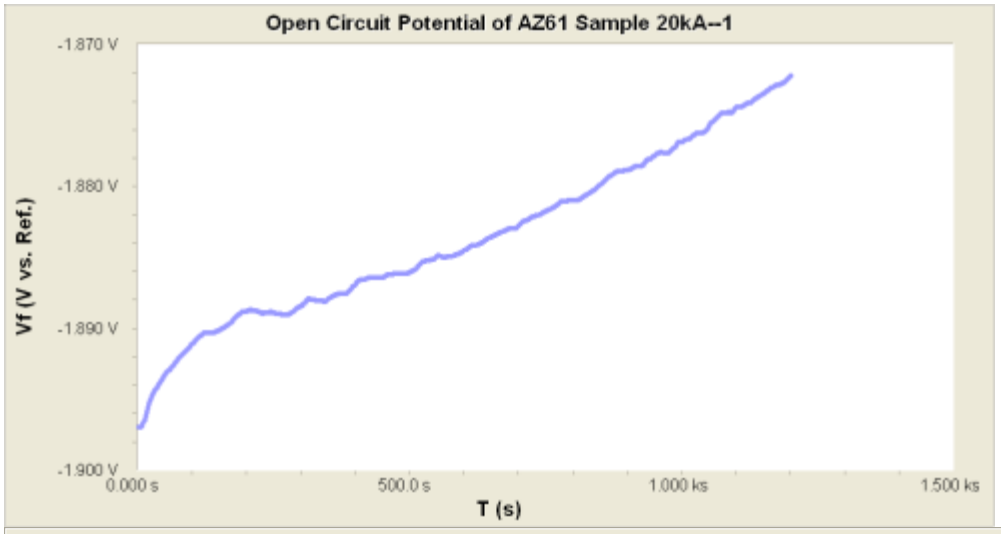
Open Circuit Potential of AZ61 Sample 20kA--1
-1.870 V
-1.880 V
-1.890 V
-1.900 V
Vf (V vs. Ref.)
0.000 s
500.0 s
1.000 ks
1.500 ks
T (s)

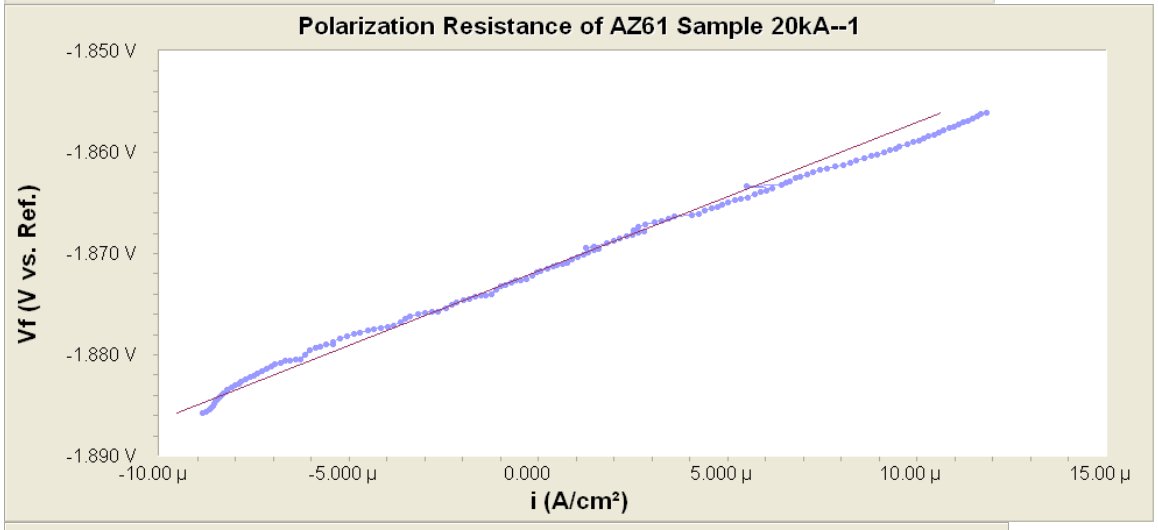
Polarization Resistance of AZ61 Sample 20kA--1
-1.850 V
-1.860 V
-1.870 V
-1.880 V
-1.890 V
Vf (V vs. Ref.)
-10.00 µ
-5.000 µ
0.000
5.000 µ
10.00 µ
15.00 µ
i (A/cm²)

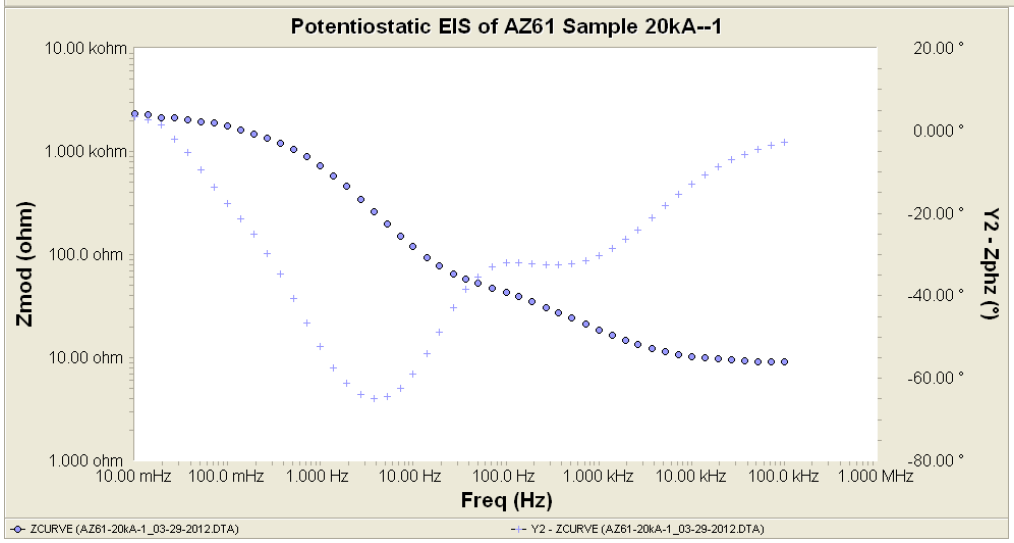
Potentiostatic EIS of AZ61 Sample 20kA--1
10.00 kohm
1.000 kohm
100.0 ohm
10.00 ohm
1.000 ohm
Zmod (ohm)
20.00 °
0.000 °
-20.00 °
-40.00 °
-60.00 °
-80.00 °
Y2 - Zphz (°)
10.00 mHz
100.0 mHz
1.000 Hz
10.00 Hz
100.0 Hz
1.000 kHz
10.00 kHz
100.0 kHz
1.000 MHz
Freq (Hz)
ZCURVE (AZ61-20kA-1_03-29-2012.DTA)
Y2 - ZCURVE (AZ61-20kA-1_03-29-2012.DTA)

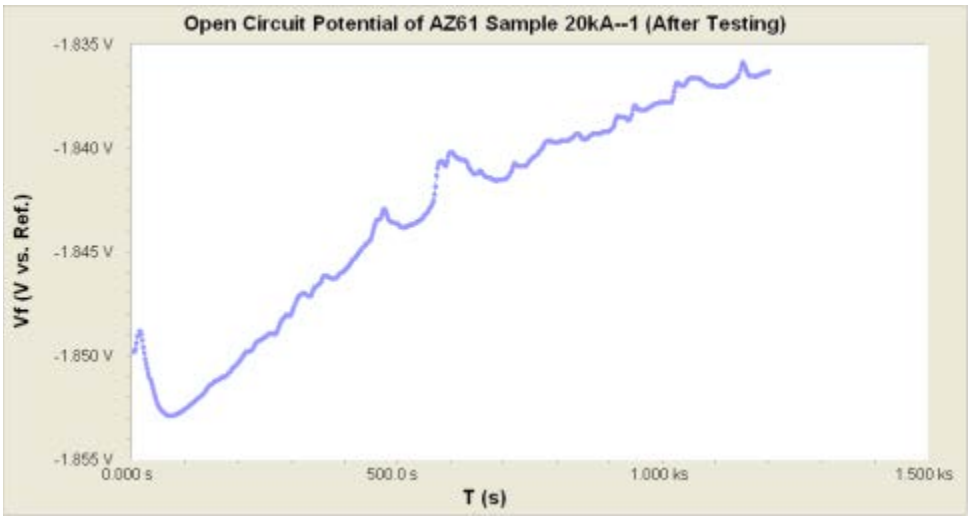
Open Circuit Potential of AZ61 Sample 20kA--1 (After Testing)
-1.835 V
-1.840 V
-1.845 V
-1.850 V
-1.855 V
Vf (V vs. Ref.)
0.000 s
500.0 s
1.000 ks
1.500 ks
T (s)

Sample 20-2

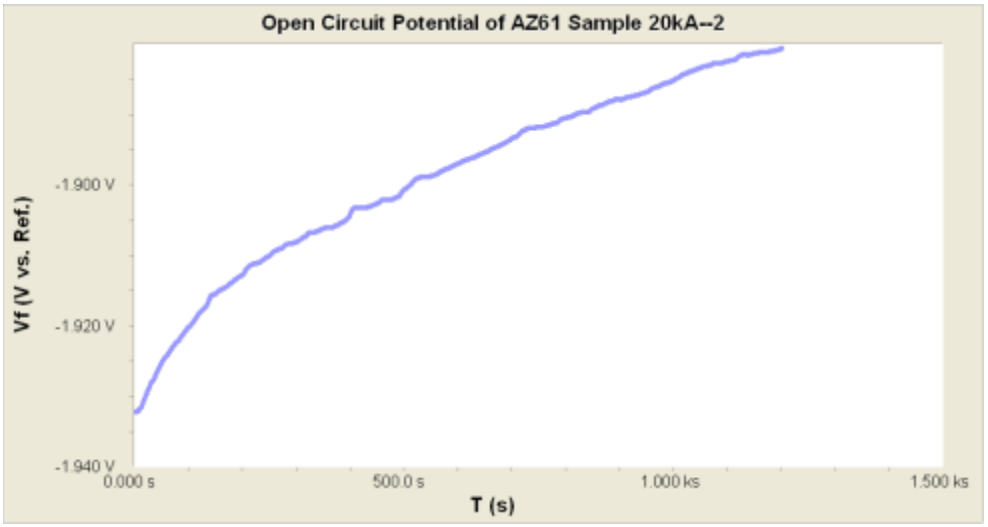
Open Circuit Potential of AZ61 Sample 20kA--2
Vf (V vs. Ref.)
-1.900 V
-1.920 V
-1.940 V
0.000 s
500.0 s
1.000 ks
1.500 ks
T (s)

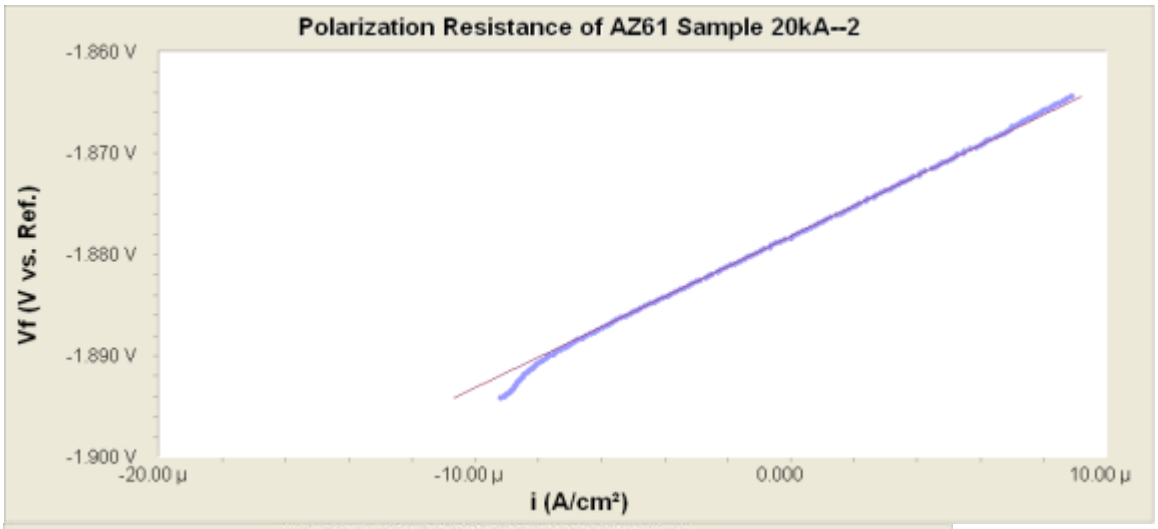
Polarization Resistance of AZ61 Sample 20kA--2
Vf (V vs. Ref.)
-1.860 V
-1.870 V
-1.880 V
-1.890 V
-1.900 V
-20.00 µ
-10.00 µ
0.000
10.00 µ
i (A/cm²)

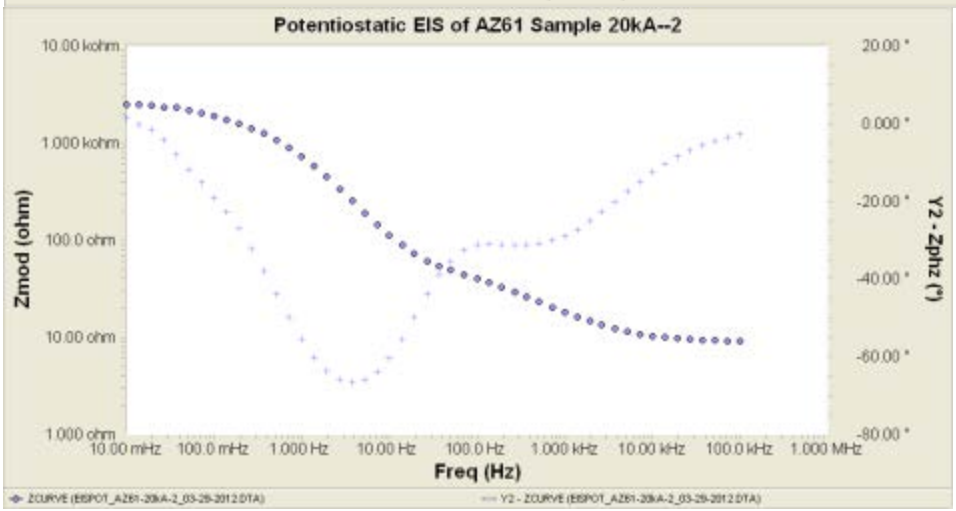
Potentiostatic EIS of AZ61 Sample 20kA--2
Zmod (ohm)
10.00 kohm
1.000 kohm
100.0 ohm
10.00 ohm
1.000 ohm
Y2 - Zphz (°)
20.00 °
0.000 °
-20.00 °
-40.00 °
-60.00 °
-80.00 °
10.00 mHz
100.0 mHz
1.000 Hz
10.00 Hz
100.0 Hz
1.000 kHz
10.00 kHz
100.0 kHz
1.000 MHz
Freq (Hz)

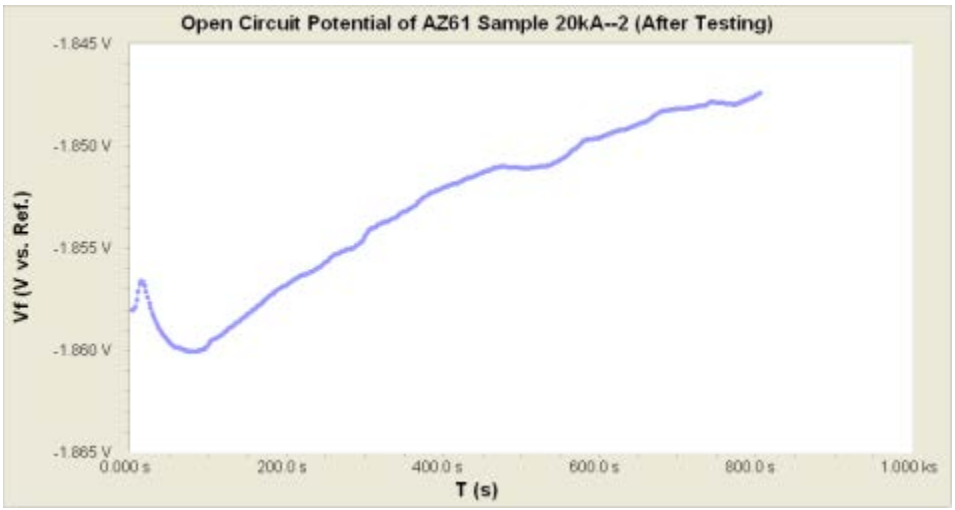
Open Circuit Potential of AZ61 Sample 20kA--2 (After Testing)
-1.845 V
-1.850 V
-1.855 V
-1.860 V
-1.865 V
Vf (V vs. Ref.)
0.000 s
200.0 s
400.0 s
600.0 s
800.0 s
1.000 ks
T (s)

Sample 20-3

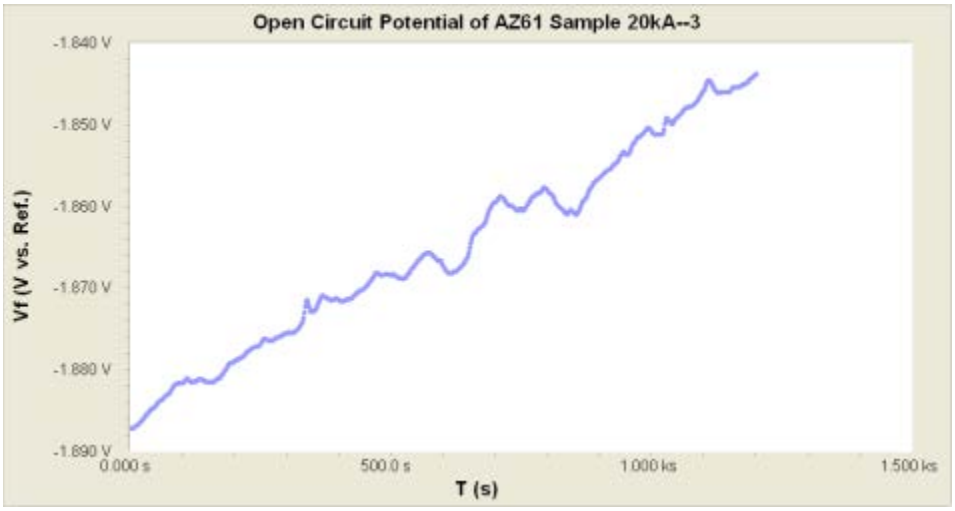
Open Circuit Potential of AZ61 Sample 20kA--3
-1.840 V
-1.850 V
-1.860 V
-1.870 V
-1.880 V
-1.890 V
Vf (V vs. Ref.)
0.000 s
500.0 s
1.000 ks
1.500 ks
T (s)

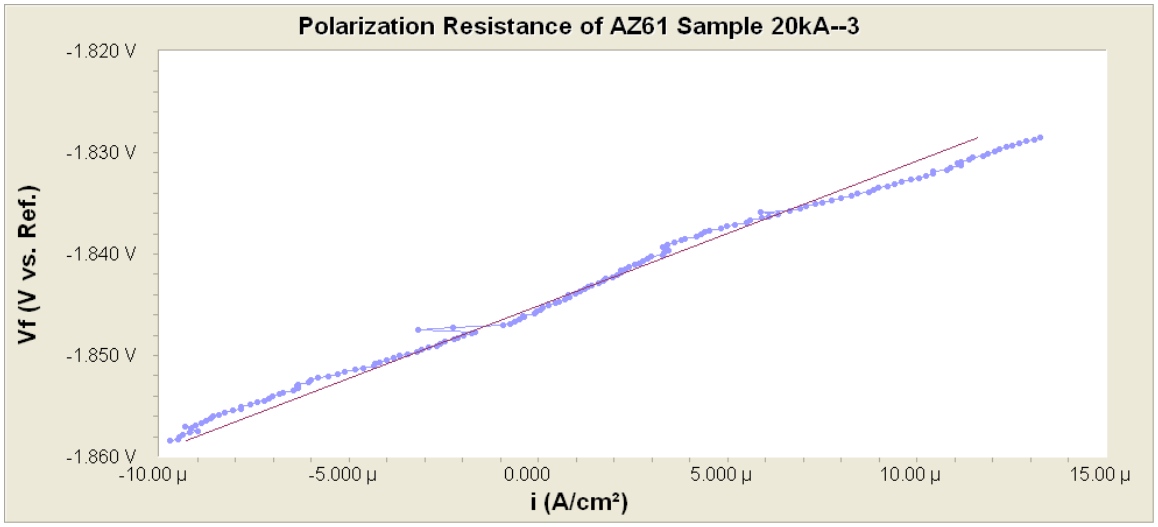
Polarization Resistance of AZ61 Sample 20kA--3
-1.820 V
-1.830 V
-1.840 V
-1.850 V
-1.860 V
Vf (V vs. Ref.)
-10.00 µ
-5.000 µ
0.000
5.000 µ
10.00 µ
15.00 µ
i (A/cm²)

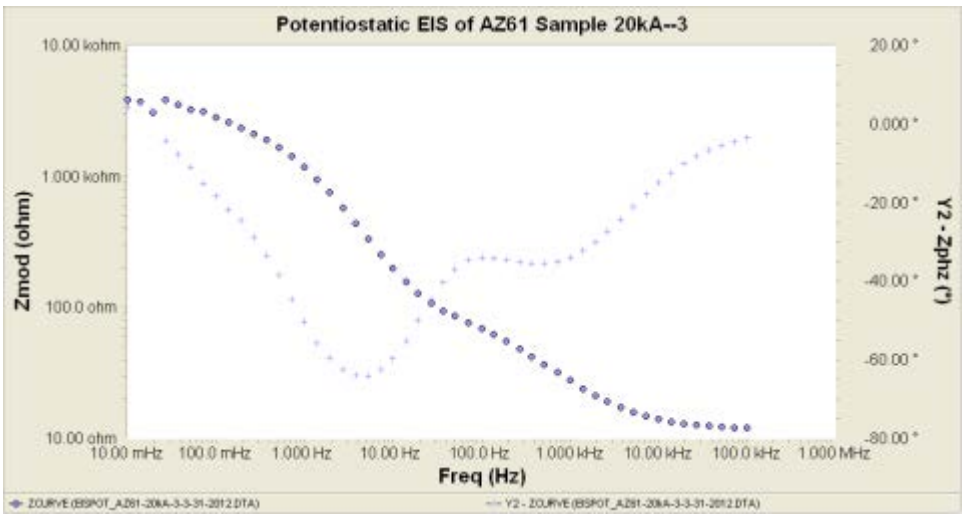
Potentiostatic EIS of AZ61 Sample 20kA--3
10.00 kohm
1.000 kohm
100.0 ohm
10.00 ohm
Zmod (ohm)
20.00 °
0.000 °
-20.00 °
-40.00 °
-60.00 °
-80.00 °
Y2 - Zphz (°)
10.00 mHz
100.0 mHz
1.000 Hz
10.00 Hz
100.0 Hz
1.000 kHz
10.00 kHz
100.0 kHz
1.000 MHz
Freq (Hz)

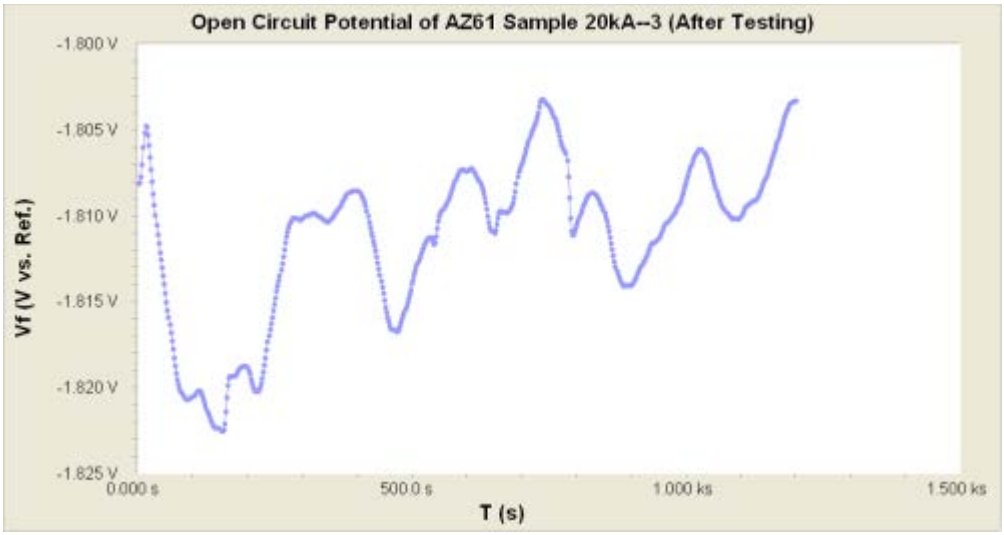
Open Circuit Potential of AZ61 Sample 20kA--3 (After Testing)
-1.800 V
-1.805 V
-1.810 V
-1.815 V
-1.820 V
-1.825 V
Vf (V vs. Ref.)
0.000 s
500.0 s
1.000 ks
1.500 ks
T (s)

Overlays of Graphs for Polarization Resistance

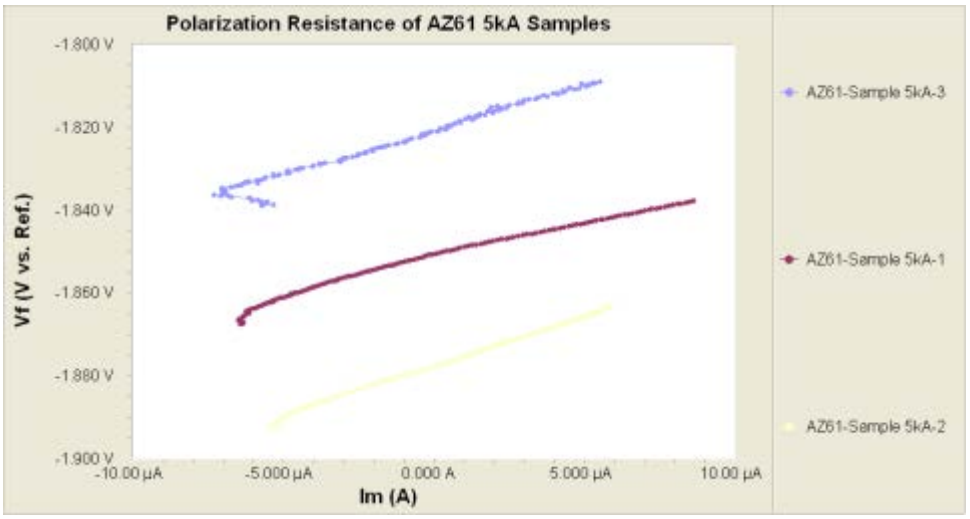

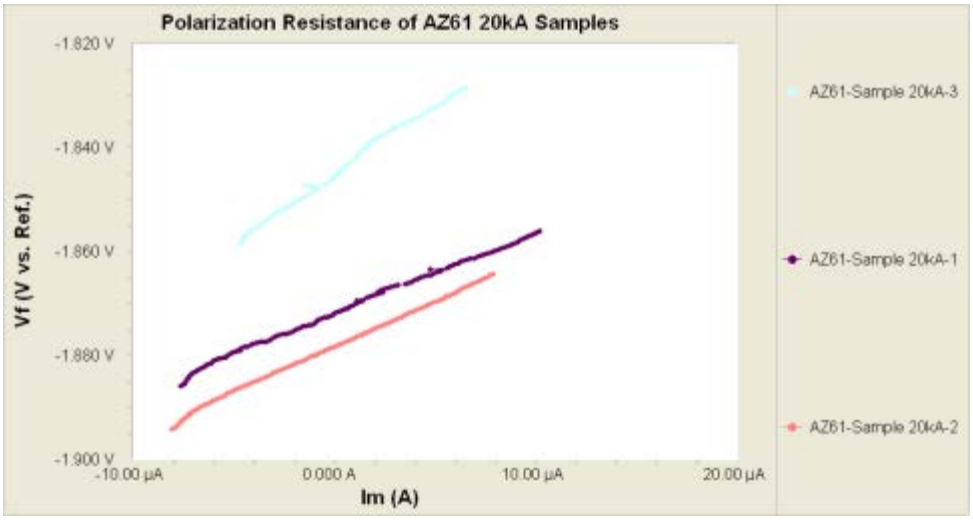

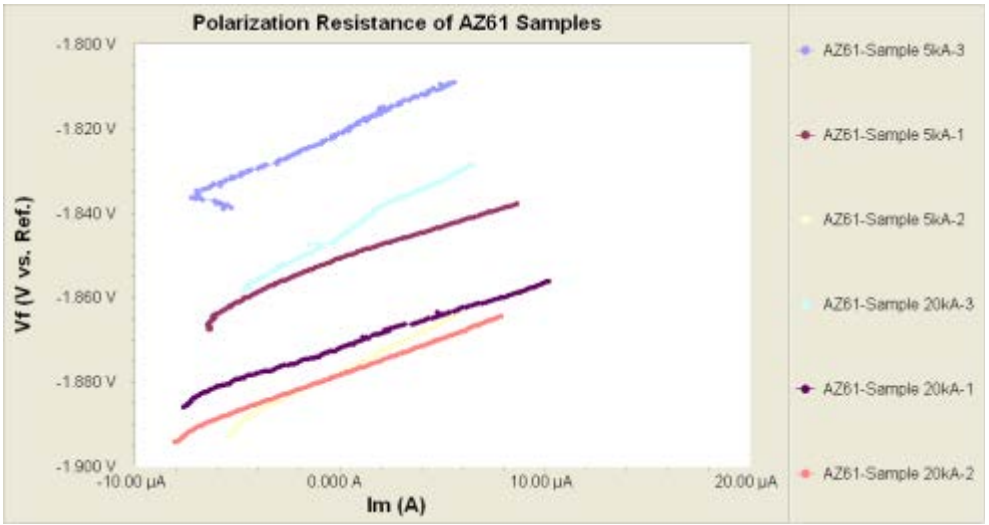

Overlays of Graphs for EIS

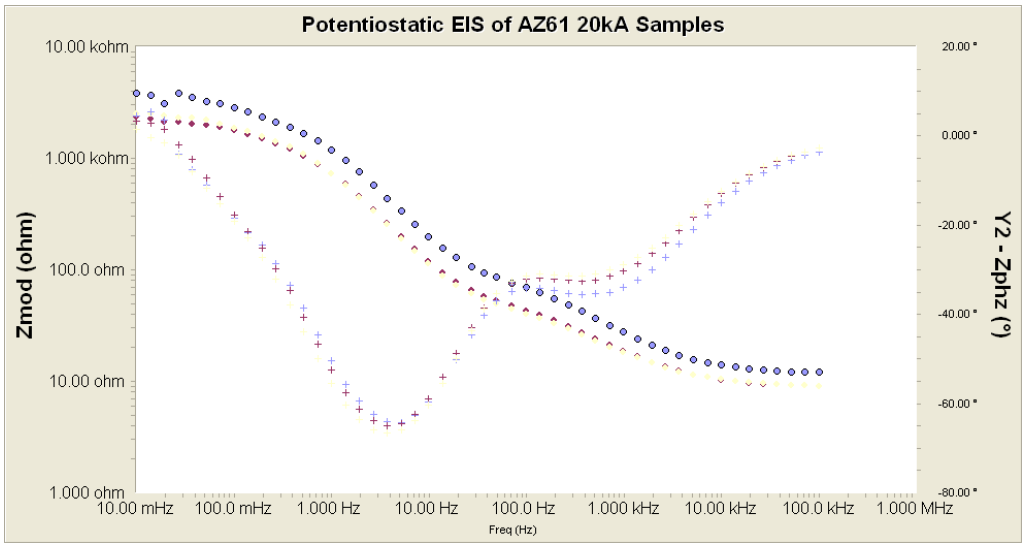

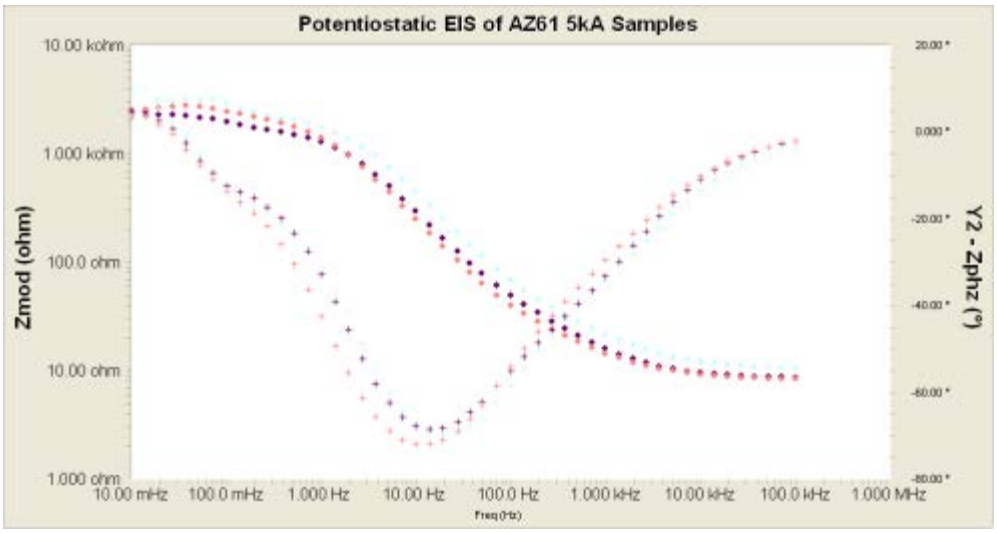

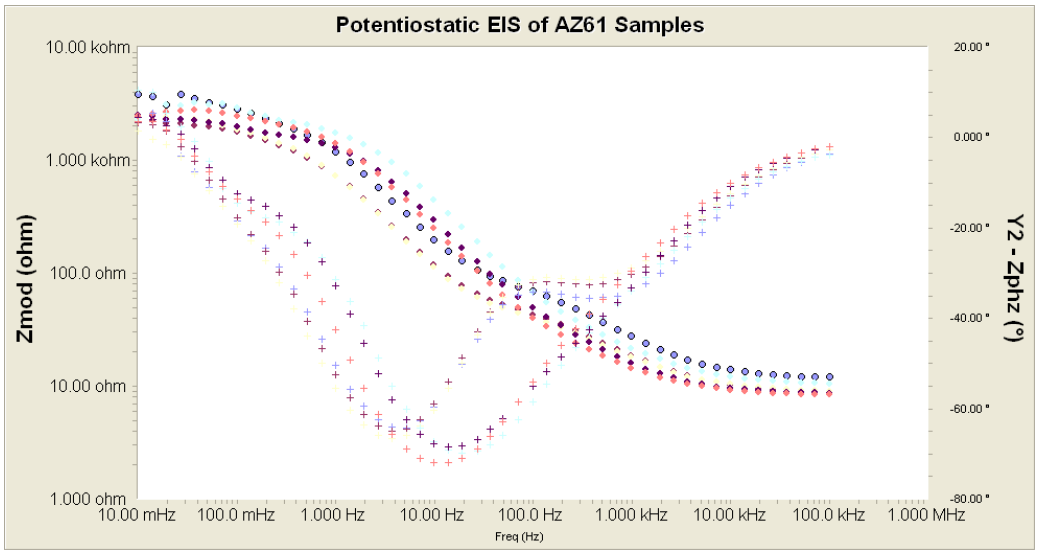
Potentiostatic EIS of AZ61 Samples
10.00 kohm
1.000 kohm
100.0 ohm
10.00 ohm
1.000 ohm
Zmod (ohm)
20.00 °
0.000 °
-20.00 °
-40.00 °
-60.00 °
-80.00 °
Y2 - Zphz (°)
10.00 mHz
100.0 mHz
1.000 Hz
10.00 Hz
100.0 Hz
1.000 kHz
10.00 kHz
100.0 kHz
1.000 MHz
Freq (Hz)

Appendix B: Comparison of Corrosion Rates

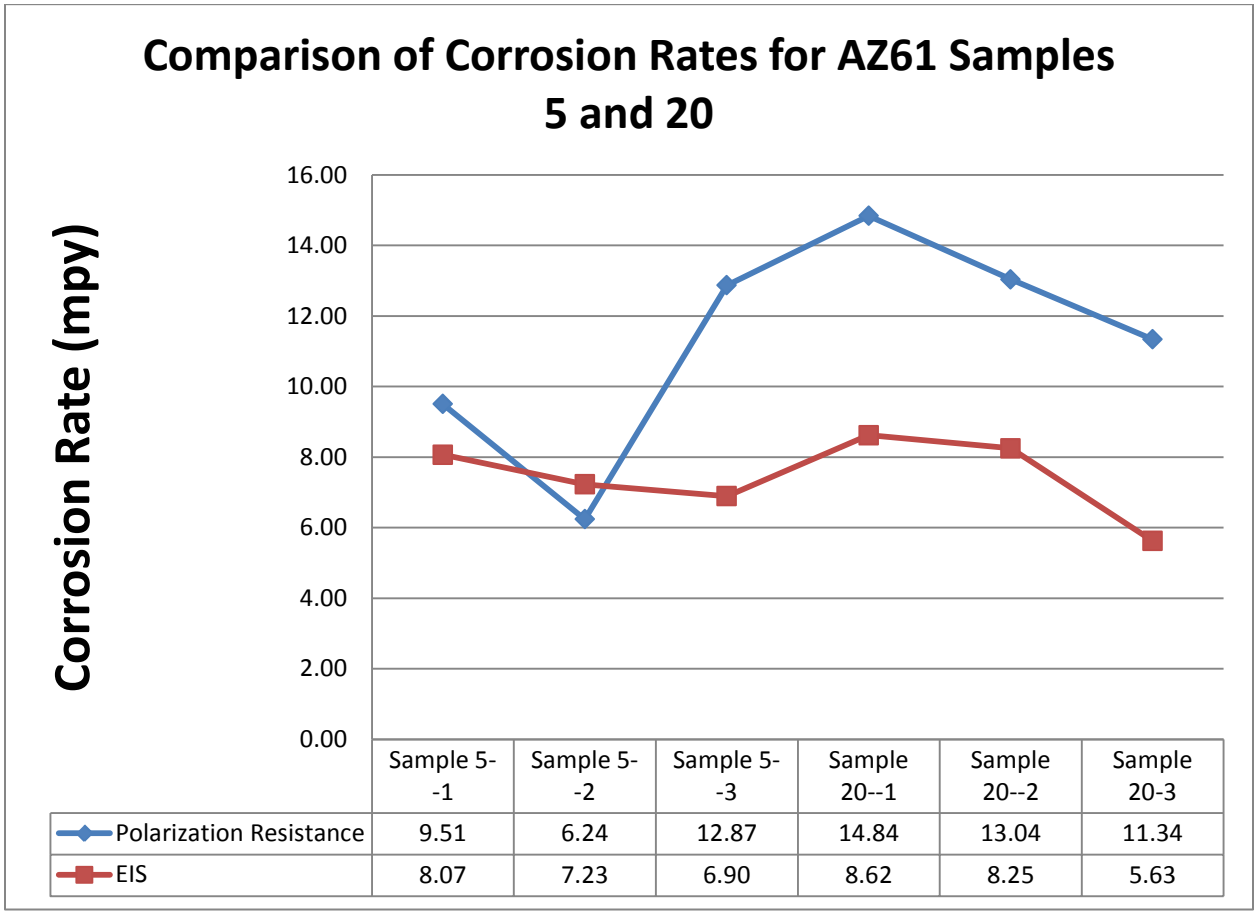

	Sample 5--1	Sample 5--2	Sample 5--3	Sample 20--1	Sample 20--2	Sample 20-3
Polarization Resistance	9.51	6.24	12.87	14.84	13.04	11.34
EIS	8.07	7.23	6.90	8.62	8.25	5.63

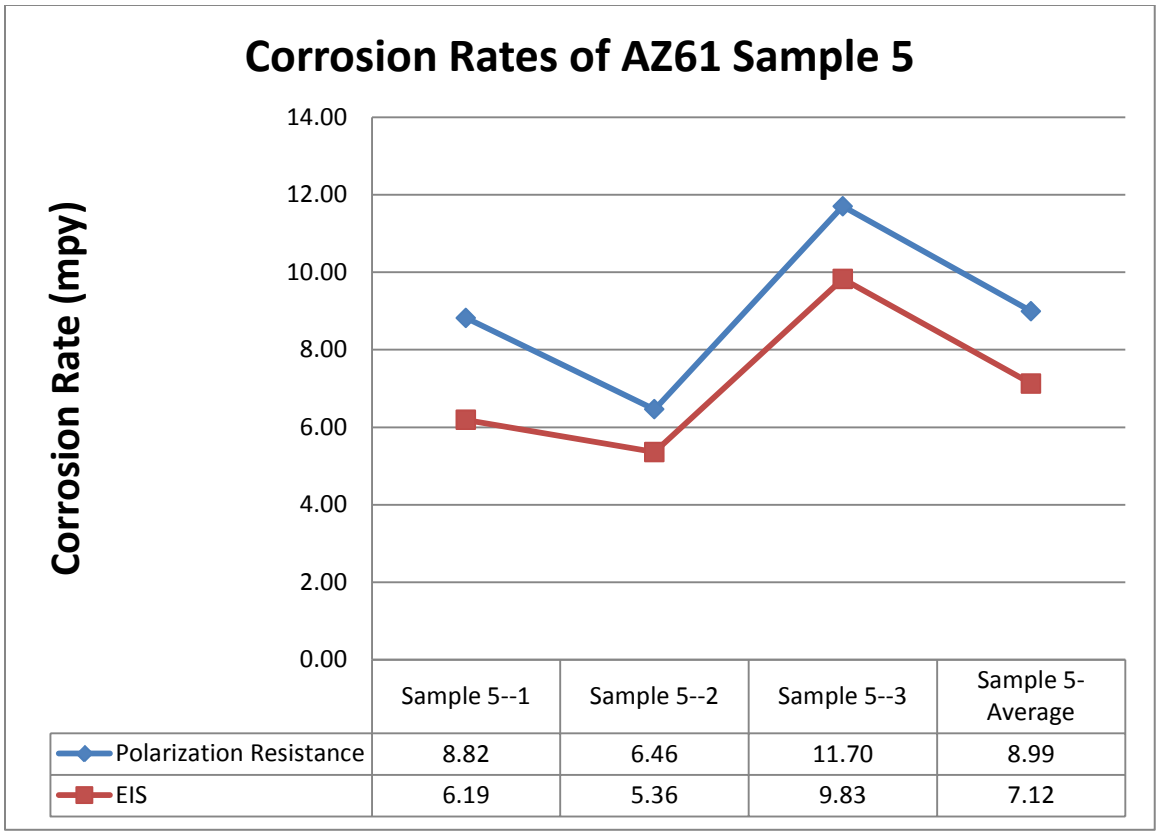
Corrosion Rates of AZ61 Sample 5
Corrosion Rate (mpy)
14.00
12.00
10.00
8.00
6.00
4.00
2.00
0.00
Sample 5--1
Sample 5--2
Sample 5--3
Sample 5-Average
Polarization Resistance
8.82
6.46
11.70
8.99
EIS
6.19
5.36
9.83
7.12

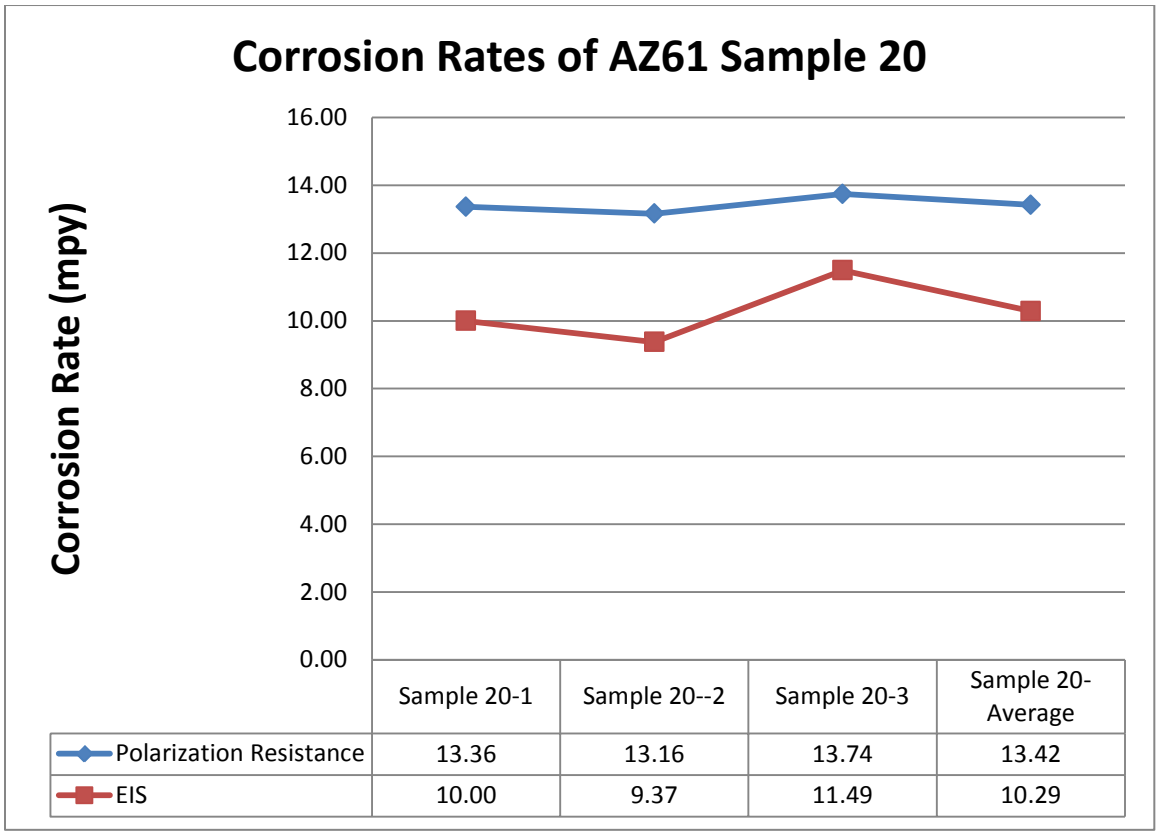
Corrosion Rates of AZ61 Sample 20
Corrosion Rate (mpy)
16.00
14.00
12.00
10.00
8.00
6.00
4.00
2.00
0.00
Sample 20-1
Sample 20--2
Sample 20-3
Sample 20-Average
Polarization Resistance
13.36
13.16
13.74
13.42
EIS
10.00
9.37
11.49
10.29

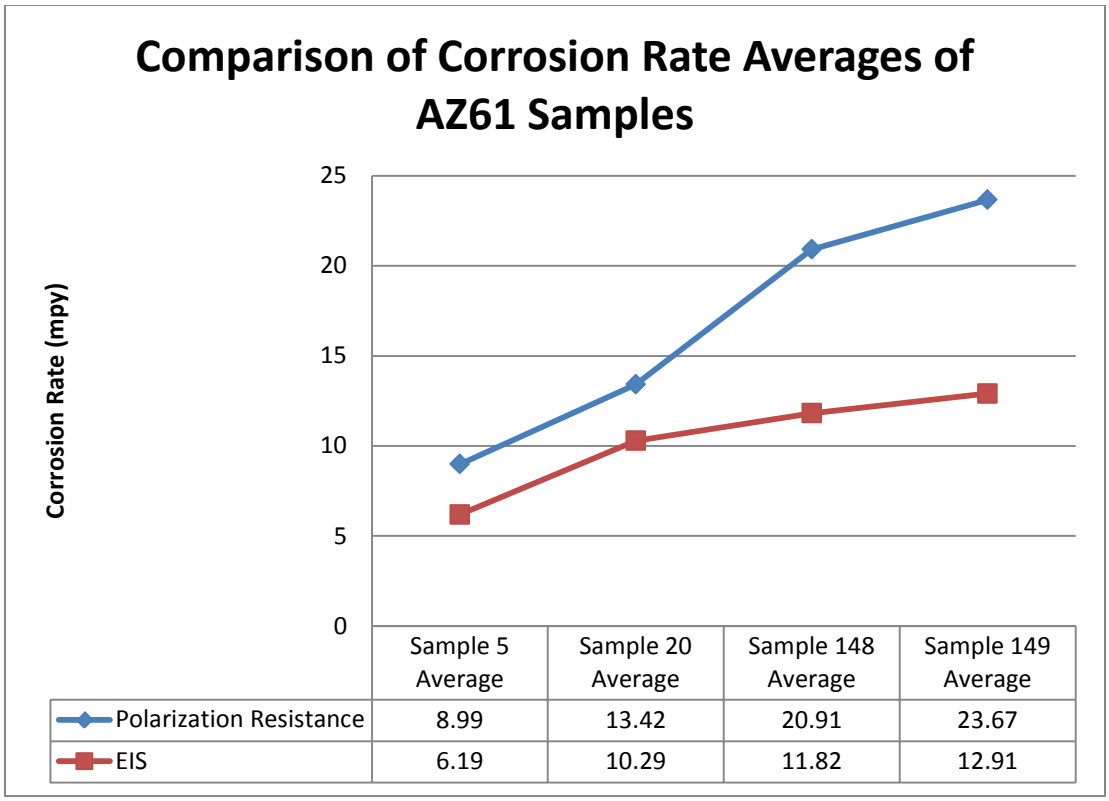
Comparison of Corrosion Rate Averages of AZ61 Samples
Corrosion Rate (mpy)
25
20
15
10
5
0
Sample 5 Average
Sample 20 Average
Sample 148 Average
Sample 149 Average
Polarization Resistance
8.99
13.42
20.91
23.67
EIS
6.19
10.29
11.82
12.91

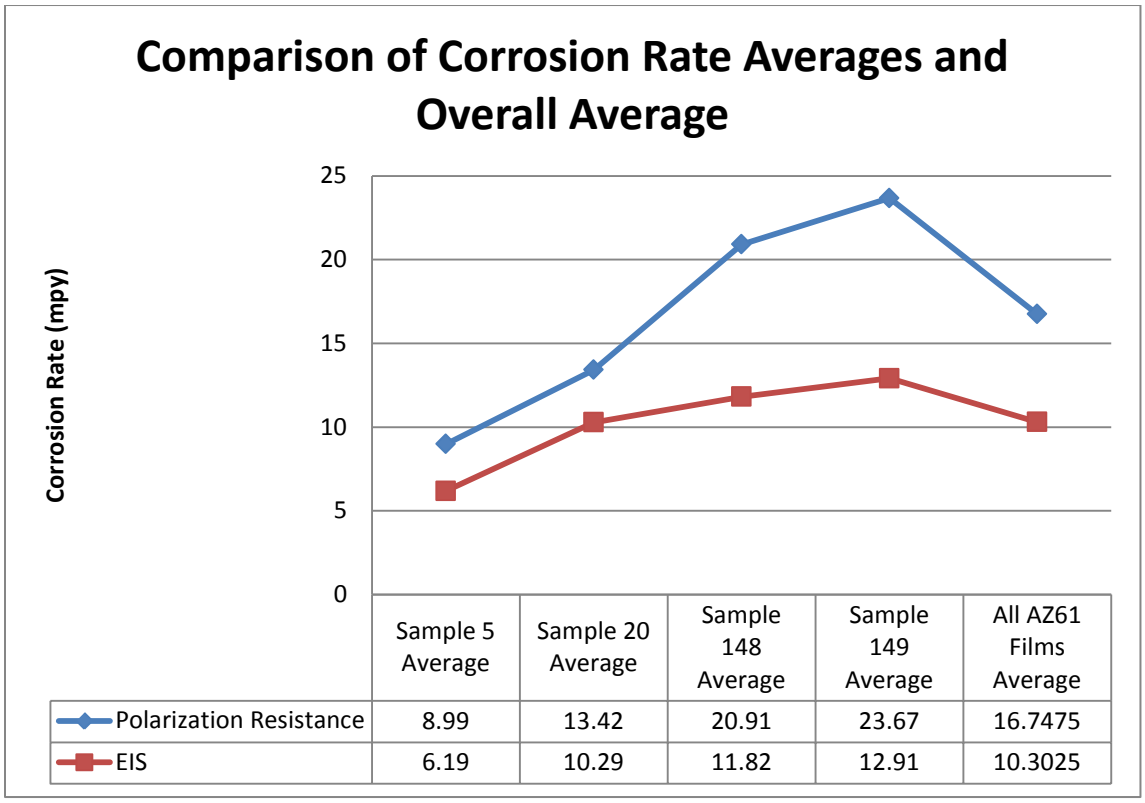
Comparison of Corrosion Rate Averages and Overall Average
Corrosion Rate (mpy)
25
20
15
10
5
0
Sample 5 Average
Sample 20 Average
Sample 148 Average
Sample 149 Average
All AZ61 Films Average
Polarization Resistance
8.99
13.42
20.91
23.67
16.7475
EIS
6.19
10.29
11.82
12.91
10.3025

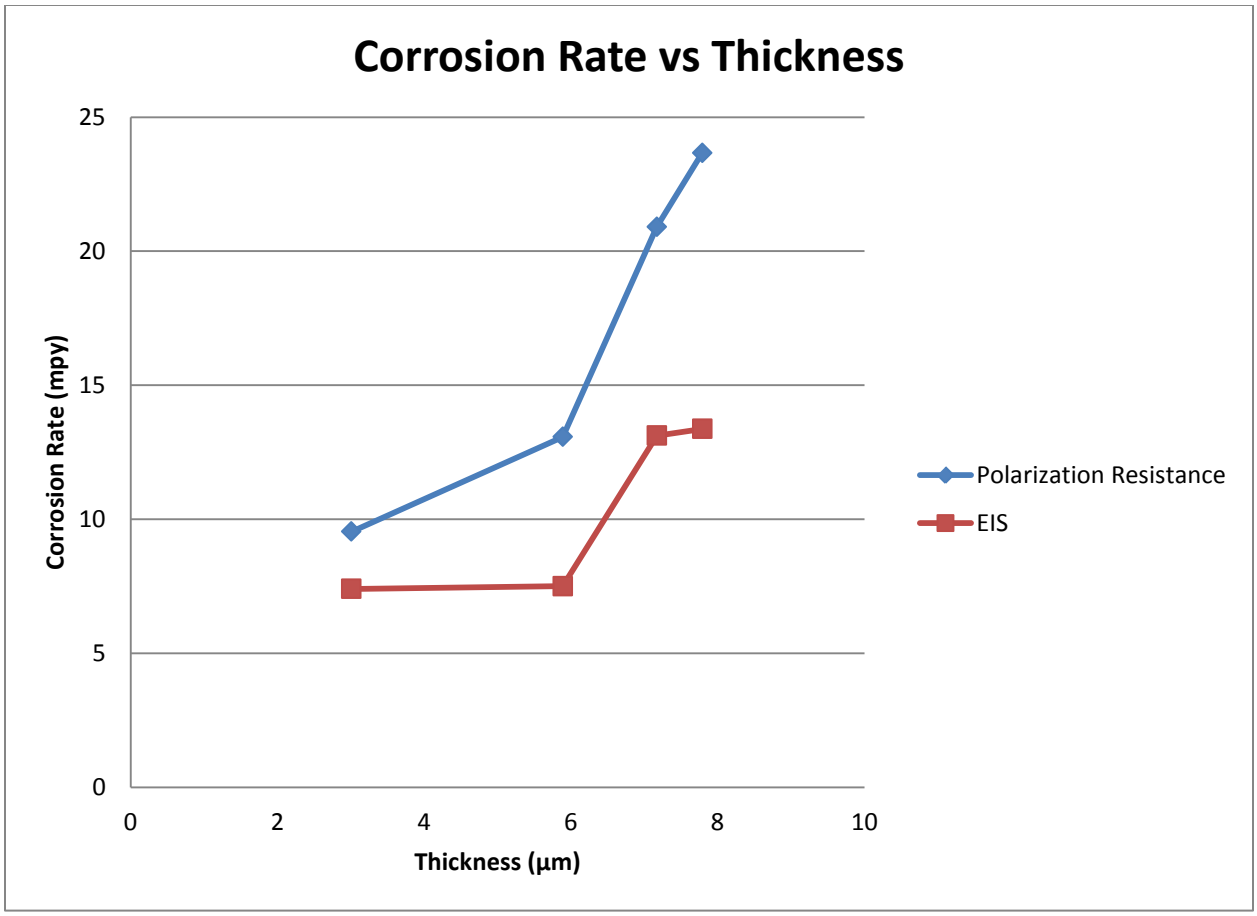
Corrosion Rate vs Thickness
Corrosion Rate (mpy)
25
20
15
10
5
0
0
2
4
6
8
10
Thickness (µm)
Polarization Resistance
EIS

Appendix C: SEM Images

Sample 5

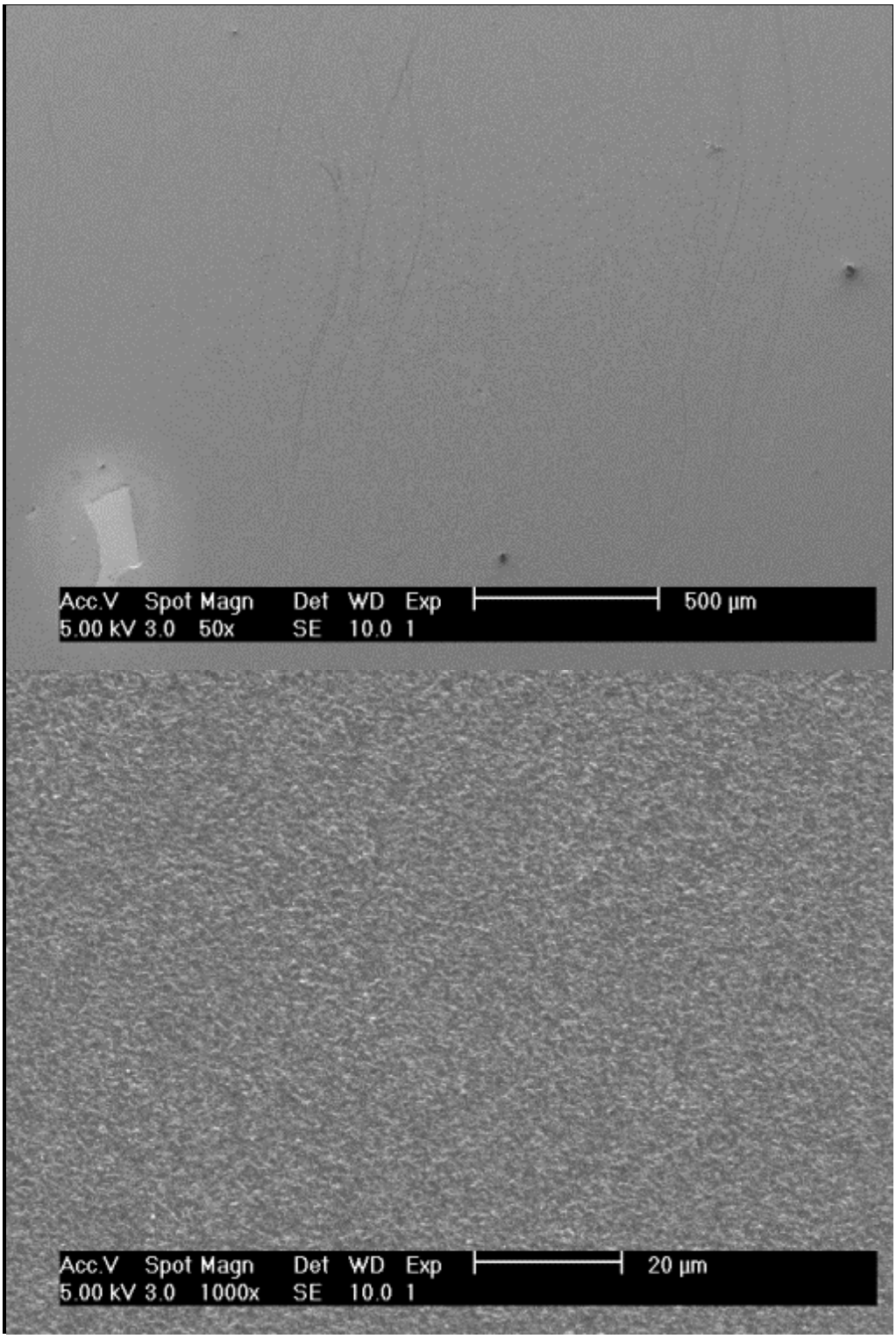

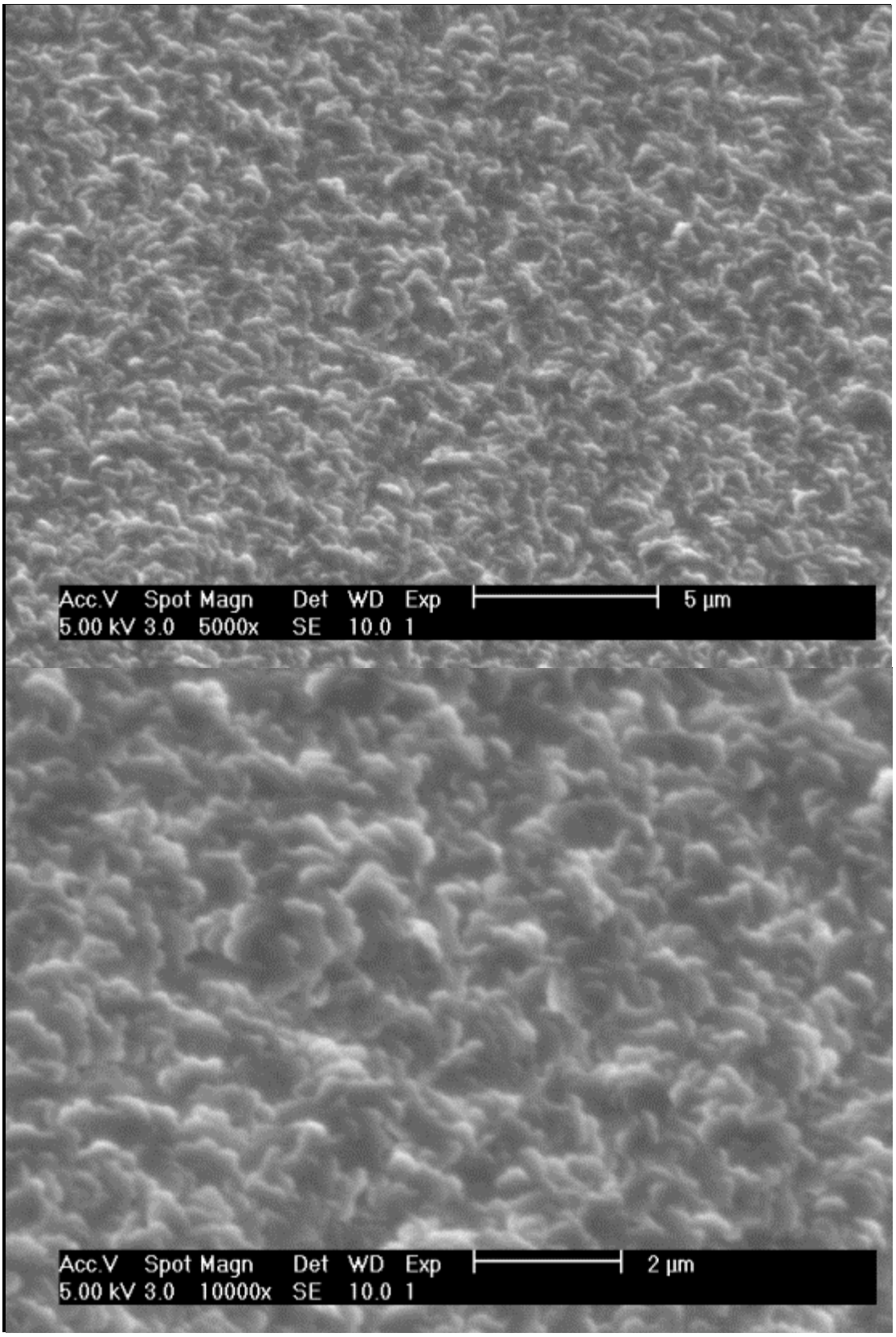
Acc.V Spot Magn Det WD Exp
5.00 kV 3.0 5000x SE 10.0 1
5 µm
Acc.V Spot Magn Det WD Exp
5.00 kV 3.0 10000x SE 10.0 1
2 µm

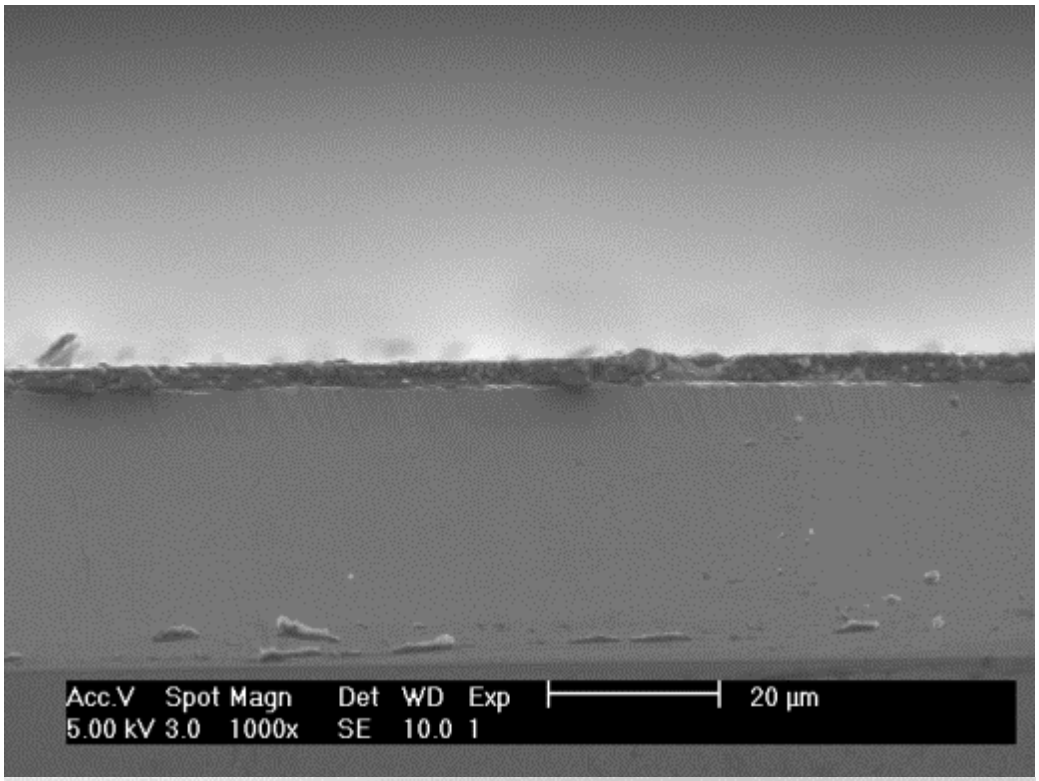
Acc.V Spot Magn Det WD Exp
5.00 kV 3.0 1000x SE 10.0 1
20 µm

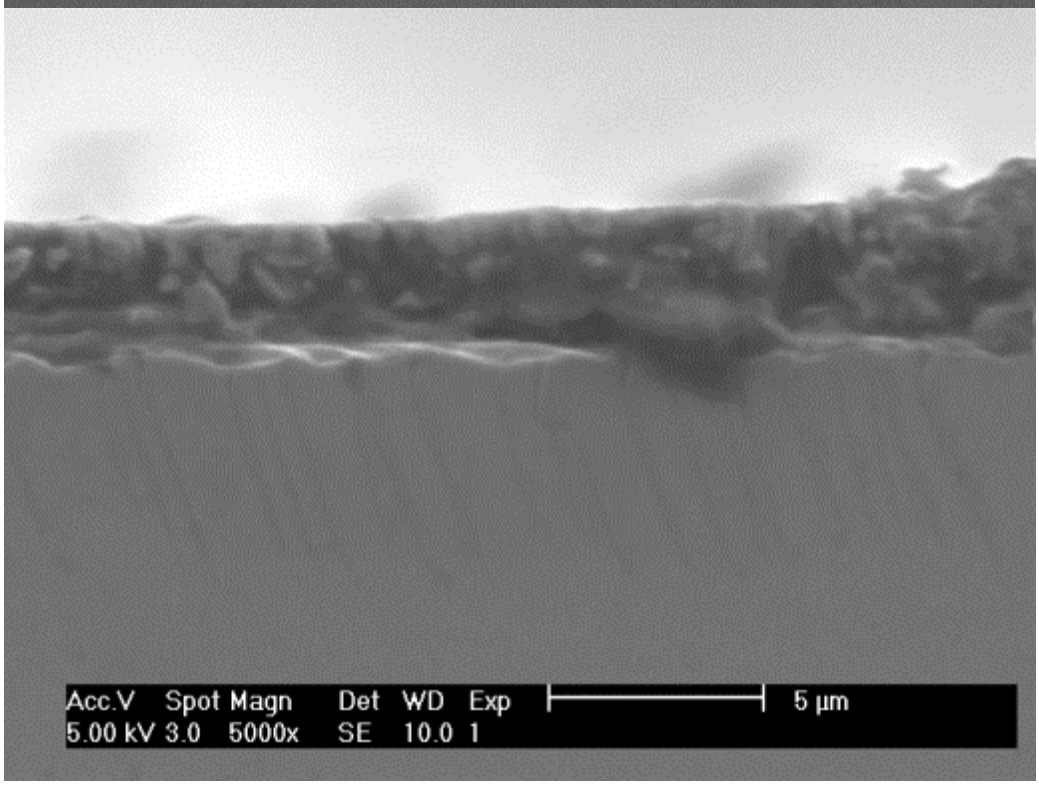
Acc.V Spot Magn Det WD Exp
5.00 kV 3.0 5000x SE 10.0 1
5 µm

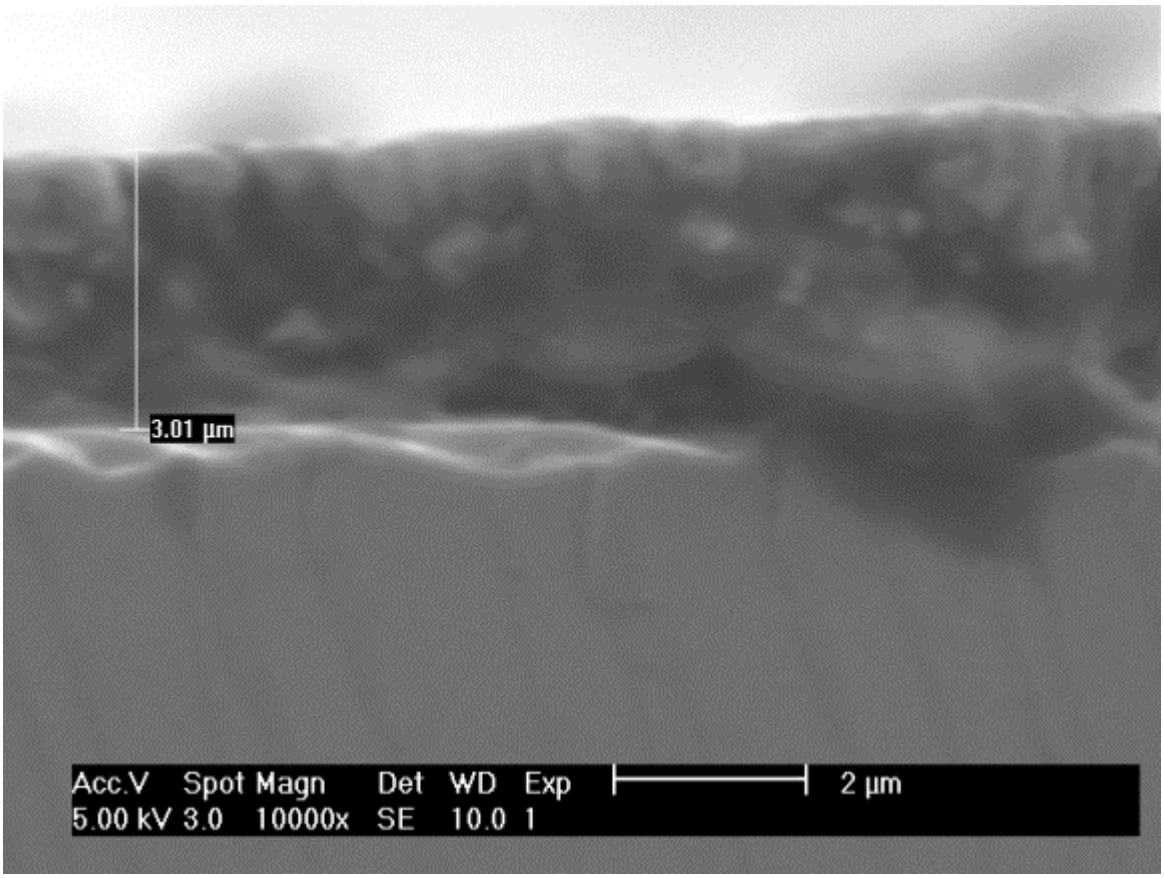
3.01 µm
Acc.V Spot Magn Det WD Exp
5.00 kV 3.0 10000x SE 10.0 1
2 µm

Sample 20

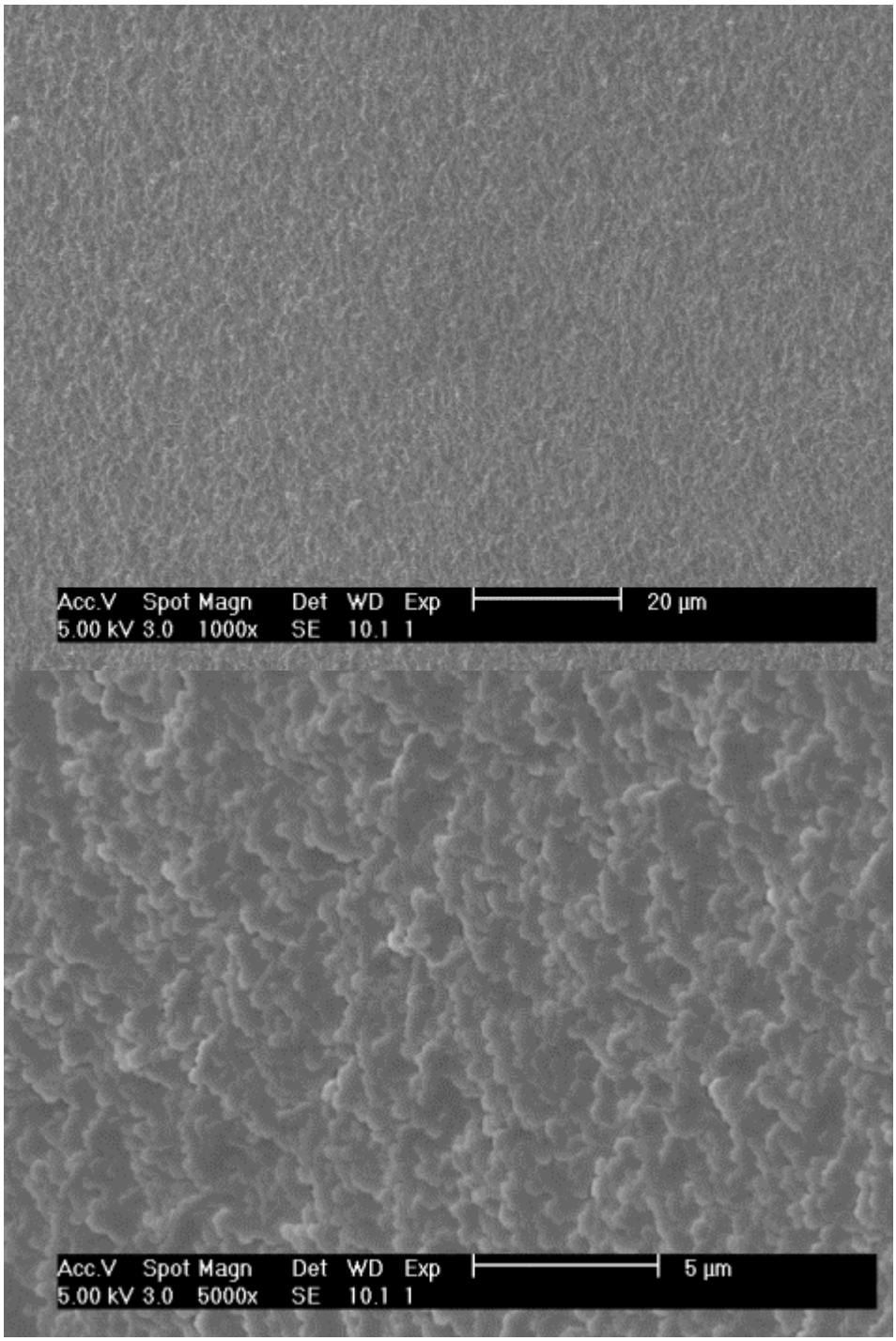
Acc.V Spot Magn Det WD Exp 20 µm
5.00 kV 3.0 1000x SE 10.1 1
Acc.V Spot Magn Det WD Exp 5 µm
5.00 kV 3.0 5000x SE 10.1 1

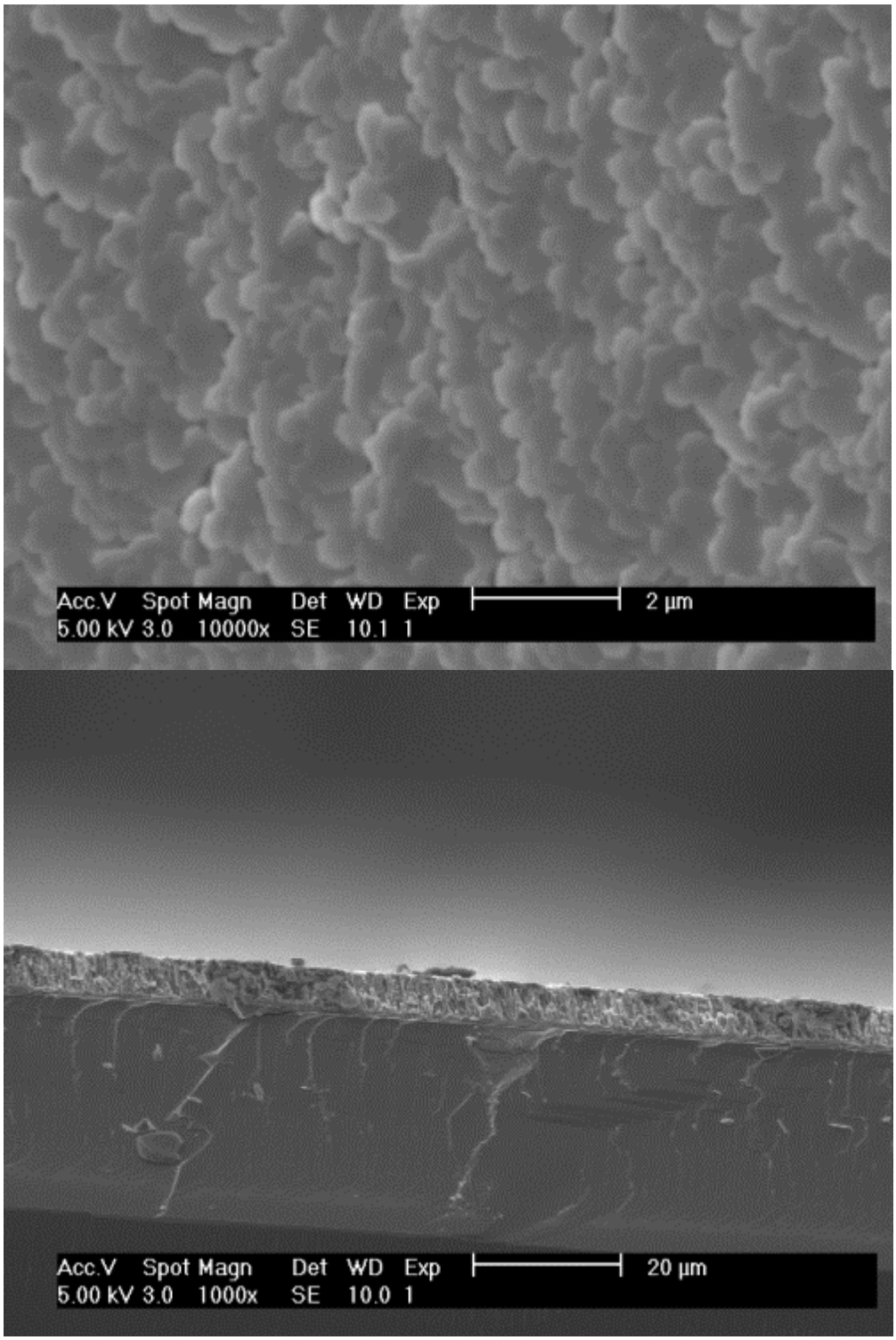
Acc.V Spot Magn Det WD Exp 2 µm
5.00 kV 3.0 10000x SE 10.1 1
Acc.V Spot Magn Det WD Exp 20 µm
5.00 kV 3.0 1000x SE 10.0 1

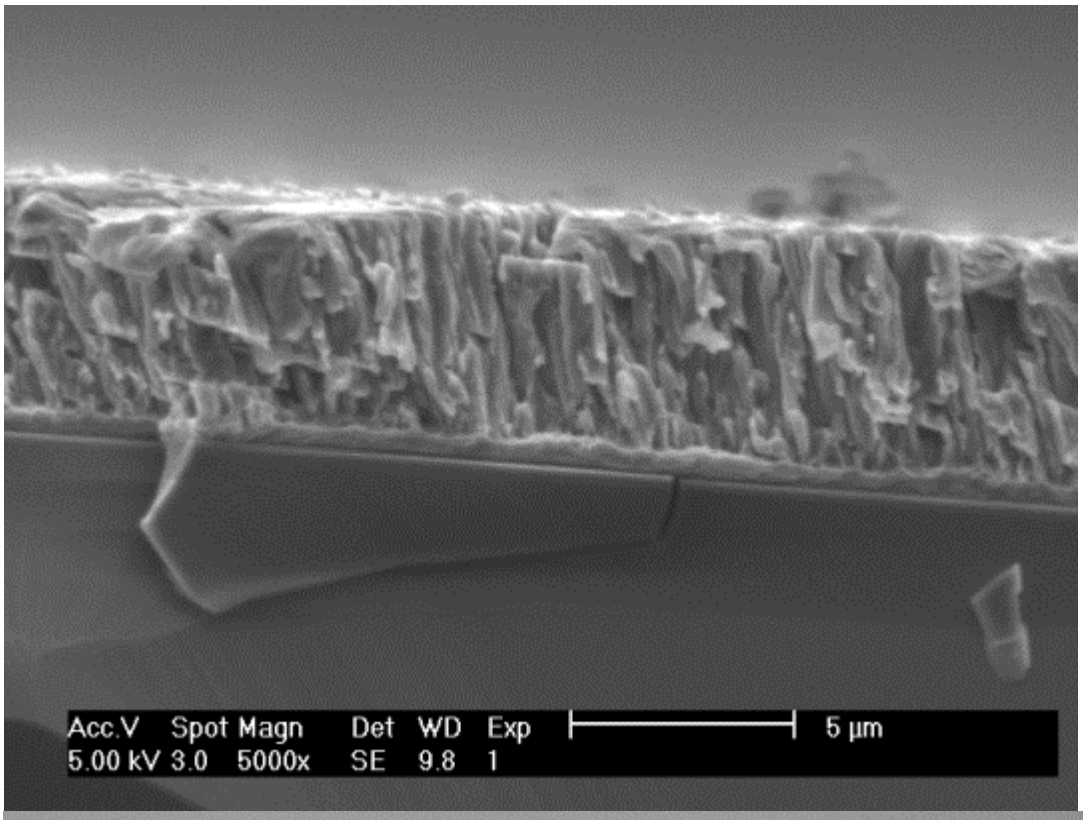
Acc.V Spot Magn Det WD Exp 5 µm
5.00 kV 3.0 5000x SE 9.8 1

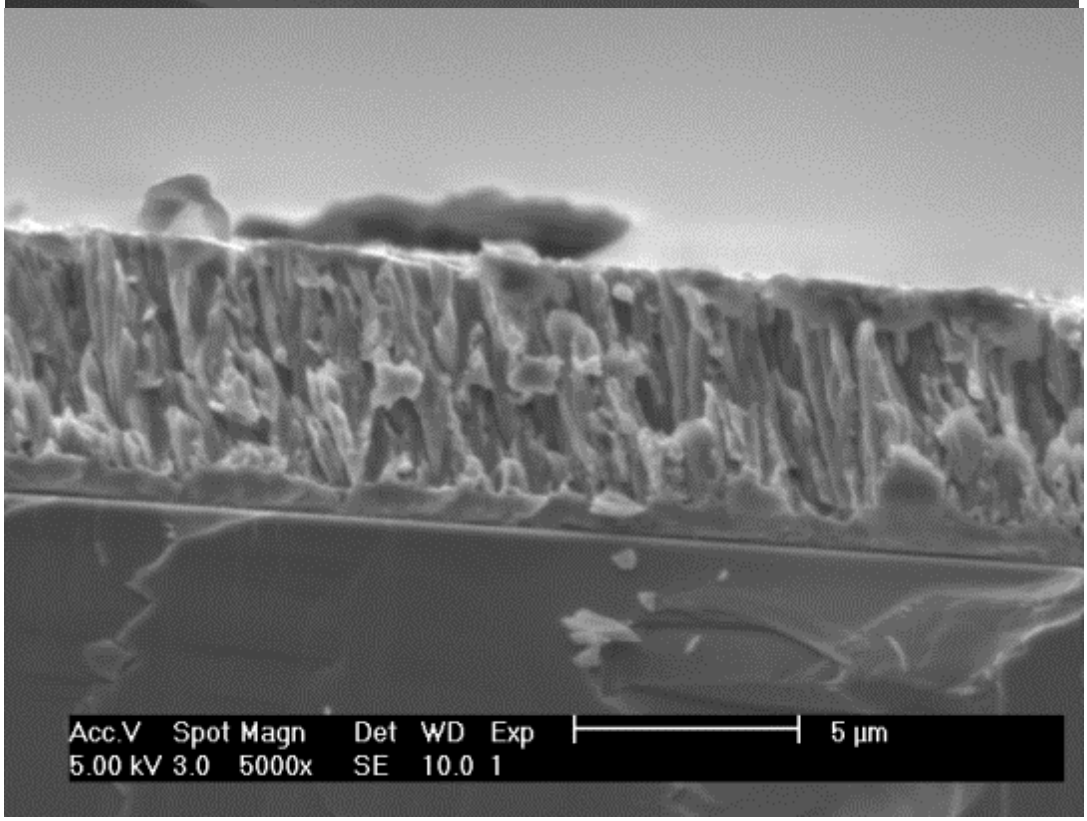
Acc.V Spot Magn Det WD Exp 5 µm
5.00 kV 3.0 5000x SE 10.0 1

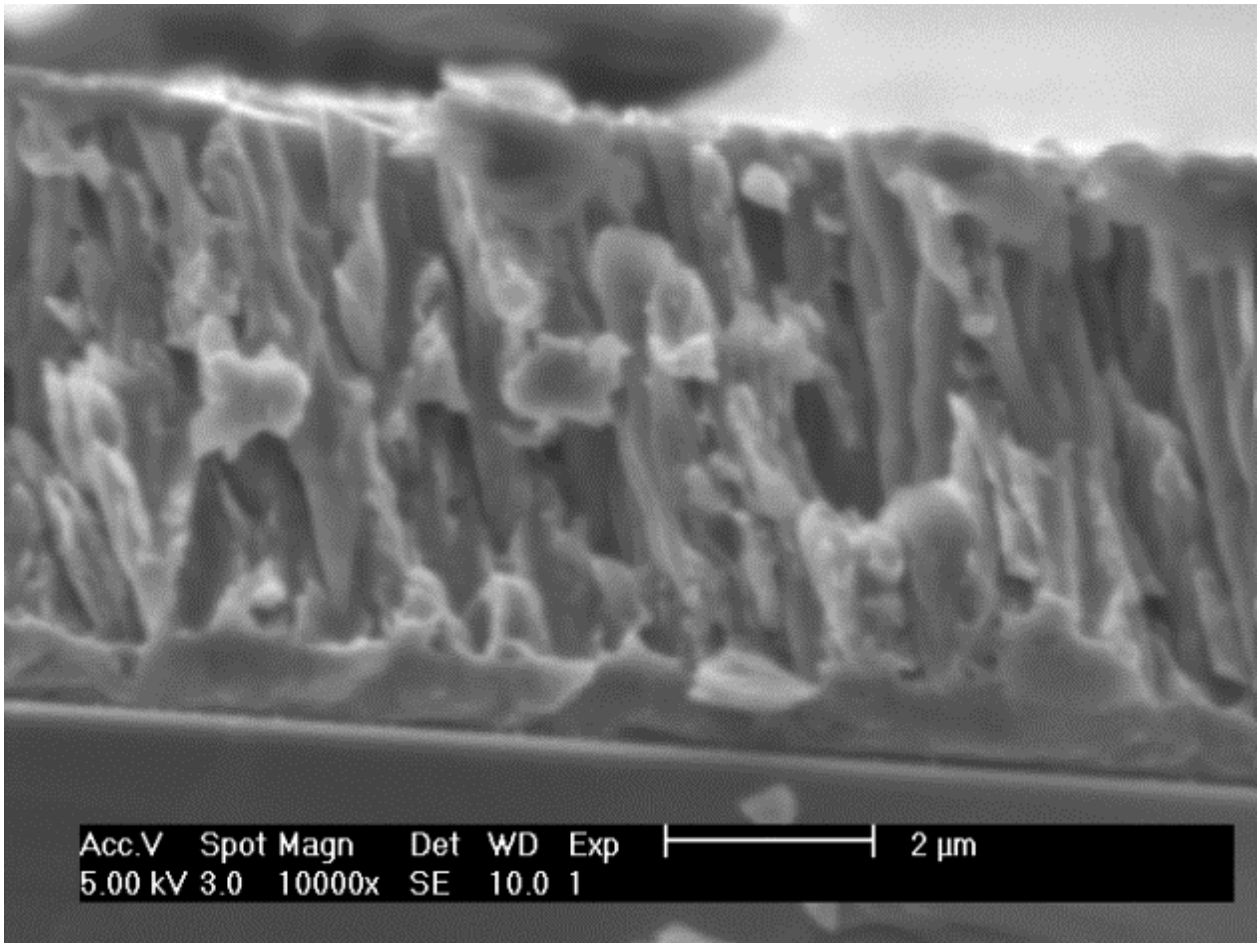
Acc.V Spot Magn Det WD Exp
5.00 kV 3.0 10000x SE 10.0 1
2 µm

Sample 148

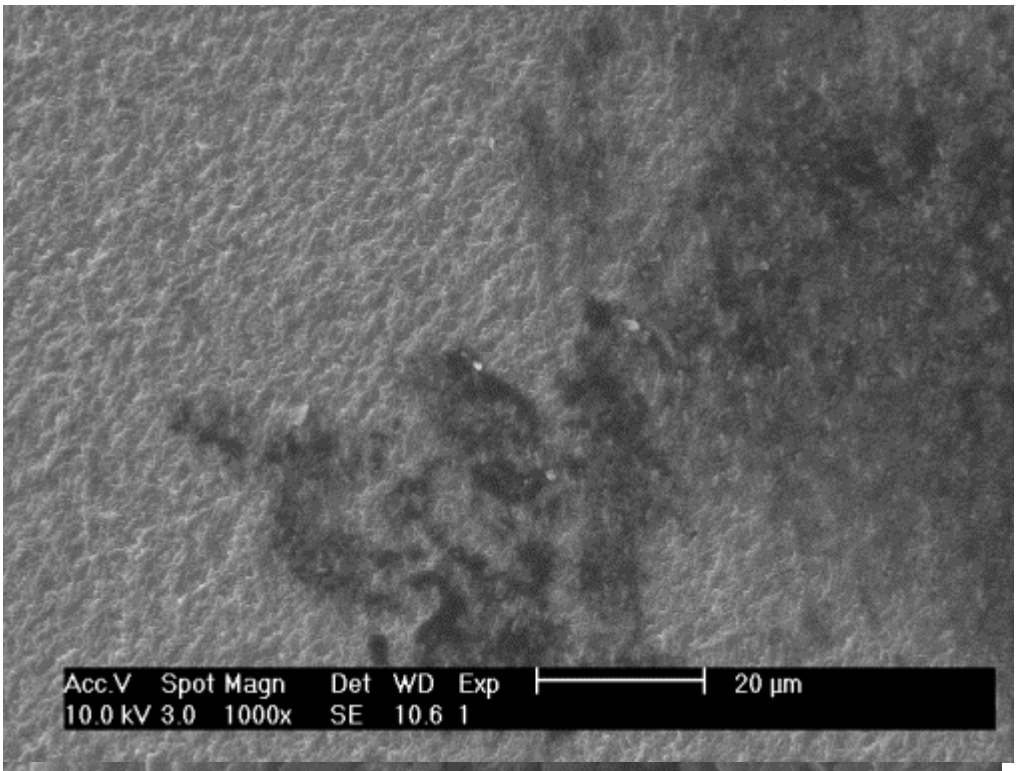
Acc.V Spot Magn Det WD Exp 20 µm
10.0 kV 3.0 1000x SE 10.6 1

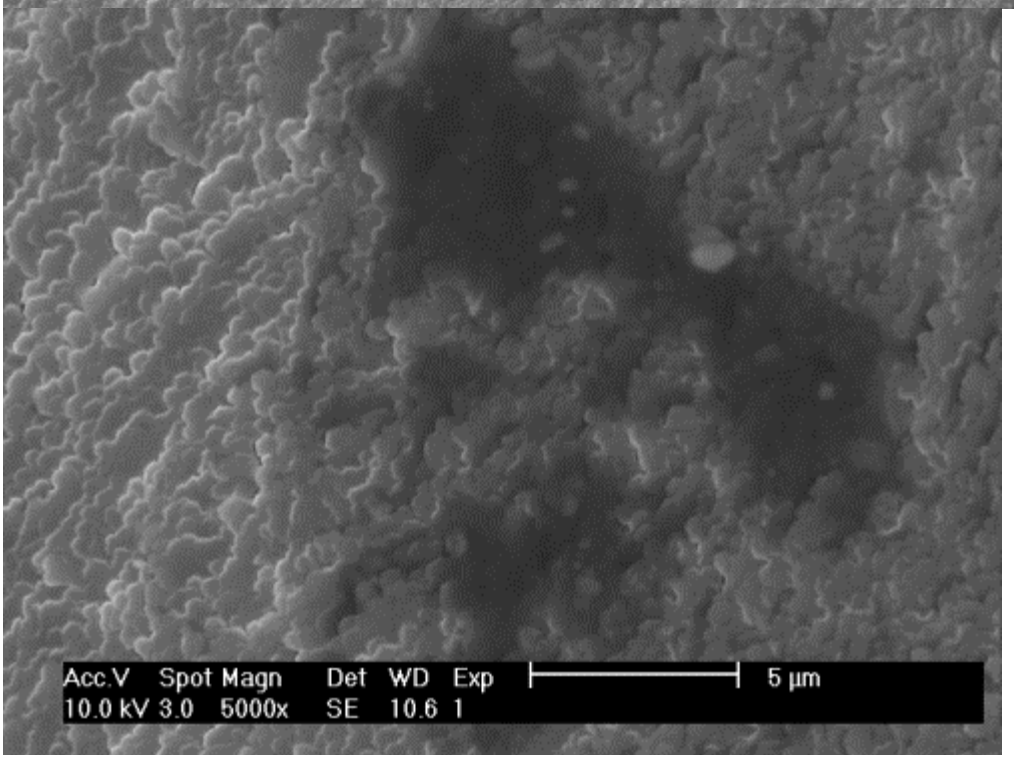
Acc.V Spot Magn Det WD Exp 5 µm
10.0 kV 3.0 5000x SE 10.6 1

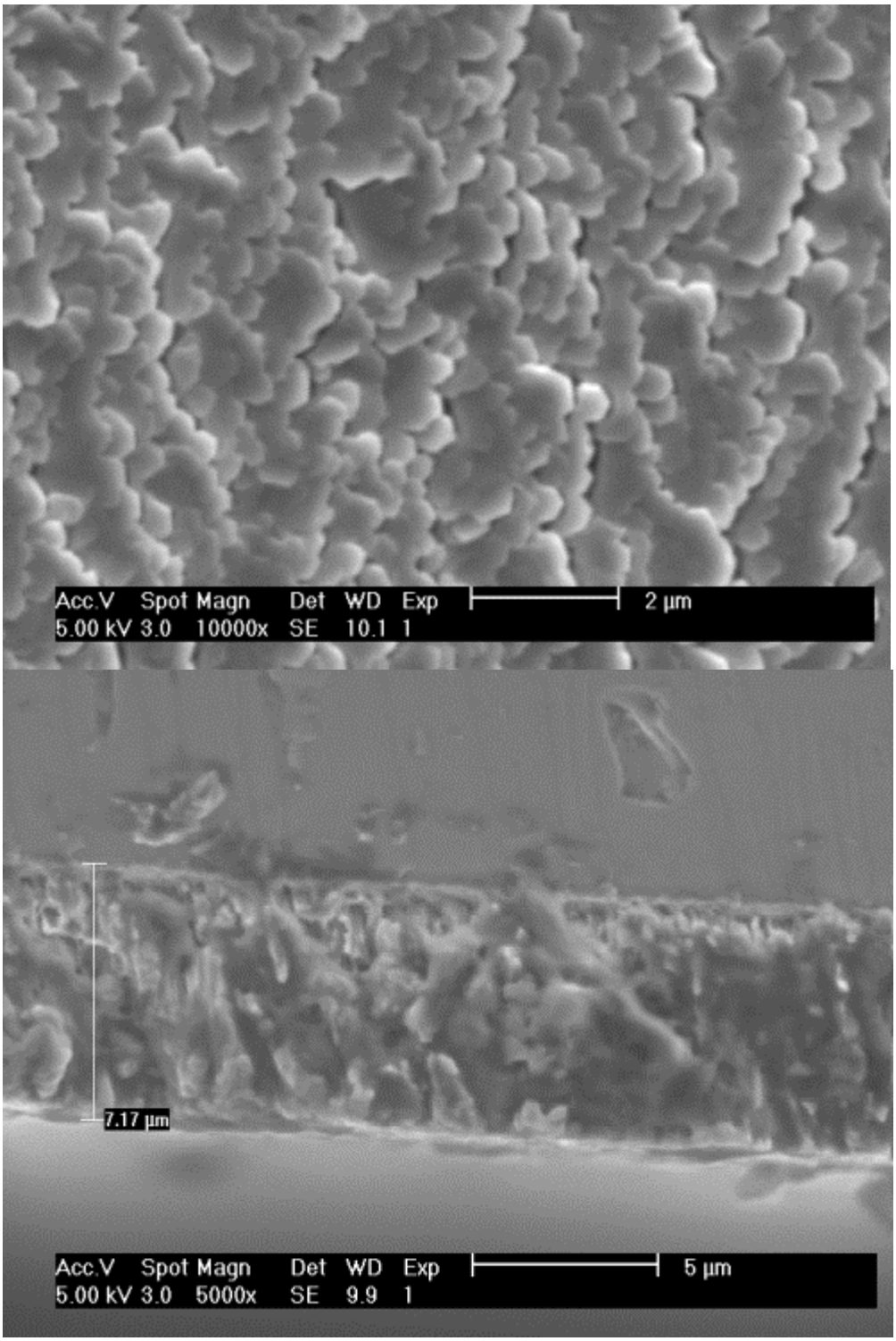
Acc.V Spot Magn Det WD Exp 2 µm
5.00 kV 3.0 10000x SE 10.1 1
7.17 µm
Acc.V Spot Magn Det WD Exp 5 µm
5.00 kV 3.0 5000x SE 9.9 1

Sample 149

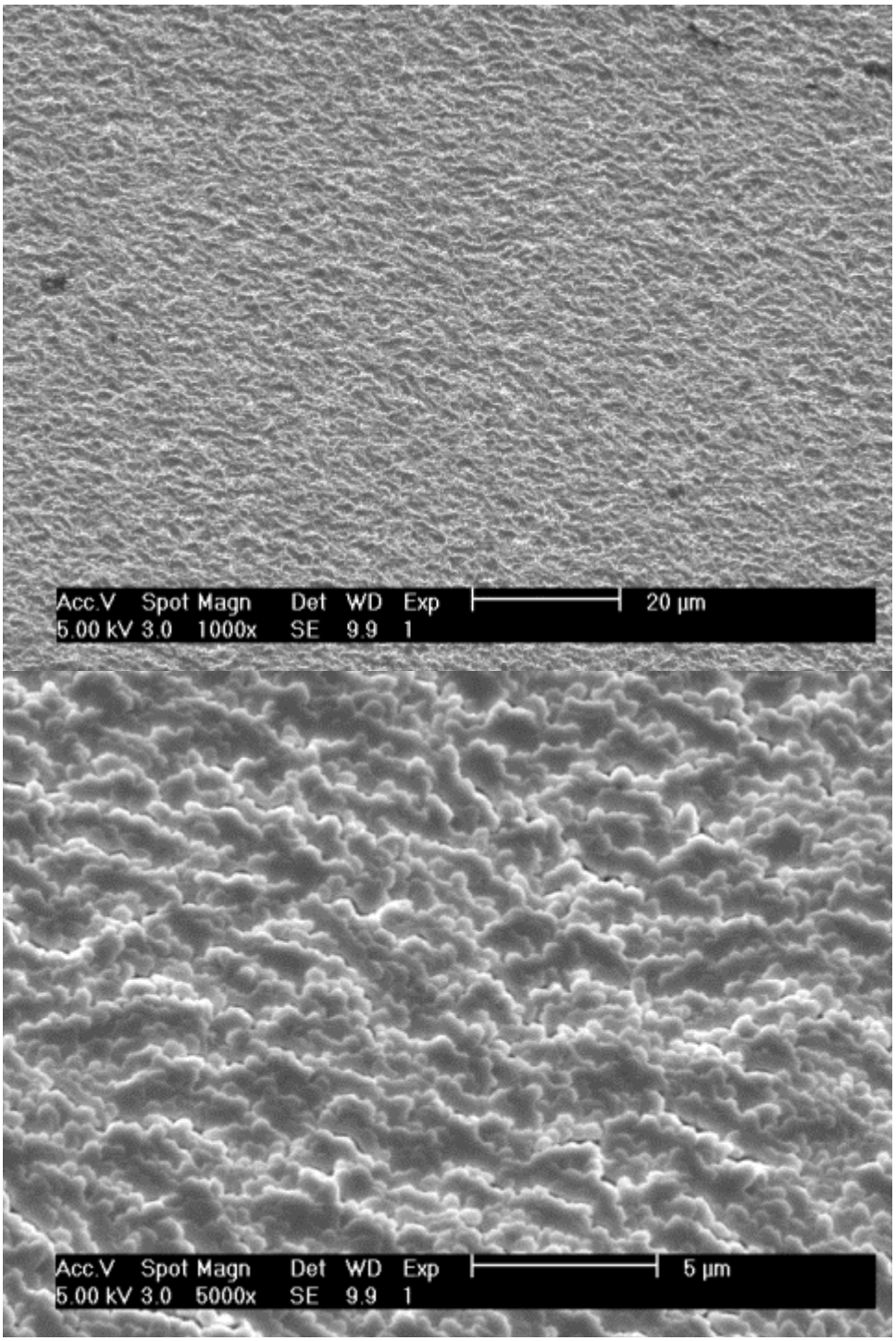
Acc.V Spot Magn Det WD Exp 20 µm
5.00 kV 3.0 1000x SE 9.9 1
Acc.V Spot Magn Det WD Exp 5 µm
5.00 kV 3.0 5000x SE 9.9 1

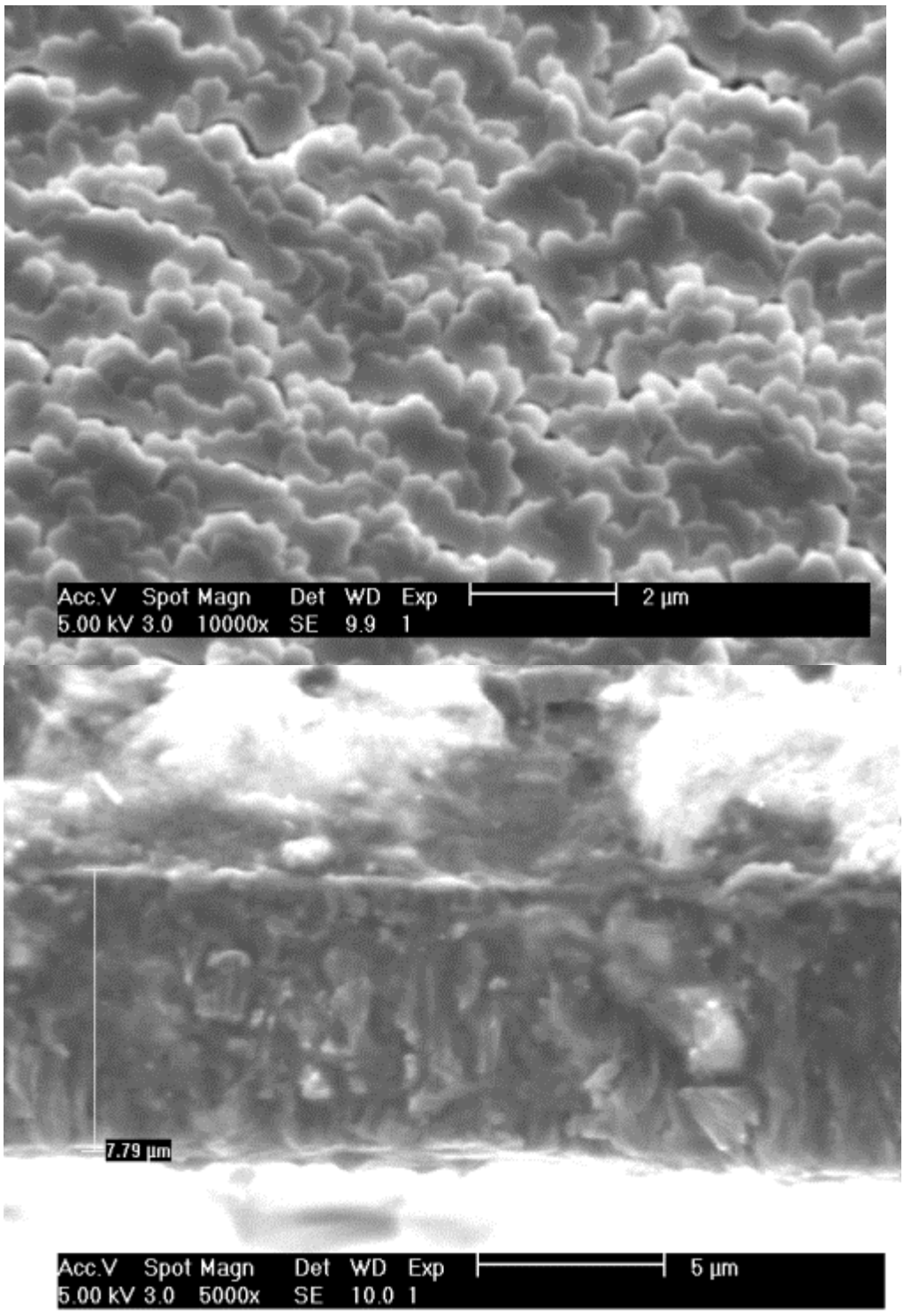
Acc.V Spot Magn Det WD Exp 2 µm
5.00 kV 3.0 10000x SE 9.9 1
7.79 µm
Acc.V Spot Magn Det WD Exp 5 µm
5.00 kV 3.0 5000x SE 10.0 1

References

[1]Baldwin, K. R., Bray, D. J., Howard, G. D., & Gardiner, R. W. (1996). Corrosion behaviour of some vapour deposited Magnesium alloys. *Materials Science and Technology*. 12. 937-943.

[2]T.G. Nieh, J. Wadsworth. (1987). Thick magnesium films produced by deposition techniques. *Thin Solid Films*. 152(3), 525-534. Retrieved from the Science Direct database.

[3]Wolfe, R., & Shaw, B. (2007). The effect of thermal treatment on the corrosion properties of vapor deposited magnesium alloyed with yttrium, aluminum, titanium, and misch metal. *Journal of Alloys and Compounds*, *437*(1-2), 157-164. doi:10.1016/j.jallcom.2006.07.111

[4]Smith, D. L. (1995). *Thin-film deposition, principles and practice*. McGraw-Hill Professional.

[5] *Fabrication techniques*. University of Texas at El Paso. (2006). Retrieved from http://wwwold.ece.utep.edu/research/webedl/cdte/Fabrication/index.htm

[6]*Byu cleanroom*. Brigham Young University. (2009). Retrieved from http://www.cleanroom.byu.edu/metal.phtml

[7]Donnellan, T. (2010). *Applied research labratory*. Retrieved from http://www.arl.psu.edu/mm_mp_ac_ebpvd.php

[8]Garcés, G. (2000). Texture of magnesium alloy films growth by physical vapour deposition (PVD). *Journal of Alloys and Compounds*, *309*(1-2), 229-238. doi:10.1016/S0925-8388(00)01075-6

[9]USGS Minerals Information: Magnesium. *USGS Mineral Resources Program*. Retrieved from <http://minerals.usgs.gov/minerals/pubs/commodity/magnesium/>.

[10]Amundsen, K., Aune, T. K., Bakke, P., Eklund, H. R., Haagensen, J. Ö., Nicolas, C., Rosenkilde, C., Van den Bremt, S. and Wallevik, O. 2003. Magnesium. Ullmann's Encyclopedia of Industrial Chemistry.

[11]Magnesium. *Office of Dietary Supplements (ODS)*. Retrieved from <http://ods.od.nih.gov/factsheets/magnesium>.

[12]Mark P. Staiger, Alexis M. Pietak, Jerawala Huadmai, George Dias, Magnesium and its alloys as orthopedic biomaterials: A review, Biomaterials, Volume 27, Issue 9, March 2006, Pages 1728-1734, ISSN 0142-9612, 10.1016/j.biomaterials.2005.10.003.

[13]Song, G. and Atrens, A. (2003), Understanding Magnesium Corrosion—A Framework for Improved Alloy Performance. Advanced Engineering Materials, 5: 837–858. doi: 10.1002/adem.200310405

[14]Jacobson, G. "Basic Forms of Corrosion." *NACE International*. 2006.

[15] Olivetti, E. (2010). *Life cycle impacts of alkaline batteries with a focus on end of life*. Massachusetts Institute of Technology.

[16]Wintherjensen, B., Gaadingwe, M., Macfarlane, D., & Forsyth, M. (2008). Control of magnesium interfacial reactions in aqueous electrolytes towards a biocompatible battery. *Electrochimica Acta*, *53*(20), 5881-5884. doi:10.1016/j.electacta.2008.04.005

[17] http://www.esm.psu.edu/litecms/media/105_sem1a2.jpg

[18]D. A. Jones, Principles and Prevention of Corrosion, 2nd edition, edited by W. Stenquist and R. Kernan. Prentice Hall, Upper Saddle River, NJ, 1996, pp.

[19] Shaw, B. (2011) *Lab 9 EIS*. ESC 455. Pennsylvania State University

[20] Sean M. Pursel, John D. Petrilli, Mark W. Horn and Barbara A. Shaw, "Effect of alloy addition and growth conditions on the formation of Mg-based bioabsorbable thin films", Proc. SPIE 7041, 704113 (2008);http://dx.doi.org/10.1117/12.796918

[21] Naccarelli, A. “Development, Characterization, and Testing of Anode Components for a Biodegradable Seawater Battery.” 2012.

Academic Vita

Robert W. Gresh, IV
186 Quick Farm Lane • State College, PA 16801 • 814-933-6018

Education
Penn State University
Shreyer Honors College
BS in Engineering Sciences, May 2012

Experience
Penn State University
January 2011-Current
Research Internship

- •Studying under one of the leading researchers in thin film development.
- •Utilize electron beam physical vapor deposition to create bio-compatible magnesium alloys that are easily and safely dissolved in the body.

Penn State University
June 2008-August 2008
Summer Placement

- •Assisted in production of vanadium oxide thin film for application in military-grade night vision equipment.
- •Conducted various tests to analyze the electrical and thermal properties of materials.

Fire One • www.fireone.com
June 2008-December 2010
Summer Placement

- •Studied under the electrical engineer who developed the world's most-advanced pyrotechnic choreography system, the 2-wire system, and the iMatch used in shows such as the 2008 Beijing Olympics.
- •Traveled to observe the consultation for FireOne at shows such as Syndey (Australia) New Year's Eve.
- •Constructed hundreds of varying hardware pieces by hand, and conducted electrical tests regularly in the FireOne warehouse.

Global Community Service

Zambia
HIV/AIDS Education Team
Spring 2006/Spring 2008

Peru
Orphanage Building Project
Summer 2010